Mechanics and transport characterization of bioengineered tissue microenvironment platforms

Elizabeth Elena Antoine

Dissertation submitted to the faculty of the Virginia Polytechnic Institute and State University in partial fulfillment of the requirements for the degree of

Doctor of Philosophy
In
Mechanical Engineering

Marissa N. Rylander, Co-Chair
Pavlos P. Vlachos, Co-Chair
Rafael V. Davalos
Raffaella De Vita
Carla V. Finkielstein
Cameron D. Tropea

3.25.2014
Blacksburg, Virginia

Keywords: collagen hydrogel; extracellular matrix; mechanical properties; microstructure; particle image velocimetry

ProQuest Number: 10593014

ProQuest 10593014

Mechanics and transport characterization of bioengineered tissue microenvironment platforms

Elizabeth Elena Antoine

Abstract

The tissue microenvironment is a complex living system containing heterogeneous mechanical and biophysical cues. Cellular components are surrounded by extracellular matrix and interstitial fluid, while transport of nutrients and biochemical factors is achieved via the vasculature. Each constituent of the tissue microenvironment can play a significant role in its ability to function normally. Many diseases including cancer have been linked with dysfunction in the tissue microenvironment; therefore an improved understanding of interaction between components of this complex system is needed.

In vitro platforms mimicking the tissue microenvironment appear to provide the most promising avenue for studies of cell-cell and cell-matrix interactions as well as elucidation of the mechanisms leading to disease phenomena such as tumor metastasis. However, successful recapitulation of all three primary components of the tissue microenvironment in three dimensions has remained challenging. In particular, matching mechanical cues and biochemical transport to *in vivo* conditions is difficult because of lack of quantitative characterization of the physical properties and parameters of such platforms.

In this work, extensive characterization of collagen I hydrogels, popular for use as extracellular matrix mimics, was performed in order to enable tuning to specific *in vivo* conditions. Additionally, perfusion of blood in a 3D tissue microenvironment platform fabricated using collagen hydrogels was characterized to enable future advances in *in vitro* modeling of the *in vivo* microenvironment. Finally, the tissue microenvironment platform is modified to enable biochemical gradients within the hydrogel and used to examine directed migration (chemotaxis) of human breast cancer cells in response to gradients in growth factor combined with varied stiffness and pore diameter of the extracellular matrix.

Acknowledgements

If I have learned one thing as a graduate student, it is that research cannot be performed in a vacuum. Many individuals and organizations have supported and encouraged me during these years at Virginia Tech. I regret that I cannot list by name everyone who has influenced my development as a scientist and as a person; however several people deserve special mention.

This work would not have been possible without the support of my research advisors, Dr. Vlachos and Dr. Rylander. I am grateful for their constant guidance and mentoring throughout my graduate studies, without which I would have been lost. I would also like to thank my committee members Dr. Davalos, Dr. De Vita, Dr. Finkielstein, and Dr. Tropea for their insightful comments and discussions.

I would like to thank all of the members of the AEThER lab and the TENCR lab for all of their help finding equipment and building experiments, willingness to troubleshoot data analysis and proofread manuscripts, but more importantly, the community and friendship that only fellow graduate students can provide. I especially would like to thank Dr. Cara Buchanan who taught me how to function in a tissue engineering lab and was instrumental in helping me develop impactful research questions.

These acknowledgements would be incomplete without special recognition of my team of outstanding undergraduate volunteers Akshata, Corbin, David, and Jiffin, whose efforts made it possible to acquire the massive amount of data presented in Chapter 4. Beyond that, your unfailing energy and excitement about research have inspired me more than you know.

Above all, I am indebted to my husband, Guillaume, who has encouraged, inspired, centered, and loved me through every step of this journey.

Attribution

This dissertation is composed of an introduction, literature review, three main chapters, a conclusion, and an appendix. Each of the main chapters represents an original manuscript published, under review, or in preparation for publication as a journal article, while the appendix contains a fourth manuscript in preparation. The first of the three main chapters (Chapter 3) is a review, while the other two chapters are research articles.

Dr. Pavlos P. Vlachos, Ph.D., Professor of Mechanical Engineering and Biomedical Engineering, Purdue University, is a committee co-chair and has provided advice and insight for the work described in each chapter. Dr. Vlachos is a co-author on each of the papers.

Dr. M. Nichole Rylander, Ph.D., Associate Professor in Mechanical Engineering, Virginia Tech, is a committee co-chair and has provided advice and insight for the work described in each chapter. Dr. Rylander is a co-author on each of the papers.

Dr. Cara F. Buchanan, Ph.D., Scientist, École Polytechnique Fédérale de Lausanne, developed the original collagen microchannel system and helped acquire the data for the work presented in Chapter 5. Dr. Buchanan is a co-author on Chapter 5.

Dr. Kamel Fezzaa, Ph.D., Physicist, Advanced Photon Source, Argonne National Laboratory, assisted with data acquisition at the ANL Advanced Photon Source and contributed to discussions of x-ray phase contrast imaging for Chapter 5. Dr. Fezzaa is a co-author on Chapter 5.

Dr. Wah-Keat Lee, Ph.D., Photon Sciences Staff, National Synchrotron Light Source II, Brookhaven National Laboratory, assisted with data acquisition at the ANL Advanced Photon Source and contributed to discussions of x-ray phase contrast imaging for Chapter 5. Dr. Lee is a co-author on Chapter 5.

Table of Contents

List of Figures

List of Tables

List of Abbreviations

3D	three-dimensional
3PG	three-point Gaussian
AFM	atomic force microscopy
APS	Advanced Photon Source
BSA	bovine serum albumin
CFM	confocal fluorescence microscopy
CI	chemotactic index
CRM	confocal reflectance microscope
dH$_2$O	distilled water
dSLR	digital single-lens reflex
DMA	dynamic mechanical analysis
DMEM	Dulbecco's modified eagle's medium
ECM	extracellular matrix
EGF	epidermal growth factor
FEP	fluorinated ethylene propylene
FITC	fluorescein isothiocyanate
FRAP	fluorescence recovery after photobleaching
GAG	glycosaminoglycan
GFP	green fluorescent protein
μPIV	micro-particle image velocimetry
PBS	phosphate buffered saline
PDMS	polydimethylsiloxane
PEG	polyethylene glycol
PEGDA	polyethylene glycol diacrylate
PEI	polyethyleneimine
PEO	polyethylene oxide
PLGA	poly(lactic-*co*-glycolic) acid
PIV	particle image velocimetry
PRMSR	peak-to-root mean square ratio
PTFE	polytetrafluoroethylene
RBC	red blood cell
RMS	root mean square
RPC	robust phase correlation
SCC	standard cross correlation
SEM	scanning electron microscopy

SHG	second harmonic generation
SNR	signal-to-noise ratio
TEM	transmission electron microscopy
TPF	two-photon fluorescence
UOD	universal outlier detection
VEGF	vascular endothelial growth factor

1 Introduction

1.1   Motivation

The tissue microenvironment is a complex system containing three major components occupying the same three-dimensional space: interstitium composed of structural matrix and surrounding fluid, vasculature, and cells. Each of these components can be comprised of multiple subcomponents: for example, extracellular matrix is primarily composed of collagen in soft tissues, but also contains varying levels of elastin, proteoglycans, and other macromolecules. Moreover, the spatial distribution of microenvironmental components is highly heterogeneous. Each of these elements of the microenvironment can have a profound impact on tissue function [1].

The tissue microenvironment is coming under close scrutiny as a potential avenue for study of disease and design of new disease therapies as well as tissue regeneration. An outstanding question in current cancer research is the importance of the link between tumor malignancy and abnormalities in the tumor microenvironment – tortuous, leaky vasculature, high protein deposition in the extracellular matrix (ECM), and poor oxygenation and nutrition due to limited perfusion and diffusion [2-4]. Stem cell differentiation and proliferation are known to be regulated by site-specific cues from the microenvironment including elasticity, ECM composition, and capacity of the microenvironment to transport signaling molecules between cells [5-7]. Drug delivery therapies depend strongly on the ability of the treatment to penetrate the microenvironment and reach the disease location.

Across these and other applications, similar challenges face all attempts to engineer an *in vitro* tissue microenvironment. Although *in vitro* models are extremely popular for investigation specific cell-cell and cell-matrix interactions, few such devices recapitulate all major components of the tissue microenvironment. Furthermore, those devices which do contain interstitium, perfusion, and cells seldom replicate the three-dimensional spatial arrangements of *in vivo* tissues. This limitation of current engineered tissues is widely recognized and there is a need for *in vitro* tissue microenvironment platforms with increased physiological fidelity.

1.2 Objective

The objective of this work was the development of a three-dimensional *in vitro* tissue microenvironment platform. This was achieved through integration of tissue engineering, experimental design, materials characterization, and particle image velocimetry (PIV) strategies. The *in vitro* tissue microenvironment platform was developed through design and characterization of two of the three primary components of the microenvironment as illustrated in Figure 1-1: collagen I hydrogels with precisely tunable mechanics and mass transport properties mimicking the interstitium and perfused microchannels with well-characterized physiological flow mimicking the vasculature. In ongoing work, the third and final component of the tissue microenvironment has been introduced to the platform in the form of human breast cancer cells. This complete microenvironment platform is being used to investigate interactions between the three components of the tissue microenvironment.
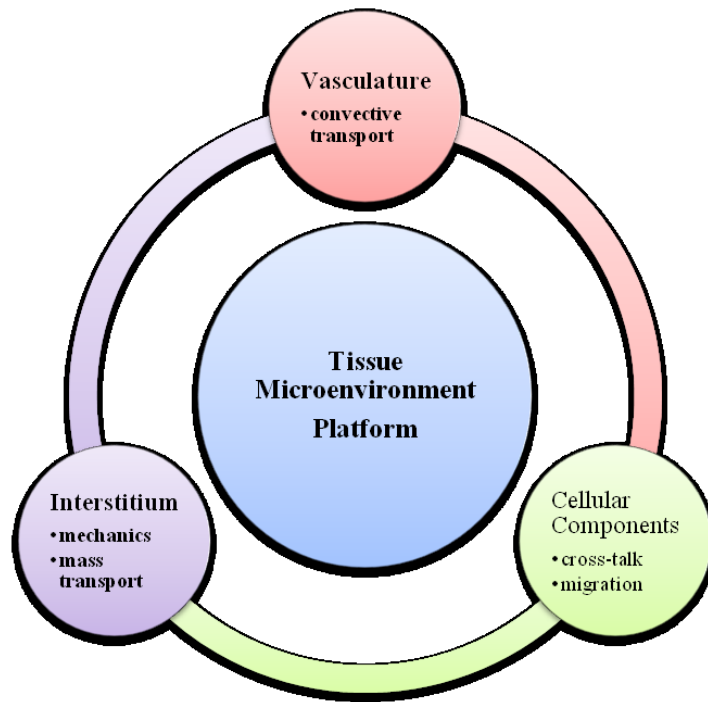
Figure 1-1: Diagram of the tissue microenvironment illustrating the dissertation objective.

1.3   Dissertation Overview

This dissertation is organized as follows: Chapters 1 and 6 provide the introduction and conclusion to the work. Chapter 2 presents an in-depth literature review of the tissue microenvironment to inform the reader about the main objectives of this work. Each of the main chapters (3-5) represents an original work, presented as a complete manuscript formatted for journal publication. Chapter 3 is an extensive review of current methods used for fabrication and characterization of collagen I hydrogels for tissue engineering, while Chapter 4 is an original research paper which addresses the challenges identified in Chapter 3 through measurement and analysis of collagen I hydrogel functional properties. Chapter 5 presents flow characterization of blood perfusion of a thick collagen tissue model using x-ray μPIV. Finally, the Appendix provides a fourth manuscript in preparation which investigates tumor cell response to growth factor gradients in the microenvironment platform.

1.4   Scientific Merit

This work, integrating measurement and instrumentation with tissue engineering, materials characterization, and flow analysis, provides the development and characterization of a novel tissue microenvironment platform with physiologically relevant mechanics, flow and mass transport. First, we investigated the mechanical and transport properties of collagen I hydrogels commonly used to mimic tissue interstitium. We reviewed the literature and found that the current characterization of hydrogel functional properties lacks coherence and is insufficient for use in design of complex engineered tissues. To address this obstacle to tissue microenvironment design, we developed an experimental data set, comprehensive sensitivity analysis and predictive regression models which can be used to tune hydrogels to mimic the interstitium of a broad range of *in vivo* tissues. Finally, we quantified blood flow within a perfused collagen hydrogel device using x-ray phase contrast particle image velocimetry, enabling future development of the system to utilize whole blood perfusion. In ongoing work, a parallel-perfusion microenvironment platform was developed for investigation of the role of interactions between matrix stiffness and epithelial growth factor (EGF) gradients on motility and directed migration of human breast cancer cells (MDA-MB-231). Ultimately, this platform will serve as a tool for experimental studies of interactive processes within the tissue microenvironment.

3

2 Literature Review

2.1 Basics of the Tissue Microenvironment

The tissue microenvironment is composed of three primary components: interstitium, vasculature, and cellular components [8]. Each of these can play a role in various diseases; for example, it is theorized that many of the physiological differences between the tumor microenvironment and that of healthy tissue stem from irregularities in the tumor vasculature and low perfusion rates [2, 9]. Therefore, these components must be considered in any study of the tissue microenvironment.

The arterial tree contains several orders of magnitude of vessel diameter and perfusion flow rate. Many tissue functions have been demonstrated to be affected by flow rate; in particular, endothelial cells only develop tight junctions and normal barrier function when exposed to physiological shear stresses [10, 11]. Perfusion conditions can also affect the availability of oxygen and nutrients to cells within the tissue.

The interstitial space is composed of extracellular matrix (ECM) and interstitial fluid which is transported through the lymphatic system. The ECM is the structural basis of tissue and primarily contains macromolecules including fibrous proteins (collagen and elastin) and polysaccharides such as hyaluronan and proteoglycans [1]. The composition and structure of these macromolecules varies significantly with tissue type and can be altered by disease. As a result, the mechanical properties of the interstitium can vary widely. Stiffnesses of soft tissues can vary between 10^2 Pa and 10^8 Pa [12], while the structure of the protein network can exhibit pore sizes from the nanoscale to the microscale. Furthermore, the extracellular matrix and surrounding interstitial fluid form a porous network which regulates diffusion of nutrients, oxygen, and other molecules in tissue. Diffusion-driven concentration gradients in biochemicals in the tissue microenvironment cam stimulate cell response and migration.

Depending on the tissue, cellular components can be numerous and exhibit complex intercellular signaling. Cell response to both mechanical and chemical aspects of the microenvironment can be described in terms of biochemical response, such as gene and protein expression, or mechanical response, such as morphological changes, proliferation, and migration.

4

2.2   Engineering the Tissue Microenvironment

The three fundamental approaches to research – analytical, numerical, and experimental – have been applied to study of the tissue microenvironment with varying levels of success. Tissue dynamics have generally been considered to be too complex for analytical techniques to be practical. Computer models based on numerical techniques, or *in silico* models, are increasingly being used as computational resources become more available, and show promise for prediction of tissue microenvironmental dynamics such as cell migration patterns [13]. *In silico* models have been used, for example, to suggest that hypoxia and acidification are key mechanisms in tumor malignancy [9]. Although *in silico* models are promising, they are cannot be used independently as they are strongly dependent on input parameters and prioritization of mechanisms, both of which must be obtained experimentally [13]. Additionally, numerical models must be validated with experimental data. Future advances in our understanding of the tissue microenvironment will likely be based on complementary numerical and experimental models [9].

Experimental techniques fall under two broad categories: *in vivo*, in a living human or animal, and *in vitro*, laboratory experiments using tissue reconstructed using live cells. While *in vivo* models duplicate the clinical environment better than *in vitro* models, and always form a necessary stage in the development of new treatments for various types of disease, the *in vivo* tissue microenvironment remains too complex for individual mechanisms be easily quantified and characterized. *In vitro* models offer more precise control of input parameters than *in vivo* models, while their lower complexity allows isolation of individual mechanisms.

The potential of three-dimensional (3D) *in vitro* tissue models for quantitative studies of normal and diseased microenvironments and evaluation of drug efficacy is widely recognized [14, 15]. However, the value of an *in vitro* model is dependent on its reproduction of complex temporal and spatial interactions as found in the physical microenvironment [1, 15]. An engineered *in vitro* tissue microenvironment should incorporate the spatial configuration, structure, and dynamic response of *in vivo* tissues [1, 16]. Finally, the *in vitro* tissue microenvironment must be designed so that control and response parameters can be accurately measured. Quantification of the tissue microenvironment is addressed in the concluding section of this literature review.

5

The benefits of 3D *in vitro* tissue models over two-dimensional systems have been well documented [17, 18]. It has been shown that cells exhibit significantly non-physiological morphology and behavior in two-dimensional cultures [1, 19]. Cells grown in two dimensions develop a flattened morphology with flat lamellipodia and form adherent single layers. Migration in two dimensions can occur only within the plane; however, it is unrestricted due to the lack of structural matrix [20, 21]. In contrast, cells grown in three dimensions are surrounded and supported structurally by ECM in a fiber network, which forces them to form a spindle-shaped morphology with cylindrical pseudopodia [19, 22]. The presence of the ECM permits cells to use different attachment mechanisms than in two dimensions [23, 24], and three-dimension migration aided by proteolysis-induced ECM remodeling is possible [25]. The ECM fiber structure regulates cell motility, with the optimal pore size slightly smaller than the cell diameter to permit cell migration in three dimensions through the structure while inhibiting slow one-dimensional migration [24, 26, 27]. Similarly, it has been shown that ECM stiffness leads to stability of the scaffold, stimulating cell motility [28, 29]. Cells exhibit migratory response to stiffness gradients (durotaxis) as well as density gradients (haptotaxis) [1, 17, 19, 30, 31]. Transport of nutrients, oxygen, metabolites, and signaling molecules in three-dimensions is diffusion-limited and triggers cellular biochemical response while two-dimensionally cultured cells obtain chemicals through direct contact with culture media [17, 32].

Since the development of tissue engineering, most studies of the interaction between cell and substrate have been in two dimensions [26, 27]. Only recently has the relevance of three-dimensionality for cell motility and ECM interaction been noted. To achieve 3D *in vitro* tissue models, cells can be grown on scaffolds representative of ECM. Because the *in vitro* microenvironment must not only permit physiological cell migration and adhesion, but must also accommodate fabrication, scaffold materials must be carefully selected. Key structural parameters of an *in vitro* scaffold are dimension, pore size, and stiffness [13, 26]. Previous 3D tissue models have used scaffolds including Matrigel, paper, native type I collagen, collagen-glycosaminoglycan (GAG), polyacrylamide (PA), polyethylene oxide (PEO), polyethylene glycol (PEG), fibrinogen, poly(lactic-*co*-glycolic) acid (PLGA), and more [1, 18, 25, 26, 30, 31, 33, 34]. Of these, type I collagen is favorable for use as a tissue scaffold because it is a major component of native ECM, provides a natural, remodelable environment for many types of cells during proliferation and migration, is readily available via isolation from animal tissues such as

porcine skin or murine tails, and can in theory be reconstituted with tailored density, fiber structure, stiffness and diffusivity for specified particles [1, 35, 36]. One drawback is that collagen exhibits a low elastic modulus relative to synthetic scaffold materials, which makes microfabrication challenging; however, several groups have successfully fabricated microstructures within collagen using various techniques [37, 38].

The presence of a perfusion mechanism which captures the dynamics of the vasculature is necessary to enable continuous mass transport through the engineered tissue and sustain a physiological nutrient supply [32, 39]. Transwell assays, which can contain quasi-3D scaffolds such as a collagen layer across the well, have high throughput and permit measurement of gene and protein expression, but are static cultures and therefore unable to reproduce the dynamics of biological tissues [40]. Recently, microfabrication techniques have been developed to produce high-resolution 2D and 3D microchannels in elastomers such as polydimethylsiloxane (PDMS) or hydrogels such as alginate, Matrigel, and collagen, producing perfusable devices that can sustain cell proliferation [1, 33, 37, 39, 41-45].

Perfused 3D systems permit temporal control of convection-driven gradients in the microenvironment for better physiological accuracy [19]. State-of-the-art microfluidic devices for tissue engineering are primarily based on microchannels formed by soft lithography in PDMS and sealed with glass coverslips for imaging [40, 44, 46-50]. Although such systems can provide 3D scaffolds for cell culture and complex planar geometries with varied cell density and perfusion characteristics, and have proven to be relatively robust, the space limitations inherent to silicon-molded microfabricated designs restrict dynamic cellular processes in the perpendicular dimension, so although such systems can have 3D ECM, dynamic processes occur in 2D. Furthermore, the influence of artificial boundaries imposed on the cells at the PDMS and glass interfaces and the effect of limiting the scaffold thickness to only a few cells [51] are likely significant [52] but yet unknown. There remains wide variation between experimental approaches and devices for the *in vitro* study of the tissue microenvironment [53]; furthermore, no device yet exists which is capable of mechanical and/or chemical microenvironmental gradients with true 3D dynamic geometry and dynamics.

7

2.3   Quantification of the Tissue Microenvironment

This section describes technology currently available for measuring the range of parameters relevant to the hypothesis described in the previous section. These include quantitative techniques for measurement of microenvironmental factors such as tissue material properties and relevant transport characteristics including diffusion, velocity distribution and wall shear stress.

2.3.1   Materials Characterization

Complete characterization of biological tissues is a monumental task. However, certain material properties are of particular relevance for tissue engineering and several techniques have been developed for their measurement. Chapter 3 provides an extensive review of fabrication parameters and characterization techniques for collagen I hydrogels in particular; however, here a brief generalized overview is provided.

Tissue elasticity varies in nature and magnitude across various biological tissues. Soft tissues have strongly nonlinear elastic properties as they are generally both viscoelastic and anisotropic. Much variation exists between groups with regards to the definition used for reported stiffness as well as measurement technique [54]. Some stiffness measurement methods of interest include tensile and compression testing, rheometry, atomic force microscopy (AFM) and nanoindentation. Tensile testing, while the classic approach to stiffness measurement, often fails for extremely soft tissues and hydrogels. Uniaxial compression testing involves displacing a sample between large plates while measuring the resistive force, and can be extremely robust but requires relatively large, isotropic samples and provides only a mean stiffness measurement. Rheological testing provides information on shear modulus which has limited applicability for most hydrogels. AFM stiffness measurements are performed by prodding the sample with a nanoscale cantilever of known stiffness and measuring the tip displacement with a laser. While this provides measurements with high spatial resolution, the difference in stiffness between available cantilevers and soft tissues and the variability in cantilever geometry results in low measurement accuracy. Furthermore, AFM is poorly suited for measurement of bulk properties of heterogeneous matrices. Nanoindentation is a similar approach with similar advantages and disadvantages. For all contact-based techniques, surface tension can lead to significant error for low-stiffness samples. Because each method has different advantages and disadvantages, the best

method for a particular sample depends on that sample's properties and *in vivo* loading characteristics.

The structure of tissue extracellular matrix is most often quantified by analysis of some type of image of the fiber network to obtain fiber diameter, pore size, and fiber density [54]. This is challenging because of the small scale of both the fibers and the fiber network. Scanning electron microscopy (SEM) is often considered the gold standard for nanoscale imaging as it can provide images with better than 1 nm resolution; however, because conventional SEM requires an electrically conductive sample under high vacuum, it cannot be used to image hydrated samples. Biological samples are often fixed, dehydrated, and sputter-coated with gold in preparation for SEM; however, it is unknown what effect each of the actions may have on the properties of the fiber network so it is not suited for hydrogel characterization [55]. Even environmental SEM, which was developed to permit imaging of samples under low pressure rather than high vacuum, cannot be used for hydrated tissues and hydrogels. AFM is another technique often used for generating topographical images; however, the hydration of the tissue is again a problem as the liquid layer on the sample surface limits the capacity of the AFM cantilever to reach the fiber network and furthermore reduces measurement resolution. The most popular option for imaging tissue and hydrogel fiber structure is confocal reflectance microscopy [56]. Using a high magnification high-numerical aperture lens and small pinhole, high-resolution images of collagen fibers can be obtained. Some studies indicate that fluorescent labeling of the collagen fibers can be used to further enhance image quality [33]. The key advantage to this technique is that it can be applied to fully hydrated tissues and gels and requires no sample preparation or manipulation.

2.3.2 Transport Characterization

The rate of diffusion of a particle in a hydrogel is dependent on the particle size, tissue fiber structure, and hydration medium. It is tempting to estimate diffusivity indirectly from porous media theory and known tissue structural parameters; however, this estimate requires precision of prior measurements and is accurate only for strictly homogeneous materials. Therefore, direct measurement is generally required. As with structure characterization, diffusion characterization is usually performed using optical methods. Generally, the diffusing material is fluorescently labeled and imaged in real-time as a concentrated sample diffuses into surrounding tissue.

Fluorescence recovery after photobleaching, or FRAP, is a modification of this technique in which the fluorescently labeled probe is homogeneously distributed in the sample and photobleached in a central small region using a laser or other high-intensity light source. Images are recorded as the bleached and unbleached materials diffuse into one another. In both cases, the intensity distribution in the recorded images can be used to compute the rate of diffusion [57, 58].

Conventionally, hydrodynamic characterization of biological tissues is restricted to measurement of the mean flow rate and an assumption of Poiseuille flow is used to estimate shear stress. This is because of the difficulty in obtaining accurate high-resolution experimental measurements. Particle image velocimetry (PIV) is a technique for measuring velocity flow fields that is gaining popularity for flow measurements in biological tissues not only because it produces temporally and spatially resolved information, accurate measurements, but also because it is a noninvasive technique and therefore suitable for measurements in tissues and cell cultures. In a typical PIV measurement, a pulsed laser sheet illuminates tracer particles seeded throughout the fluid, which are imaged by a high-speed camera. Cross-correlation of pairs of images is used to calculate the statistical particle displacement, which can be used with the time delay between images to compute the velocity field. Micro-particle image velocimetry (microPIV) is an adaptation for microfluidic applications that uses fluorescent tracer particles and imaging through an inverted epifluorescent microscope. In a paper coauthored with Dr. Cara Buchanan, we describe the application of microPIV for the first time to obtain wall shear stress measurements in a cylindrical perfused collagen hydrogel [38]. The primary disadvantage of PIV for biological applications is that the technique requires optical access to the flow of interest as well as refractive index matching at all non-planar surfaces; these require that *in vitro* tissue microenvironments be carefully designed if microPIV is to be performed. Recent work has demonstrated the feasibility of x-ray PIV for accurate flow measurements in opaque flows [59-62] and this may become a viable option for *in vitro* microenvironment models in the future.

References

1. Griffith, L.G. and M.A. Swartz, *Capturing complex 3D tissue physiology in vitro.* Nat Rev Mol Cell Biol, 2006. **7**(3): p. 211-24.
2. Brown, J.M. and A.J. Giaccia, *The unique physiology of solid tumors: Opportunities (and problems) for cancer therapy.* Cancer Research, 1998. **58**(7): p. 1408-1416.
3. Vaupel, P., F. Kallinowski, and P. Okunieff, *Blood-Flow, Oxygen and Nutrient Supply, and Metabolic Microenvironment of Human-Tumors - a Review.* Cancer Research, 1989. **49**(23): p. 6449-6465.
4. Jang, S.H., et al., *Drug delivery and transport to solid tumors.* Pharm Res, 2003. **20**(9): p. 1337-50.
5. Engler, A.J., et al., *Extracellular matrix elasticity directs stem cell differentiation.* J Musculoskelet Neuronal Interact, 2007. **7**(4): p. 335.
6. Prewitz, M.C., et al., *Tightly anchored tissue-mimetic matrices as instructive stem cell microenvironments.* Nat Methods, 2013. **10**(8): p. 788-94.
7. Holst, J., et al., *Substrate elasticity provides mechanical signals for the expansion of hemopoietic stem and progenitor cells.* Nat Biotechnol, 2010. **28**(10): p. 1123-8.
8. Jain, R.K., *Transport of molecules in the tumor interstitium: a review.* Cancer Research, 1987. **47**(12): p. 3039-51.
9. Henning, T., et al., *Relevance of tumor microenvironment for progression, therapy and drug development.* Anti-Cancer Drugs, 2004. **15**(1): p. 7-14.
10. Seebach, J., et al., *Regulation of endothelial barrier function during flow-induced conversion to an arterial phenotype.* Cardiovasc Res, 2007. **75**(3): p. 596-607.
11. Phelps, J.E. and N. DePaola, *Spatial variations in endothelial barrier function in disturbed flows in vitro.* Am J Physiol Heart Circ Physiol, 2000. **278**(2): p. H469-76.
12. Leventhal, I., P.C. Georges, and P.A. Janmey, *Soft biological materials and their impact on cell function.* Soft Matter, 2007. **3**(3): p. 299-306.
13. Friedl, P. and K. Wolf, *Plasticity of cell migration: a multiscale tuning model.* J Cell Biol, 2010. **188**(1): p. 11-9.
14. Mueller-Klieser, W., *Three-dimensional cell cultures: from molecular mechanisms to clinical applications.* Am J Physiol, 1997. **273**(4 Pt 1): p. C1109-23.
15. Yamada, K.M. and E. Cukierman, *Modeling tissue morphogenesis and cancer in 3D.* Cell, 2007. **130**(4): p. 601-610.
16. Kim, J.B., *Three-dimensional tissue culture models in cancer biology.* Semin Cancer Biol, 2005. **15**(5): p. 365-77.
17. Pampaloni, F., E.G. Reynaud, and E.H. Stelzer, *The third dimension bridges the gap between cell culture and live tissue.* Nat Rev Mol Cell Biol, 2007. **8**(10): p. 839-45.
18. Fischbach, C., et al., *Engineering tumors with 3D scaffolds.* Nat Methods, 2007. **4**(10): p. 855-60.
19. Li, S., J.L. Guan, and S. Chien, *Biochemistry and biomechanics of cell motility.* Annu Rev Biomed Eng, 2005. **7**: p. 105-50.
20. Ridley, A.J., et al., *Cell migration: integrating signals from front to back.* Science, 2003. **302**(5651): p. 1704-9.
21. Vitorino, P. and T. Meyer, *Modular control of endothelial sheet migration.* Genes Dev, 2008. **22**(23): p. 3268-81.

22. Jiang, H. and F. Grinnell, *Cell-matrix entanglement and mechanical anchorage of fibroblasts in three-dimensional collagen matrices*. Mol Biol Cell, 2005. **16**(11): p. 5070-6.

23. Maaser, K., et al., *Functional hierarchy of simultaneously expressed adhesion receptors: integrin alpha2beta1 but not CD44 mediates MV3 melanoma cell migration and matrix reorganization within three-dimensional hyaluronan-containing collagen matrices*. Mol Biol Cell, 1999. **10**(10): p. 3067-79.

24. Haston, W.S., J.M. Shields, and P.C. Wilkinson, *Lymphocyte locomotion and attachment on two-dimensional surfaces and in three-dimensional matrices*. J Cell Biol, 1982. **92**(3): p. 747-52.

25. Wolf, K., et al., *Amoeboid shape change and contact guidance: T-lymphocyte crawling through fibrillar collagen is independent of matrix remodeling by MMPs and other proteases*. Blood, 2003. **102**(9): p. 3262-9.

26. Harley, B.A., et al., *Microarchitecture of three-dimensional scaffolds influences cell migration behavior via junction interactions*. Biophys J, 2008. **95**(8): p. 4013-24.

27. Doyle, A.D., et al., *One-dimensional topography underlies three-dimensional fibrillar cell migration*. J Cell Biol, 2009. **184**(4): p. 481-90.

28. Shoulders, M.D. and R.T. Raines, *Collagen structure and stability*. Annu Rev Biochem, 2009. **78**: p. 929-58.

29. Wolf, K., et al., *Collagen-based cell migration models in vitro and in vivo*. Semin Cell Dev Biol, 2009. **20**(8): p. 931-41.

30. Lo, C.M., et al., *Cell movement is guided by the rigidity of the substrate*. Biophysical Journal, 2000. **79**(1): p. 144-152.

31. Isenberg, B.C., et al., *Vascular smooth muscle cell durotaxis depends on substrate stiffness gradient strength*. Biophys J, 2009. **97**(5): p. 1313-22.

32. Malda, J., T.J. Klein, and Z. Upton, *The roles of hypoxia in the in vitro engineering of tissues*. Tissue Eng, 2007. **13**(9): p. 2153-62.

33. Cross, V.L., et al., *Dense type I collagen matrices that support cellular remodeling and microfabrication for studies of tumor angiogenesis and vasculogenesis in vitro*. Biomaterials, 2010. **31**(33): p. 8596-607.

34. Cheung, Y.K., et al., *Microscale Control of Stiffness in a Cell-Adhesive Substrate Using Microfluidics-Based Lithography*. Angewandte Chemie-International Edition, 2009. **48**(39): p. 7188-7192.

35. Paszek, M.J., et al., *Tensional homeostasis and the malignant phenotype*. Cancer Cell, 2005. **8**(3): p. 241-254.

36. Ramanujan, S., et al., *Diffusion and convection in collagen gels: Implications for transport in the tumor interstitium*. Biophysical Journal, 2002. **83**(3): p. 1650-1660.

37. Chrobak, K.M., D.R. Potter, and J. Tien, *Formation of perfused, functional microvascular tubes in vitro*. Microvascular Research, 2006. **71**(3): p. 185-196.

38. Buchanan, C.F., et al., *Three-Dimensional Microfluidic Collagen Hydrogels for Investigating Flow-Mediated Tumor-Endothelial Signaling and Vascular Organization*. Tissue Eng Part C Methods, 2014. **20**(1): p. 11.

39. Wlodkowic, D. and J.M. Cooper, *Tumors on chips: oncology meets microfluidics*. Curr Opin Chem Biol, 2010. **14**(5): p. 556-67.

40. Polacheck, W.J., I.K. Zervantonakis, and R.D. Kamm, *Tumor cell migration in complex microenvironments*. Cell Mol Life Sci, 2013. **70**(8): p. 1335-56.

41. Khademhosseini, A. and R. Langer, *Microengineered hydrogels for tissue engineering.* Biomaterials, 2007. **28**(34): p. 5087-92.

42. Lu, H., et al., *Microfluidic shear devices for quantitative analysis of cell adhesion.* Anal Chem, 2004. **76**(18): p. 5257-64.

43. Ling, Y., et al., *A cell-laden microfluidic hydrogel.* Lab Chip, 2007. **7**(6): p. 756-62.

44. Chung, S., et al., *Cell migration into scaffolds under co-culture conditions in a microfluidic platform.* Lab on a Chip, 2009. **9**(2): p. 269-275.

45. Cheng, S.Y., et al., *A hydrogel-based microfluidic device for the studies of directed cell migration.* Lab Chip, 2007. **7**(6): p. 763-9.

46. Wang, S.J., et al., *Differential effects of EGF gradient profiles on MDA-MB-231 breast cancer cell chemotaxis.* Exp Cell Res, 2004. **300**(1): p. 180-9.

47. Song, J.W. and L.L. Munn, *Fluid forces control endothelial sprouting.* Proc Natl Acad Sci U S A, 2011. **108**(37): p. 15342-7.

48. Aurand, E.R., K.J. Lampe, and K.B. Bjugstad, *Defining and designing polymers and hydrogels for neural tissue engineering.* Neurosci Res, 2012. **72**(3): p. 199-213.

49. Salieb-Beugelaar, G.B., et al., *Latest developments in microfluidic cell biology and analysis systems.* Anal Chem, 2010. **82**(12): p. 4848-64.

50. Frohlich, E.M., X. Zhang, and J.L. Charest, *The use of controlled surface topography and flow-induced shear stress to influence renal epithelial cell function.* Integr Biol (Camb), 2012. **4**(1): p. 75-83.

51. Zervantonakis, I.K., et al., *Three-dimensional microfluidic model for tumor cell intravasation and endothelial barrier function.* Proc Natl Acad Sci U S A, 2012. **109**(34): p. 13515-20.

52. Sung, J.H. and M.L. Shuler, *Microtechnology for Mimicking In Vivo Tissue Environment.* Annals of Biomedical Engineering, 2012. **40**(6): p. 1289-1300.

53. Buchanan, C. and M.N. Rylander, *Microfluidic culture models to study the hydrodynamics of tumor progression and therapeutic response.* Biotechnol Bioeng, 2013. **110**(8): p. 2063-72.

54. Antoine, E.E., P.P. Vlachos, and M.N. Rylander, *Collagen I Hydrogels for Tissue Engineering: Characterization of Functional Material Properties.* Tissue Engineering Part B: Reviews, in review.

55. Raub, C.B., et al., *Noninvasive assessment of collagen gel microstructure and mechanics using multiphoton microscopy.* Biophysical Journal, 2007. **92**(6): p. 2212-22.

56. Brightman, A.O., et al., *Time-lapse confocal reflection microscopy of collagen fibrillogenesis and extracellular matrix assembly in vitro.* Biopolymers, 2000. **54**(3): p. 222-234.

57. Berk, D.A., et al., *Fluorescence photobleaching with spatial Fourier analysis: measurement of diffusion in light-scattering media.* Biophysical Journal, 1993. **65**(6): p. 2428-36.

58. Seiffert, S. and W. Oppermann, *Systematic evaluation of FRAP experiments performed in a confocal laser scanning microscope.* J Microsc, 2005. **220**(Pt 1): p. 20-30.

59. Kim, G.B. and S.J. Lee, *Contrast enhancement of speckle patterns from blood in synchrotron X-ray imaging.* Journal of Biomechanics, 2009. **42**(4): p. 449-454.

60. Lee, S.J. and G.B. Kim, *X-ray particle image velocimetry for measuring quantitative flow information inside opaque objects.* Journal of Applied Physics, 2003. **94**(5): p. 3620-3623.

13

61. Lee, S.J., et al., *Development of a compact x-ray particle image velocimetry for measuring opaque flows.* Review of Scientific Instruments, 2009. **80**(3): p. -.
62. Jamison, R.A., et al., *X-ray Velocimetry and Haemodynamic Forces Within a Stenosed Femoral Model at Physiological Flow Rates.* Annals of Biomedical Engineering, 2011. **39**(6): p. 1643-1653.

3   Review of Collagen I Hydrogels for Bioengineered Tissue Microenvironments: Characterization of Mechanics, Structure, and Transport[*]

Elizabeth Antoine[1], Pavlos Vlachos[2], M. Nichole Rylander[3]

[1] Department of Mechanical Engineering, Virginia Tech, Blacksburg, Virginia, USA

[2] School of Mechanical Engineering, Purdue University, West Lafayette, Indiana, USA

[3] VT-WFU School of Biomedical Engineering and Sciences, Virginia Tech, Blacksburg, Virginia, USA

3.1   Abstract

Type I collagen hydrogels have been used successfully as 3D substrates for cell culture and have shown promise as scaffolds for engineered tissues and tumors. A critical step in the development of collagen hydrogels as viable tissue mimics is quantitative characterization of hydrogel properties and their correlation with fabrication parameters, which enables hydrogels to be tuned to match specific tissues or fulfill engineering requirements. A significant body of work has been devoted to characterization of collagen I hydrogels; however, due to the breadth of materials and techniques used for characterization, published data are often disjoint and hence their utility to the community is reduced. This review aims to determine the parameter space covered by existing data and identify key gaps in the literature so that future characterization research can be most efficiently conducted.

This review is divided into three sections: (1) relevant fabrication parameters are introduced and several of the most popular methods of controlling and regulating them are introduced, (2) hydrogel properties most relevant for tissue engineering are presented and discussed along with their characterization techniques, (3) the state of collagen I hydrogel characterization is recapitulated and future directions are proposed. Ultimately, this review can serve as a resource for selection of fabrication parameters and materials characterization methodologies in order to increase the usefulness of future collagen hydrogel-based characterization studies and tissue engineering experiments.

---

[*] In revision for Tissue Engineering Part B: Reviews.

3.2 Introduction

Three-dimensional (3D) scaffold-based culture models represent a rapidly growing niche in tissue engineering because they more closely mimic *in vivo* conditions than traditional cellular monolayers [1-4]. The class of materials known as hydrogels, which ranges from synthetic molecules such as poly(ethylene glycol) (PEG) to native proteins such as collagen and fibrin, has been demonstrated to be well-suited for use as 3D scaffolds [5-9]. Collagen-based hydrogels are gaining widespread popularity as scaffolds for tissue engineering due to the abundance of collagen in natural extracellular matrix (ECM). Collagen makes up 25% (by dry weight) of total protein *in vivo* [10, 11]; of the various types of collagen, type I is the most prevalent and is by far the most popular for tissue engineering due to its ease of extraction and adaptability for multiple applications.

Although collagen I is a viable scaffold for a wide range of applications [12-15], comparison between studies is difficult due to significant variation in hydrogel fabrication protocols used by different research groups. It is well known that scaffold material properties play an important role in cellular behavior [10, 12]. One of the main drawbacks to using collagen hydrogels as scaffolds for tissue engineering is that these properties are highly variable and dependent on a large number of fabrication parameters such as collagen source or gelation pH, resulting in a vast design space [10, 16-20]. The need for quantitative characterization of collagen hydrogels is recognized within the scientific community as a prerequisite for quantitative studies, tissue optimization, and comparative research [14, 17, 18].

Recent publications have aimed to characterize collagen material properties; however, the majority of previous studies have investigated relationships between isolated fabrication parameters and material properties without considering the influence of the full design space on material properties. Furthermore, just as there is wide variation in fabrication protocols implemented by each group, there is little overlap between fabrication parameters employed. Since fabrication parameters and material properties are coupled in collagen hydrogels, the data available in the literature form a set of scattered measurements that cannot be extrapolated to form a complete multidimensional data set. Because of this, the results of such studies are difficult to interpret and only qualitatively useful to other research groups.

16

This review aims to provide a guide to the collagen characterization data available in the literature to facilitate identification of the most relevant studies for design of future experiments. In this review, only fabrication parameters previously identified as having a significant effect on one or more hydrogel properties are discussed in detail. These parameters include collagen source, solubilization method, polymerization pH, polymerization temperature, ionic strength and collagen concentration [11, 14, 21, 22]. The hydrogel properties covered in this review, spanning polymerization, mechanics, structure, and transport, have previously been demonstrated to regulate cellular response [9, 10, 22-24].

For information on molecular characterization of collagen, the reader is directed to articles by Abraham et al. and Miller and Rhodes [14, 25]. Enhanced crosslinking techniques and composite hydrogels, most often used to enhance the strength of low-concentration collagen gels, are beyond the scope of this review as it focuses on basic hydrogel fabrication and properties. However, some works involving enhanced crosslinking are cited here in the context of their fabrication techniques and characterization methodologies. For further information and examples of enhanced crosslinking of collagen hydrogels, the reader is directed to reviews [10, 11] as well as several experimental studies [21, 26-30]. For the reader interested in dynamic remodeling of ECM, excellent reviews by Lu et al. (general perspective on ECM degradation and remodeling) [31] and Baaijens et al. (collagen-specific remodeling) [32] are recommended.

3.3 Collagen Hydrogel Fabrication Parameters

Most collagen hydrogels are prepared using type I collagen, which comprises 90% of the protein in human connective tissues [14, 20] and is easily extracted from animal tissue with minimal contamination by other collagens or proteins. Type I collagen is a triple helical protein formed of 67-nm periodic polypeptide chains with a total molecular weight near 300 kDa [14, 33]. Collagen fibrils self-assemble at neutral pH into bundled fibers typically 12-120 nm diameter that cross-link to produce a matrix structure [11, 34-36] which ultimately forms a hydrogel in the presence of a water-based solvent.

3.3.1 Collagen Source and Solubilization

Several groups have demonstrated that the collagen source (e.g. rat tail tendon, porcine skin, bovine skin) influences hydrogel properties [12, 20, 37]. Relationships between collagen source

and polymerization kinetics, hydrogel mechanics, and fiber structure are discussed in more detail in Sections 3.4.1-0. Furthermore, the method by which collagen is extracted from tissue has been shown to alter the molecular structure of the collagen fibrils as well as the kinetics of assembly [12, 38]. Acid solubilization is most commonly used for minimally cross-linked collagens such as rat tail tendon, while a combination of neutral salt solution with proteolytic extraction (pepsin digestion) is often used in order to fully denature highly cross-linked collagens from bovine or porcine skin [11, 20]. Many combinations of collagen sources, solubilization techniques, and solvents are in use for preparation of collagen stock solutions. Furthermore, collagen stock solutions, even those produced commercially, have been found to have significant batch-to-batch variation [12, 14]. A review of some of the collagen stock solutions referenced in the literature reveals that there is little consistency (Figure 3-1).
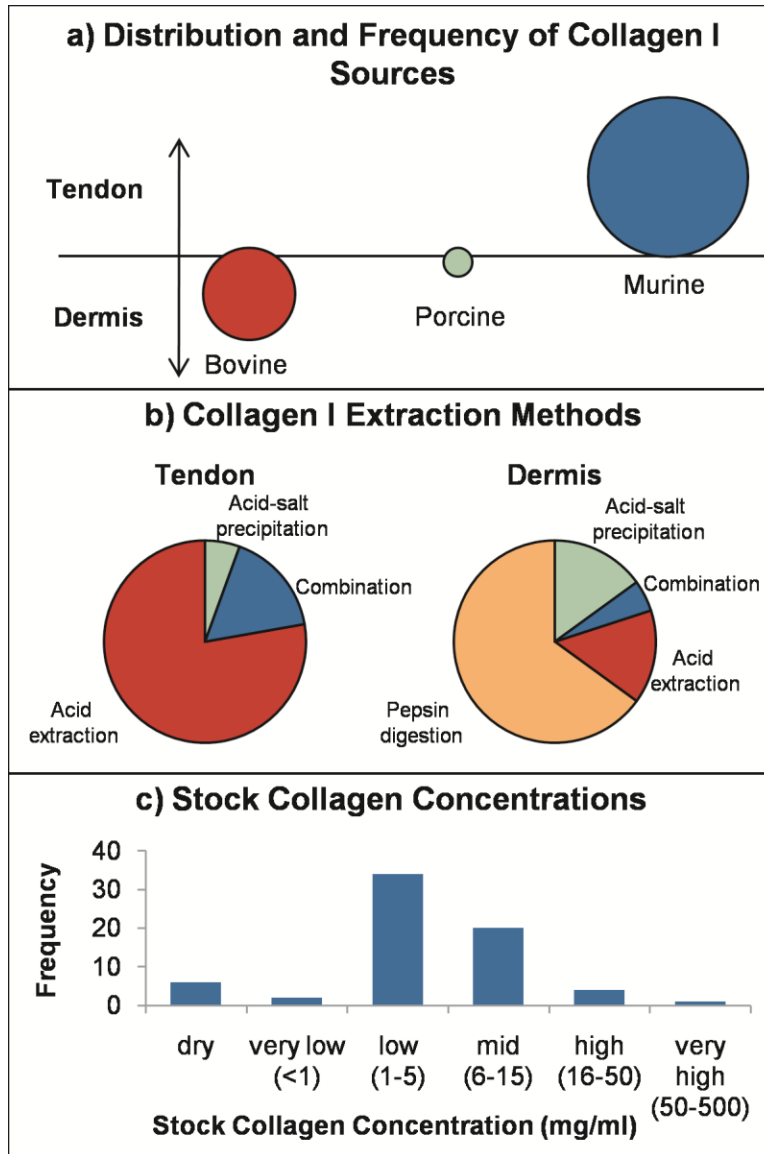
Figure 3-1: Overview of collagen I sources and solubilization methods. Source data can be found in the Appendix (Table 3-2).

Figure 3-1 shows the distribution of collagen source, solubilization, and stock solution concentrations obtained from a survey of over 50 research articles, listed in Appendix A (Section 3.7.1, Table 3-2). While it was not possible to include all collagen hydrogel-based publications in this review, this sample size is large enough to provide information representative of the field. In Figure 3-1(a), each bubble corresponds to a source species with the bubble diameter corresponding to relative frequency of experiments using that source. Vertical bubble placement indicates to what extent each tissue type (tendon or dermis) is used from each source species. Figure 3-1(a) shows that rat tendons represent the primary source of collagen I for hydrogel

19

research, although the contribution of bovine dermal tissue is comparable. Porcine tendon and dermis are infrequently used. Figure 3-1(b) provides a breakdown of extraction methods used for each tissue type (regardless of species).

Figure 3-1(b) indicates that collagen denaturation methods in use are relatively consistent with the degree of crosslinking for each source tissue: minimally-crosslinked collagens sourced from tendons are denatured using acid alone, while dermal collagens, with their high crosslink density, require pepsin digestion or other complex denaturation procedures.

Finally, Figure 3-1(c) is a histogram of stock solution concentrations reported in the literature. Whether extracted in-house or obtained commercially, stock concentrations are most commonly in the range 1-5 mg/ml which is lower than the collagen content of many native tissues. As noted in the following sections, this limitation has implications for the utility of collagen hydrogels as tissue mimics.

3.3.2 Collagen Concentration

Collagen concentration *in vitro* and *in vivo* influences tissue mechanical properties, thereby regulating cellular behavior [39-41]. It is suggested to play a role in tumor malignancy, as cancerous tissue contains 9-45 mg/ml (0.9-4.5% wt.) collagen in the interstitium while normal tissue contains significantly less [19]. Most research characterizing collagen hydrogels examines limited and disjoint ranges of collagen concentration, as demonstrated by Figure 3-2, which presents the distribution of collagen hydrogel concentrations found in the literature (Appendix A (Section 3.7.1): Table 3-3). The majority of these studies were performed within the last decade. In this plot, bubble location corresponds to the range of concentrations examined by each source. If only a single collagen concentration was used for a study, the bubble falls on the dashed line. Studies investigating broader concentration ranges are represented by bubbles centered further from the dashed line. Bubble diameter is not linked to concentration range, but rather indicates number of publications with identical conditions. Bubble color indicates bubbles of the same size. Each red bubble represents a single study. The large blue bubble, located at 2 mg/ml, represents the majority of publications.
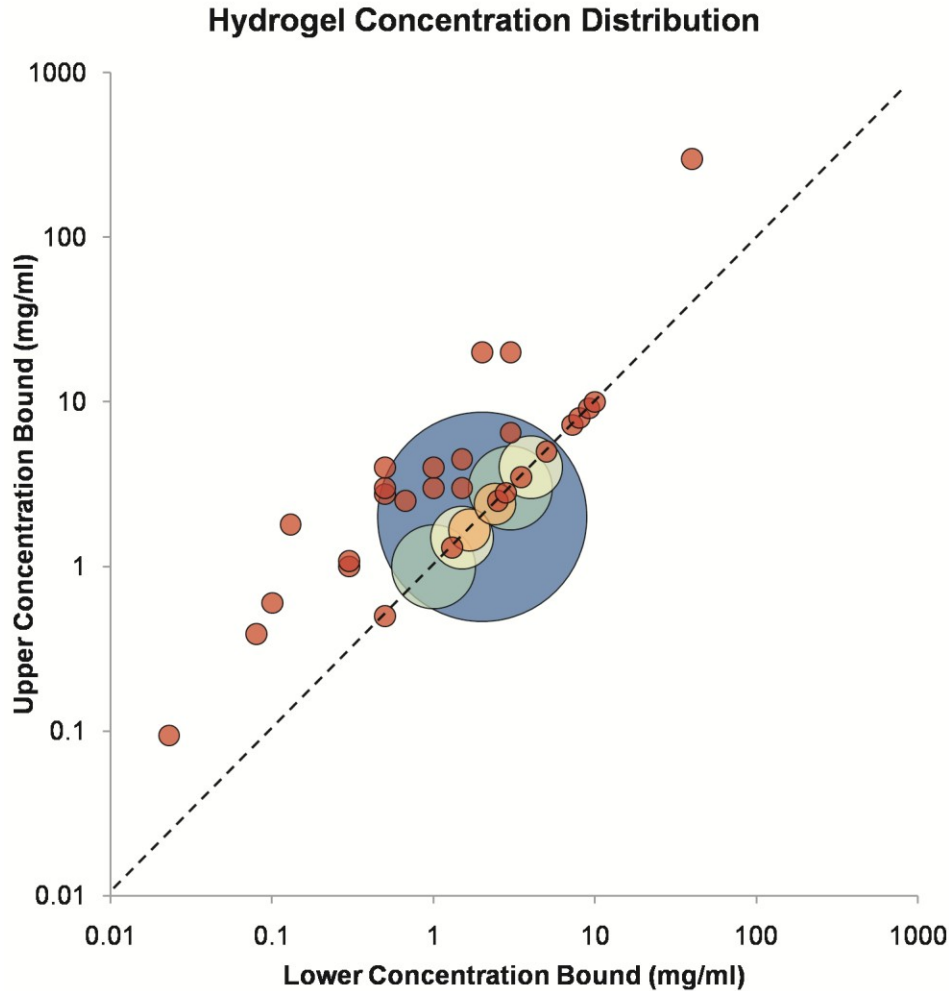
Figure 3-2: Collagen concentration ranges used in the tissue engineering literature.
Source data can be found in the Appendix (Table 3-3). 1 mg/ml = 0.1% wt.

Although most tissue mimics have been fabricated using hydrogels with low collagen content (< 4 mg/ml), as shown in Figure 3-2, they have limited value for mimicking 3D tissues due to their non-physiological strength and microstructure, which result in an inability to support microfabrication as bulk gels [42, 43]. Their use in characterization experiments is likely because most commercially available formulations are provided at low concentrations (see Figure 3-1(c), Appendix A (Section 3.7.1): Table 3-2). Conversely, gels with extremely high collagen content (>20 mg/ml) form a fiber structure too dense to permit cell migration and viability [43]. Finally, Figure 3-2 reveals that, as most previous works use single-concentration hydrogels (represented by the bubbles centered along the dashed line), the majority of the literature provides no insight into the effect of varying collagen concentration on gel characteristics and cell response. Notable

exceptions include Ramanujan et al. and Erikson et al., who examined the influence of collagen concentration over practical ranges (0-45 and 2-20 mg/ml, respectively) on both diffusivity and fiber structure and found a decrease in diffusion rate and decrease in fiber length and organization with increased collagen concentration [19, 27]. Cross et al. performed an in-depth study of the relationship between collagen concentration and hydrogel properties including stiffness and fiber structure, as well as cellular response [43]. For further information on correlations of collagen concentration (as well as other fabrication parameters) with hydrogel properties, the reader is directed to the subsequent sections.

Control of collagen concentration in hydrogels is most easily and accurately achieved using lyophilized collagen, as the reconstitution step permits accurate weight measurement of dry collagen and volume measurement of solvent to obtain the stock solution concentration. The Sirius Red colorimetric assay [44] is commonly used to measure the quantity of soluble collagen in stock solutions [45].

3.3.3 Polymerization Temperature

Along with collagen content, temperature of polymerization significantly affects hydrogel properties. Because reaction kinetics are temperature-dependent, self-assembly of collagen molecules occurs more rapidly at higher temperature and results in fibers with a lower number of bundled fibrils, resulting in a less ordered structure [26, 46] and consequently altered mechanical, structural, and transport properties as discussed in later sections. While most previous studies have used hydrogels polymerized at 37°C to facilitate cell seeding and viability, polymerization at room temperature (20-26°C) or below is not uncommon but generally inhibits inclusion of cells within the hydrogel. Chrobak et al. found inconsistent hydrogel formation at polymerization temperatures below 19°C [42]; however, as other groups have successfully polymerized collagen hydrogels at temperatures down to 4°C, this is likely unique to their experimental protocol. Yang et al. and Raub et al. varied polymerization temperature between 4 and 37°C to control fiber structure without necessitating variation in concentration and noted that polymerization at low temperatures produced the most desirable pore size for cellular proliferation [26, 46]. Similarly, Chrobak et al. found that gels formed at room temperature can be used to create microchannels with better stability and less degradation over time than those formed at 37°C [42]. Table 3-1 summarizes polymerization temperatures found in the literature.

Polymerization temperature (°C)	Reference(s)
Single temperature	
4 (refrigeration)	[31]
20-26 (room temperature)	[16, 29, 33, 39, 46-48]
37	[13, 14, 17, 20, 22, 28, 35, 38, 42, 49-75]
Range of temperatures	
4, 21, 37	[34]
4, 14, 24, 37	[27]
12-37	[76]
23, 37	[41]
Temperature gradient during polymerization	
4 -> 37	[77]
(4, 26, 35) -> 4 -> (4, 26, 35)	[37]
(22, 27, 32) -> 37	[45]

Table 3-1: Polymerization temperature of collagen hydrogels used for tissue engineering.

Polymerization temperature is difficult to control accurately, as temperature-dependent fiber self-assembly initiates as soon as the solution is neutralized. Most groups work with solutions on ice or in an ice chamber to slow polymerization until the hydrogel is well mixed, at which time it is moved to a chamber at the appropriate polymerization temperature. Therefore, the exact temperature of the hydrogel during the initial stages of polymerization is heterogeneous and regulated by convection and conduction. These effects cannot be strictly controlled in practice; however, if fabrication procedures are consistent, mixing is performed rapidly, and the polymerizing solution is moved immediately from ice to a temperature-controlled chamber, the properties of the final hydrogel are typically reproducible.

3.3.4   Polymerization pH

pH during fabrication strongly influences both structural and mechanical properties of the collagen hydrogel [34, 46, 47]. Yamamura et al. created hydrogels with pH ranging from 5-10 and found a strong positive correlation between pH and compression modulus [13], and Raub et al. found similar trends with hydrogels polymerized at pH in the range 5.5-8.5 [34]. Sung et al. and Gobeaux et al. studied the influence of pH on fiber size and organization across pH ranges of 7.1-8.3 and 6-12, respectively, as discussed in detail in Section 0 [47, 48]. Although gels polymerized at extreme pH may provide favorable properties for tissue mimics, for practical purposes pH of cellularized hydrogels is restricted to 7.4-8.4, as cell viability suffers outside this range [48, 49]. Achilli and Mantovani bypassed this restriction by first polymerizing hydrogels at pH = 10 and subsequently rinsing with buffer to return the pH to 7.4 before seeding cells on the

23

surface of the gel [35]. Although adequate cell viability was achieved with this method, it is not realistic for experiments in which cells must be seeded throughout the gel [21].

Figure 3-3 provides an overview of collagen hydrogel compositions in the literature (Appendix A (Section 3.7.1): Table 3-4). Similarly to Figure 3-2, Figure 3-3 (a) is a bubble plot indicating pH of collagen hydrogels, where bubble position shows pH values and range (if any), bubble size represents frequency in the literature, and bubble color indicates bubbles of the same size. Many publications did not report pH values for their hydrogels, but instead stated that the solution was at "neutral" or "physiological" pH. For graphical purposes, these studies were grouped together and plotted in Figure 3-3 at pH = 7.4 (green), but kept separate from those studies in which pH was specifically noted to be 7.4 (blue) so that the distinction could be visualized. Figure 3-3 (b), (c), and (d) show the breakdown of buffers, neutralization agents, and other components found in collagen hydrogels, respectively. The most common component in each class is highlighted in bold in the legend.
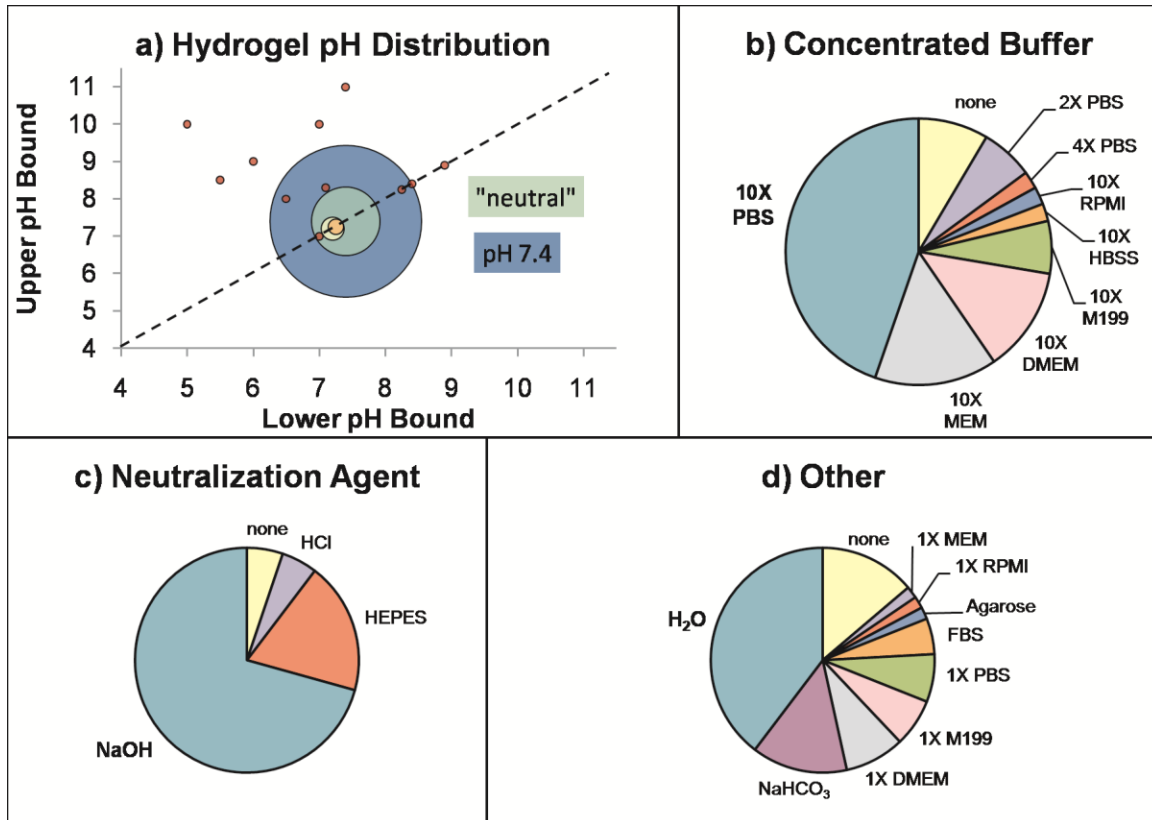
Figure 3-3: Collagen hydrogel configurations used in the tissue engineering literature.
a) pH ranges. b-d) Distribution of non-collagen hydrogel components. Components in bold occur most frequently and match the commercial BD/Vitrogen hydrogel preparation protocols. Source data can be found in the Appendix (Table 3-4).

Since early hydrogel studies have been primarily concerned with comparison of cell response in two-dimensional vs. three-dimensional culture, hydrogels have typically been polymerized at a physiological pH at or near 7.4 (Figure 3-3). As a result, published protocols and manufacturer guidelines use "recipes" for proportions of reagents required to obtain hydrogels at pH 7.4. Because pH is a fabrication parameter that can be exploited, at least within the range of cell viability (7.4-8.4), for design of tunable hydrogels, a single recipe is no longer adequate and calibration experiments must be performed.

pH of collagen hydrogels is not only dependent on the ratio of neutralization agent) to acid-solubilized collagen, but also buffer type and preparation, dilution ratio of collagen in hydrogel, and even absolute collagen concentration. Figure 3-3 indicates that one reagent stands out in each category: 10X phosphate buffered saline (PBS) as the concentrated buffer, sodium

hydroxide (NaOH) for neutralization, and distilled water for dilution. However, this unique combination of parameters was used in less than one-fourth of the studies surveyed for Figure 3-3 (Appendix A (Section 3.7.1): Table 3-4). Because of the variation in reagents comprising hydrogels used by different research groups (Figure 3-3), pH should be verified for each individual configuration. A sample pH calibration for the reagents used by our group, with varying collagen concentration, is provided in Figure 3-4. Details of the experimental methodology used to obtain the data for Figure 3-4 are provided in Appendix B (Section 0).
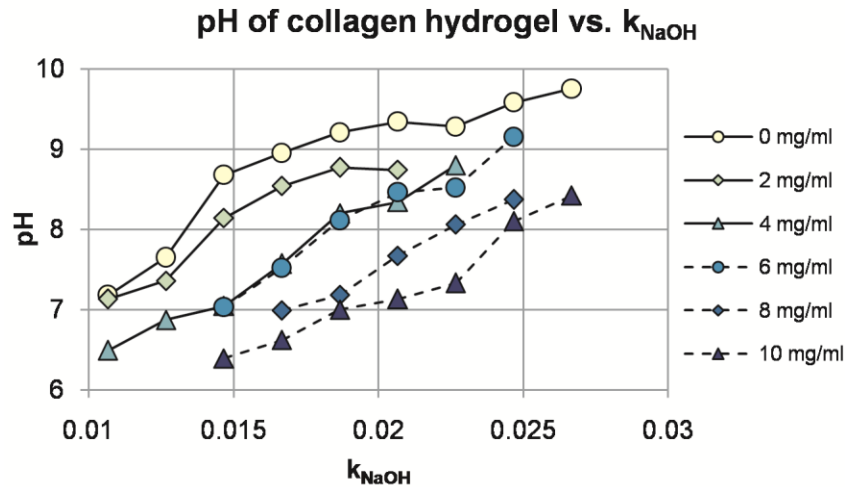
Figure 3-4: Dependence of hydrogel pH on NaOH fraction and absolute collagen concentration.

Collagen hydrogels are often fabricated using culture medium containing phenol red, which provides a useful visual indicator of pH. pH paper is also valuable for estimation of hydrogel pH, especially those fabricated using phenol red-free media or PBS, although it lacks sufficient accuracy for studies which require precise pH regulation. Electronic pH probes provide the most accurate measurements; however, they require immersion of the electrode tip in solution and, therefore, large sample volumes which may be impractical for some applications.

3.3.5 Ionic Strength
Finally, ionic strength has been demonstrated to affect hydrogel polymerization and subsequently structural and mechanical properties as described in later sections [46]. Gobeaux et al. varied ionic strength from 24-1300 mM for very high concentration gels (>75 mg/ml) polymerized at pH of 7.4, and measured resulting changes in hydrogel optical and structural properties [47].

Achilli and Mantovani varied ionic strength over a much smaller range, from 64.2-174 mM, but still found a significant effect on polymerization and mechanical properties [35].

Although few publications directly report ionic strength of collagen hydrogels, most recipes utilize 10X buffers (media or PBS) diluted to 1X strength in the final hydrogel in order to obtain hydrogel ionic strength similar to that of standard buffer solutions (Appendix A (Section 3.7.1): Table 3-4). Reported values using such recipes fall within the range 130-300 mM [12, 21, 34, 46, 50-54]. Finer control of ionic strength has been achieved by adjusting the concentration of phosphate in the buffer or adding sodium chloride (NaCl) to the hydrogel [35, 47, 54]. Ionic strength is seldom measured directly for collagen hydrogels, but rather calculated from known or estimated concentrations of all ionic compounds present in solution [54].

3.4 Collagen Hydrogel Characteristics

The following sections describe polymerization, mechanics, structure, and transport of collagen hydrogels. Each section provides a brief overview of the importance of the parameter for tissue engineering as well as information about current measurement techniques. Finally, correlations of each property with fabrication parameters as well as other properties are described.

3.4.1 Polymerization

As noted in previous sections, the kinetics of collagen fiber network assembly, a multi-step process including fibril formation, fiber nucleation and development, and cross-linking, is dependent on almost all fabrication parameters [12, 26, 38, 46, 47, 54]; furthermore, the addition of external crosslinking agents also affects fibrillogenesis [21, 55]. Polymerization kinetics provide insight into the molecular processes linking controllable fabrication parameters with the final state of the hydrogel. For example, Kreger et al. examined how collagen source and extraction method affect material properties [12]. Under identical polymerization conditions, they determined that acid-solubilized collagens polymerize more rapidly than pepsin-digested collagens and noted that these results are consistent with previous research indicating that telopeptides, which are damaged or destroyed by pepsin digestion, play a key role in fiber nucleation [12].

27

The importance of characterization of polymerization becomes clear when one considers that the ideal polymerization temperature or pH to achieve target structural or mechanical properties may not align with optimum conditions for viability in cell-seeded gels. In particular, lag time before polymerization begins and duration of polymerization are critical parameters for the design of mixing and incubation protocols to maximize viability.

Fibrillogenesis is frequently measured through spectrophotometric measurements of hydrogel turbidity, which have been demonstrated to correlate with degree of polymerization [12, 38]. Most previous works have measured turbidity at 313 nm [21, 38, 54] or 405 nm [12, 55] using standard spectrophotometric equipment with temperature controlled sample chambers. Total change in absorbance (ΔAbs) as well as three temporal parameters – lag time (t_L), polymerization rate (dAbs/dt), and half-time ($t_{1/2}$) – can be easily quantified from typical turbidity data (Figure 3-5). Duration of polymerization (twice the half-time) is strongly dependent on temperature but is typically on the order of 10 minutes to several hours [12, 35] for most applications.
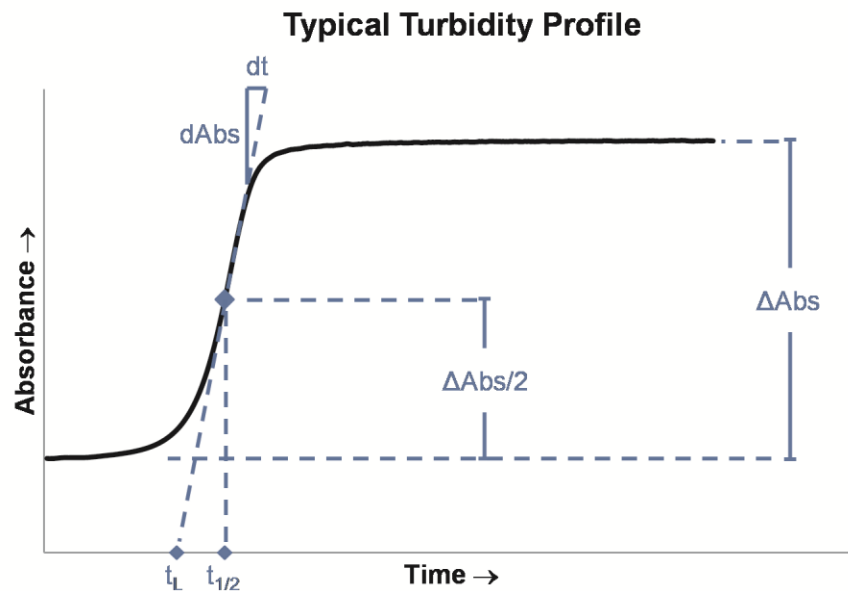
Figure 3-5: Diagram of a typical spectrophotometric measurement for quantification of polymerization. The polymerization half-time $t_{1/2}$ is defined as the time at which half of the total change in absorbance ΔAbs/2 is attained. The rate of change of absorbance at the half-time is defined as the polymerization rate dAbs/dt, while the lag time is defined as the zero-absorbance intercept of the line with slope dAbs/dt and intersecting $(t_{1/2}, \Delta Abs/2)$.

28

3.4.2 Mechanics

The influence of ECM stiffness on cell biology – including morphology, cytoskeletal stiffness, adhesion, migration, and proliferation – has been well-established; however, these effects have not yet been quantified for many cell types [9, 18, 39, 56-59]. The relationship between tissue elasticity and cell signaling and response has significant implications for many types of disease, especially cancer. In fact, increased ECM stiffness, along with elevated collagen concentration, is a hallmark of many tumors [60-62]. ECM stiffness has also been linked with endothelial integrity and consequently regulation of angiogenesis [13, 63-65]. The link between tissue stiffness and cell response has two major implications for tissue engineering using collagen hydrogels. For *in vitro* hydrogels meant to mimic specific tissues, hydrogel mechanical properties must be matched to the corresponding *in vivo* tissue properties in order to obtain physiologic behavior of cells in the hydrogel. Alternatively, hydrogel mechanical properties must be varied in a controlled fashion in order to answer outstanding questions about cell behavior in normal and disease states.

While the term "stiffness" is used in the preceding paragraph in a general sense to describe the mechanical resistance to deformation of a material (tissue or hydrogel), it cannot be used for meaningful discussions of material properties because it is strictly an extrinsic, structure-dependent property. Mechanical properties must first be defined in terms of specific types of deformation: tension, compression or shear. All of these deformation modes are commonly used in practice for characterization of biological tissues and care must be taken to avoid attempts to compare measurements obtained in different deformation modes. The elastic moduli of biological tissues have been reported to range from 10^2 Pa (brain) to 10^8 Pa (tendon) [66]. However, due to the different deformation modalities used to obtain these and similar *in vivo* data (elastic modulus can refer to either tensile or compression modulus), comparisons can seldom be drawn between such measurements [17, 58, 66, 67]. Furthermore, because soft biological tissues as well as collagen hydrogels are nonlinear viscoelastic materials, mechanical properties are both time- and strain-dependent. If only a single value is reported for an experimental study, an implicit approximation of linear elasticity (whether acknowledged or not) is made, and special attention must be paid to the experimental conditions under which the measurement was obtained.

Characterization of collagen hydrogel mechanical properties must be performed so that resulting measurements can be matched with *in vivo* data: this implies matching both deformation modality and temporal/strain characteristics. Although full mechanical characterization of viscoelastic parameters under all three deformation modalities is possible using dynamic mechanical analysis (DMA) in tension, compression, and torsion; this is not practical for many researchers and furthermore corresponding data for *in vivo* tissue is seldom available. As an alternative, if the physiologically relevant type of deformation, strain range, and timescale can be identified, more limited characterization may be sufficient for adequate ECM matching. For example, tendon and muscle often undergo rapid tension, relatively high strains, and are furthermore anisotropic. In contrast, physiological deformation of brain or breast tissue is more commonly quasi-steady-state compression. Fortunately, most tissues undergo relatively small strains under physiological conditions and exhibit linear behavior within this regime, simplifying analysis [67].

A significant amount of literature exists for mechanical characterization of collagen hydrogels covering a wide range of measurement methodologies, time and strain scales. Figure 3-6 provides a comparison of experimental settings used to estimate tensile, compression, and shear moduli. The inverse of the strain rate is plotted on the abscissa as a characteristic time, while the strain (expressed in %) is plotted on the ordinate as a characteristic length. As an example, Yamamura et al. performed confined compression of collagen hydrogels deforming at 0.01 (1%) strain/s from 5-15% strain; this study is plotted at (100s, 10%) with a bar extending to (100s, 15%) to indicate the strain range used to estimate compression modulus [13]. From the figure, it is clear that tensile and compression tests are generally performed with long time scales and at relatively high strains in order to best estimate relaxation moduli, while oscillatory shear measurements are performed at much shorter time scales and smaller strains in order to obtain additional information about the viscous component of deformation. Chandran and Barocas provide an excellent review of experimental methodologies for each deformation mode, discussing underlying physics and highlighting advantages and limitations of each [68].
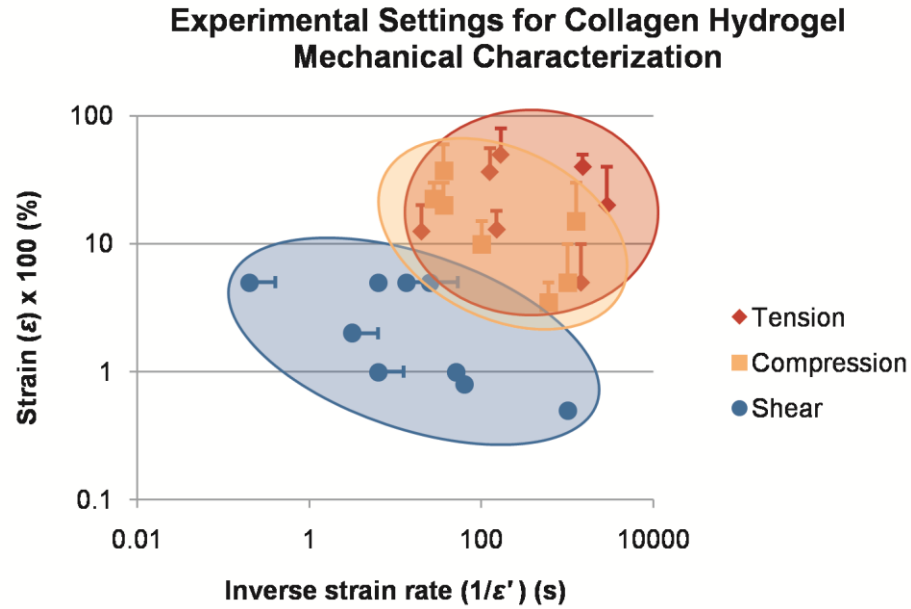
Figure 3-6: Modes and physical scales of collagen hydrogel mechanical characterization.
Data points corresponding to studies investigating a range of scales are centered at the mean value and
plotted with a bar extending to the upper bound of the range investigated. Because of the log-log scale, lower
bounds are not plotted. Source data and application notes can be found in the Appendix (Table 3-5).

In all deformation modes, it is critical to maintain sample integrity by humidification or immersion in a buffer solution during measurements; furthermore, high-resolution load cells must often be used in order to resolve the small forces associated with compliant hydrogels. Tensile tests in particular require simultaneous imaging of the specimen gauge region in order to quantify the cross-sectional area obtain an accurate measurement of true strain. In tension, failure stress and strain are often of interest in addition to the elastic modulus. Compression testing can be performed using either confined or unconfined samples. In both cases, accurate positioning of the platen at the sample surface to avoid sample preloading can be difficult. Surface tension at the interface can further complicate matters; this effect has previously been minimized through the use of a porous platen (especially for confined compression) [43, 68] or hydrophobic platen [69]. Oscillatory shear measurements generally require initial frequency and shear sweeps to determine the boundaries of linear response; most of the literature has concluded that approximately 1 Hz and 5% strain produce linear response in collagen hydrogels. Although atomic force microscopy (AFM) is extensively used for localized tissue and cell mechanical

measurements [7, 58], it is poorly suited for measurement of bulk properties due to the heterogeneity of collagen hydrogels [70].

The effect on mechanical properties of each of the fabrication parameters described in this review has been quantified. Both collagen source and solubilization affect hydrogel mechanics [12]. All studies investigating the effect of collagen concentration on hydrogel elastic and shear moduli demonstrate positive correlation [12, 40, 43, 51, 53, 63]. Similarly, increasing pH increases all metrics of collagen hydrogel modulus [13, 34, 35, 51]. The relationship between ionic strength and compression modulus is less straightforward, and appears to be interdependent with pH and temperature [35]. Crosslinking agents, by design, increase mechanical properties of hydrogels [15, 21, 26, 28, 30, 40, 59].

In general, there is poor agreement between quantitative mechanical measurements in the literature, not only due to differences in deformation mode and timescale but also variation in hydrogel fabrication parameters. This becomes especially apparent when conflicting correlations are found; for instance, Achilli and Mantovani determined that increasing polymerization temperature from 4 - 37°C decreases mechanical properties, with negligible correlation at pH = 7 but strong correlation at pH = 10 [35]. These results contradict the findings of Raub et al. several years earlier [26] where mechanical properties increased by two orders of magnitude over the same temperature range, but at a pH of 7.4. Differences between these studies such as collagen concentration ([26]: 2 mg/ml; [35] 4 mg/ml) and deformation mode ([35] characterized tensile and compression moduli while [26] investigated only shear modulus) may explain the discrepancy; however, further characterization is clearly necessary to fully understand the relationship between hydrogel mechanical properties and polymerization temperature. Furthermore, more detailed reporting of hydrogel fabrication protocols in order to highlight similarities and differences would assist the reader in accurately interpreting mechanical characterization data.

3.4.3 Structure

It is well known that the fiber structure of extracellular matrix can regulate cellular morphology, proliferation, migration, and gene expression [9, 13, 39, 46, 60, 71], and is therefore an important parameter for hydrogel characterization. Fiber structure in collagen gels is complex and often

defined quantitatively in terms of parameters such as mean fiber diameter D, fiber density (or volume fraction), pore size P, degree of cross-linking (or number of cross-links per fiber), and orientation Ø (Figure 3-7). These parameters can be used to help elucidate the cellular characteristics described above; for example, fiber orientation describes anisotropy of the material and can therefore be a predictor of directionality of cell migration.
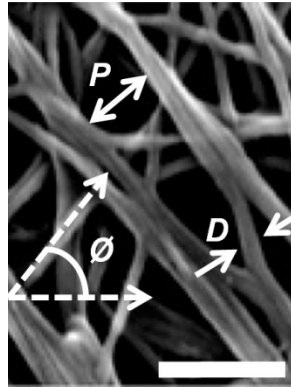
Figure 3-7: Representative SEM image of collagen hydrogel (34) annotated to indicate commonly quantified fiber structure parameters P (pore size), D (fiber diameter), and Ø (orientation). Scale bar 500 nm. Figure reproduced with permission of the publisher.

Several methodologies for measurement of hydrogel fiber structure are available. AFM has similar limitations for fiber structure imaging as for mechanical characterization: measurements are too localized for accurate estimation of bulk network properties. Historically, collagen hydrogel fibers have been imaged using scanning electron microscopy (SEM) [50, 52, 72] and transmission electron microscopy (TEM) [38, 54] for qualitative/semi-quantitative analysis of network and fibril structures, respectively. Although these methods provide high-resolution images and preserve relative information about fiber dimensions [26], they require significant sample manipulation, drying, and chemical processing. These can lead to shrinkage and collapse of the fiber structure, which prevent quantitative analysis of 3D fiber structure and SEM images [14, 20, 26, 34, 48]. While more advanced electron microscopy techniques such as cryo-SEM and environmental SEM have been developed which do not require sample dehydration, these still necessitate high vacuum or sample fixation which can alter the structure of the hydrogel.

Although electron microscopy remains in use for high-resolution imaging of hydrogel topology where quantitative results are not necessary, its limitations have led to the development of optical imaging techniques for fiber structure measurement of fully hydrated, unmodified hydrogels.

These include two closely related techniques, two-photon fluorescence (TPF) and second harmonic generation (SHG), as well as confocal reflectance and fluorescence microscopy (CRM/CFM), all of which have become popular modalities for recording fiber structure as they can be used to obtain images of gels in the hydrated state [20, 26]. Figure 3-8 provides a qualitative comparison of sample images acquired using each of these modalities.
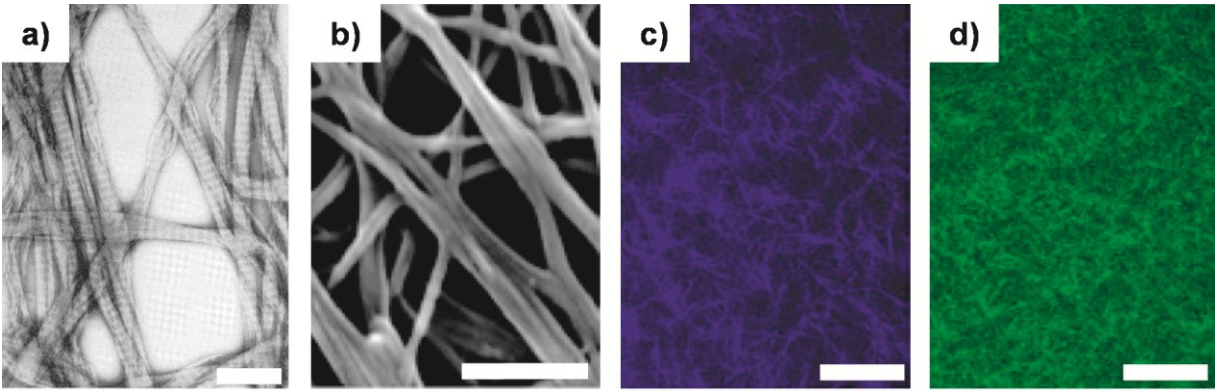
Figure 3-8: Representative images of collagen hydrogels using various modalities.
a) TEM (38) (scale bar 500nm) b) SEM (34) (scale bar 500 nm) c) SHG (34) (scale bar 50 μm) d) CRM (34) (scale bar 50 μm). Figures reproduced with permission of the publishers.

TPF and SHG are both based on two-photon laser excitation and therefore have the advantages associated with near-infrared illumination: i.e. high penetration depth and low phototoxicity. Furthermore, the use of fluorescence or second-harmonic generation provides good signal-to-noise ratio due to suppression of background light. However, they require high laser power and have difficulty penetrating dense tissue [20]. CRM, although somewhat noisier than TPF or SHG due to non-specificity of reflected light, is more commonly used, most likely due to availability of necessary equipment. CRM is an established technique in which images are formed by the light reflected from collagen fibers. Because reflected light does not undergo a spectral shift, CRM requires replacement of the microscope's fluorescent excitation filter with a beamsplitter (typically 80/20) and removal of the emission filters. This permits the reflected light to reach the microscope detector, which is usually a photomultiplier tube for laser-scanning confocal microscopes. CRM has been successfully performed across a range of wavelengths (405-543 nm) and magnifications (40-63X using water or oil immersion objectives).

For all three optical modalities, the distance of the focal plane into the hydrogel is a critical parameter. It has been demonstrated that collagen fibers form a significantly different network at

the surface of the coverslip than within the gel; therefore, images acquired too close to the coverslip produce misleading information and are likely a source of inconsistencies in fiber structure data in the literature [39]. Therefore, the distance of the focal plane from the sample surface should be clearly reported with all fiber structure data. Furthermore, the overall hydrogel thickness has been shown to influence hydrogel network formation for gels at or below 1.5 mg/ml collagen concentration [39]; although hydrogels for 3D tissue engineering generally require higher concentrations at which this effect is negligible, this dimension should nonetheless be clearly stated in experimental methodologies.

Regardless of imaging modality, quantitative analysis of fiber network images is necessary for extraction of structural parameters. Although many researchers have investigated collagen hydrogel network structure, no standard automated image analysis technique has yet emerged and therefore wide variation exists in published structural characteristics. Approaches in recent publications utilize algorithms exploiting a wide range of image segmentation and thresholding techniques [12, 21, 26, 27, 34, 40, 43, 46, 53, 55, 73], grid-based estimation [27, 39, 73], and even Fourier transforms and autocorrelation [34, 39, 74]. Furthermore, manual estimation of dimensions of user-identified fibers and pores is not uncommon [12, 13, 21, 34, 37, 50, 72, 75]. Finally, existing algorithms do not appear to be robust enough to accurately analyze images with a high density of fibers, a parameter primarily regulated by collagen concentration. For example, although Kreger et al. investigated polymerization kinetics and mechanical properties of 0.5-4 mg/ml hydrogels, fiber structure data is notably absent for samples above 3 mg/ml [12]. With one exception [43], which presents fiber structure images inconsistent with other publications, no studies have been found which present fiber structure analysis of collagen hydrogels >4 mg/ml collagen concentration. This is a significant limitation, as collagen hydrogels below this concentration, while initially widely studied, have not been successfully matched to *in vivo* tissues and in particular lack sufficient structural integrity to support microfabrication and perfusion [19, 42, 43, 76].

All collagen fabrication parameters discussed in this review have been demonstrated to influence one or more metrics of fiber structure. Increasing collagen concentration has been correlated with increased fiber density and reduced pore size but has no effect on fiber diameter [12, 19, 40, 47, 51, 52, 55, 72, 77]. However, increasing pH or temperature promotes electrostatic interactions

and fiber nucleation, accelerating polymerization and produce fibers with reduced diameter and networks with small pore size [26, 34, 35, 46, 48, 51]. Similarly, decreasing ionic strength of the hydrogel produces decreased fiber diameter and pore size [35, 47].

Although correlation between collagen source and fiber structure is difficult due to differences in collagen extraction and hydrogel preparation, it has been shown that the monomer/oligomer ratio can be used to control the degree of crosslinking within the collagen network [53]. In a review by Wolf et al., it is shown that pepsin-digested collagens, most often those produced from bovine tendon or porcine skin (Figure 3-1, Appendix A (Section 3.7.1): Table 3-2), produce fiber networks with long fibers and large pores compared to non-pepsin treated collagens such as that extracted from rat tail tendon (Figure 3-1, Appendix A (Section 3.7.1): Table 3-2) [20]. They conclude that this due to the reduction in fiber nucleation sites due to telopeptide removal [20]. Carey et al. suggested that the culture medium used in hydrogel fabrication (PBS, MEM, DMEM or M199) influences hydrogel fiber structure but that this relationship is negligible relative to the effect of other fabrication parameters [39]. Sung et al. indicated a difference in fiber shape depending on the neutralization medium used to fabricate the hydrogel (HEPES or NaOH) [48].

Fiber structure has often been measured in conjunction with other material properties such as polymerization kinetics [12, 21, 38, 47, 54, 55], mechanical properties [12, 13, 16, 21, 26, 30, 34, 35, 40, 43, 46, 50, 51, 53, 78, 79], or diffusivity [19, 27, 73, 79]. The goal of such experiments is usually development of predictive models which eliminate the need for time-consuming, expensive measurement of all relevant properties. However, because of the interdependence of properties on fabrication parameters, such correlations have value only under limited conditions.

3.4.4 Transport

Oxygen, nutrients, and other soluble bioactive molecules in avascular tissue are primarily transported by diffusion [27, 80]. Quantification of diffusion processes is a key step to understanding transport limitations within tumors [19, 62] as well as designing effective drug delivery strategies [27]. Because diffusion requirements are application-dependent, thorough characterization of the transport properties of collagen hydrogels is necessary before hydrogels can be designed to match desired properties [10].

The diffusive capacity of a hydrogel, characterized by the diffusion coefficient D, depends on both the gel fiber structure and the size and shape of the diffusing species [10]. The effective diffusion coefficient of a molecule in a collagen hydrogel can be estimated from the diffusion coefficient of the molecule in the interstitial fluid if the fiber structure (permeability and fiber shape characteristics) is known [8, 19]; however, a far more reliable estimate can be obtained by direct measurement using the method of fluorescence recovery after photobleaching (FRAP) [19, 80-82]. FRAP is an well-established experimental technique in which a fluorescent probe is homogenously distributed in the diffusion medium, locally bleached, and imaged in a time series to produce an intensity decay profile from which the diffusion coefficient can be measured based on Fick's second law. Using a confocal microscopy, high-resolution data can be obtained and no calibration is necessary. For further details on the method and analysis, see Seiffert and Opperman [81].

The fluorescent probe used in FRAP measurements in collagen hydrogels is often an easily labeled model protein such as dextran [19, 27, 73, 80] because it is available in a wide range of molecular weights and thus can be matched to a molecule of interest. Bioactive molecules in ECM range from small soluble cytokines and growth factors, with molecular weight on the order of 10^0 - 10^1 kDa [10, 80, 83, 84], to large insoluble macromolecules such as glycosaminoglycans and proteoglycans, with molecular weight on the order of 10^2 - 10^3 kDa [80]. Examples of other molecular probes which have been used for FRAP diffusivity measurements include bovine serum albumin (BSA) and lactalbumin [19]. It should be noted that care must be taken when performing FRAP using a molecule different than the molecule of interest as molecular weight matching may not be sufficient to mimic all ECM interactions [80].

For FRAP measurements, the thickness of the hydrogel is typically limited to several hundred microns to limit out-of-plane diffusion and background noise. It should be noted that, due to the possible dependence of fiber structure on gel thickness [39], this may introduce error when extrapolating FRAP diffusion measurements to thicker hydrogels. FRAP samples are usually formed between coverslips, on special multiwell slides, or in similar molds [19, 27, 73]. The fluorescent probe can be introduced during hydrogel fabrication [73] or by soaking the polymerized gel in probe-containing medium for 12-72 hours [19, 27, 79, 80]. FRAP in collagen hydrogels has most often been performed using laser-scanning confocal microscopy. While wide

variation exists in the literature in choice of imaging parameters such as resolution, magnification, and bleach region size and shape, most measurements require use of all available lasers at full power to obtain sufficient bleaching.

Ramanujan et al. successfully used FRAP to measure the diffusion coefficient of dextrans with a wide range of molecular weights (4-2000 kDa) in collagen hydrogels and correlated decreased diffusivity with an increase in collagen concentration [19]. Erikson et al. performed similar experiments with 2000 kDa dextran in collagen supplemented with decorin or hyaluronan [27], and Gillette et al. measured the diffusion coefficient of 3-500 kDa dextrans in collagen/alginate hydrogels [73]. Stylianopoulos et al. predicted using numerical models that the ionic strength of the hydrogel solution can affect the diffusion of charged particles [85]. To our knowledge, the effects of collagen source and solubilization, hydrogel pH, and hydrogel polymerization temperature on diffusion rates in collagen hydrogels have not yet been experimentally investigated.

3.5   Concluding Remarks

Significant progress has been made in recent years towards characterization of polymerization, mechanical, structural, and transport properties of collagen hydrogels. However, the full potential of many aspects of hydrogel characterization is yet to be realized. The community has not yet reached consensus on a deformation modality for mechanical characterization, even within specialized applications such as microvascular tissue engineering or tumor engineering. Because individual studies are often restricted to measurements using a single deformation modality, it remains unclear how different modalities correlate with one another. With respect to fiber structure characterization, accurate methods for quantification of structural parameters in hydrogels above 3 mg/ml are generally not available. This is a significant limitation, as the current trend is towards the use of higher concentration hydrogels due to improved replication of the properties of *in vivo* tissue. Furthermore, data for diffusion of bioactive molecules in collagen hydrogels remains extremely limited. The relationships between hydrogel transport properties (diffusivity) and many fabrication parameters including collagen source and concentration, polymerization temperature, and polymerization pH, have not yet been investigated. Finally, a

physics-based predictive model for one or more material properties, based on fabrication parameters, would be of great benefit to the entire community working with collagen hydrogels.

In this review, we note that the literature appears to contain contradictions with respect to material properties of collagen hydrogels, which we trace back to differences in fabrication protocols and characterization techniques. In order to minimize such ambiguities, it is necessary that researchers report fabrication and measurement protocols in increased detail, including seemingly inconsequential information. Such transparency will improve interpretability of the data on collagen hydrogel characterization, and facilitate future research efforts in this promising field.

3.6   Acknowledgements

3.7 Appendices

3.7.1 Appendix A: Supplementary Tables

Table 3-2: Collagen I sources and solubilization methods.

Source	Manufacturer (if applicable)	Solubilization	Solvent of final solution	Stock collagen concentration	Reference(s)
Bovine					
Dermis	Advanced BioMatrix (Vitrogen 100/PureCol)	pepsin digestion	0.01-0.012N HCl	~3 mg/ml	[12, 16, 19, 27, 29, 55, 71, 72, 76, 79, 86-88]
	Roche (Collagen S)	0.5M acetic acid	unknown	unknown	[14]
	Sigma	acid-salt precipitation	0.01M HCl	n/a (lyophilized)	[12, 51]
	Organogenesis	unknown acid	unknown	2.2 mg/ml	[68, 78]
Tendon	Sigma	sodium phosphate precipitation	0.01M HCl	10 mg/ml	[36, 89]
Porcine					
Dermis	in-house extraction	HCl + NaN3, pepsin digestion	0.5M (3%) acetic acid	10 mg/ml	[30]
	in-house extraction	acid-salt precipitation	0.01M HCl	n/a (lyophilized)	[12, 53, 90]
Tendon	Nitta Gelatin, Inc. (Cellmatrix Type 1-A)	unknown acid	unknown	3 mg/ml	[13]
	in-house extraction	NaCl + HCL, pepsin digestion	0.01N acetic acid	n/a (lyophilized)	[89]
Rat Tail					
Tendon	BD Biosciences "low concentration"	0.5M acetic acid	0.01-0.02M acetic acid	3-4 mg/ml	[48, 60, 63, 88, 91-94]
	BD Biosciences "high concentration"	0.5M acetic acid	0.01-0.02M acetic acid	8-11 mg/ml	[12, 21, 26, 34, 40, 42, 46, 73, 85, 95, 96]
	Sigma	0.1M acetic acid	0.1M acetic acid	2 mg/ml	[77]
	in-house extraction	0.1% acetic acid	0.1% acetic acid	8-30 mg/ml	[43]
	in-house extraction	unknown acid	0.017M (0.1%) acetic acid	10 mg/ml	[39]
	in-house extraction	acid-salt precipitation with 0.5 M acetic acid	0.5 M acetic acid	0-500 mg/ml	[47]
	in-house extraction	acid-salt precipitation and pepsin digestion	0.005M acetic acid	0.20-0.21 mg/ml	[54]
	in-house extraction	acid-salt precipitation and pepsin digestion	0.5M acetic acid	2 mg/ml	[38, 97]
	in-house extraction	0.5M acetic acid	0.02M acetic acid	5 mg/ml	[21]
	in-house extraction	0.5M acetic acid	HCl	4.29 mg/ml	[28]
	in-house extraction	0.02M acetic acid	0.02M acetic acid	1.4-44 mg/ml	[35, 50, 52]
	in-house extraction	acid-salt precipitation	unknown	5 mg/ml	[15]
	in-house extraction	0.01M HCl	0.01M HCl	12-20 mg/ml	[98]

40

Table 3-3: Collagen concentration in hydrogels used for tissue engineering.

1 mg/ml = 0.1% wt.

Collagen concentration (mg/ml)	Reference(s)
Single concentration	
0.5	[16]
1	[46, 60, 73, 78]
1.3	[48]
1.5	[16, 63, 88]
1.67	[29, 71]
2	[35, 60, 74-76, 86, 87, 91, 92, 94]
2.4	[13, 79]
2.5	[99]
2.8	[35]
3	[28, 63, 68, 93]
3.5	[100]
4	[21, 26, 34]
5	[15]
7-7.5	[95]
8	[98]
9.15	[85]
10	[30]
Concentration Range	
0-45	[19]
0.08-0.39	[38]
0.1-0.6	[50]
0.13-1.8	[55]
0.023-0.094	[54]
0.3-1.0	[52]
0.3-1.08	[77]
0.5-2.75	[53]
0.5-3	[90]
0.5-4	[12]
0.67-2.5	[72]
1-3	[51]
1-4	[40]
1.5-3	[39]
1.5-4.5	[96]
2-20	[27]
3-6.5	[42]
3-20	[43]
40-300	[47]

41

Table 3-4: Polymerization pH and components in collagen hydrogels used for tissue engineering.

pH	Concentrated buffer	Neutralization agent	Other components	Reference(s)
Single pH				
~7.0-7.5	10X PBS	NaOH	H2O, sodium bicarbonate	[42, 95]
7.0	none	NaOH	DMEM, MEM, RPMI, M199, PBS	[39]
7.2	10X M199	HEPES	H2O, sodium bicarbonate	[50]
	10X DMEM	NaOH/HCl	none	[79]
	10X MEM	none	sodium bicarbonate	[71]
7.4	10X PBS	NaOH	H2O	[12, 19, 26, 27, 53, 63, 73, 93, 94] (BD, Vitrogen protocol)
	10X PBS	NaOH	1X PBS	[21]
	10X MEM	none	sodium bicarbonate, FBS	[72]
	10X MEM	NaOH, HEPES	1X M199	[76]
	10X MEM	NaOH, HEPES	1X PBS	[68]
	10X MEM	NaOH, HEPES	FBS	[78]
	none	NaOH	1X DMEM, agarose	[16]
	10X DMEM	NaOH	1X DMEM	[96]
	10X DMEM	NaOH, HEPES	H2O, sodium bicarbonate, FBS	[46]
	10X M199/RPMI	NaOH, HEPES	H2O, sodium bicarbonate	[52]
	10X HBSS	NaOH	1X DMEM sodium bicarbonate	[77]
neutral/ physiological (exact pH not specified)	10X M199	NaOH	1X M199	[43]
	10X MEM	NaOH	1X M199	[87]
	10X PBS	NaOH	H2O	[29, 40, 55, 86]
	2X PBS	HEPES	none	[60]
	10X PBS	NaOH, HEPES	1X PBS	[75]
	none	NaOH	none	[85]
8-8.5	10X DMEM	NaOH	none	[28]
8.4	10X DMEM	NaOH	1X DMEM	[98]
8.9	10X DMEM	NaOH	H2O	[92]
pH range				
5-10	10X MEM	NaOH/HCl, HEPES	none	[13]
5.5-8.5	10X PBS	NaOH	dH2O	[34]
6-9	modified 10X PBS	none	none	[51]
6-13	modified PBS	NaOH	none	[47]
6.5-8.0	modified 2X PBS	NaOH/HCl	none	[54]
7-10	none	NaOH, HEPES	H2O	[35]
7.1-8.3	4X or 2X PBS	NaOH or HEPES	none	[48]
7.4-11	10X PBS	NaOH	H2O	[91]

42

Table 3-5: Review of collagen hydrogel mechanical characterization.

Deformation mode	Time scale of deformation	Strain scale of deformation	Parameters varied	Highlights of Study	Ref.
Single-mode studies					
Tension	0.067%/s	30-50%	Collagen concentration, polymerization pH	Fiber structure imaging (confocal reflectance) during strain application; longer, thinner fibers correlate with higher strain	[51]
	0.07%/s	0-10%	Addition of polymers (including collagen) to PLGA hydrogels	Collagen strengthens PLGA hydrogels	[18]
	0.67%/s	8-18% (break)	Addition of GAGs, fibroblasts to collagen hydrogels	GAGs increase tensile modulus; fibroblasts reduce modulus	[28]
	0.8%/s	17-56% (break)	Addition of various crosslinkers to collagen hydrogels	Crosslinkers increase tensile strength but reduce extensibility	[15]
	1.67%/s	not stated	Collagen concentration	Studied EC traction in constrained or floating hydrogels; found larger capillary structures in constrained gels	[63]
	5%/s (step) followed by relaxation	5-20%	Addition of agarose (varying concentration) to collagen hydrogels	Agarose slows hydrogel relaxation and reduces hydrogel compressibility	[78]
Compression (unconfined)	0.167%/s	2-5%	Addition of GAGs	GAGs increase compression modulus	[59]
Compression (confined)	0.1%/s	0-10%	none	Anisotropy measurement during strain application; find that interstitial flow and fiber bending regulate stress response	[68]
	1%/s	5-15%	pH	Compression modulus increases with pH; ECs grown on rigid hydrogels migrate less but form deeper networks	[13]
	Step (rate unspecified) followed by relaxation	3-20%	Collagen concentration	Compression modulus increases with collagen concentration	[43]

Deformation mode	Time scale of deformation	Strain scale of deformation	Parameters varied	Highlights of Study	Ref.
Single-mode studies (continued)					
Shear (oscillatory)	0.016-16 Hz	2%	Addition of protein supplements	Collagen breaks down under shear with oscillation frequency above 3 Hz	[50]
	0.1 Hz	0.5%	Collagen concentration, addition of glutaraldehyde	G' increases with concentration but pore size decreases; decoupled pore size and shear modulus and found cell spreading and migration depend primarily on pore size	[40]
	0.1-1 Hz	not stated	Addition of protein supplements	Fibronectin or laminin supplements at high concentration reduce G' and G" of hydrogels	[79]
	0.1-100 Hz	5%	Temperature, addition of glutaraldehyde	G', G" frequency-independent at 5% strain; shear moduli increase with temperature, addition of GA	[26]
	0.4 Hz	5%	Addition of agarose	Agarose increases G' but leaves gross fiber structure unchanged	[16]
	0.5-1 Hz	5%	Collagen vs. fibrin	Fibrin stiffer than collagen at same concentration	[86]
	1 Hz	0.8%	Polymerization temperature	Modified temperature and measured shear moduli throughout polymerization; final G', G" decrease slightly at higher temperatures	[46]
	1.6 Hz	5%	Polymerization pH	G', G" frequency-independent at 5% strain; shear moduli increase with pH	[34]
	0.1-10 Hz	n/a (0.5 Pa)	Addition of GAGs	Chondroitin sulfate increases ECM void fraction, decreasing shear modulus; dextran does not affect mechanical properties	[21]
Shear (creep)	n/a	n/a (9.5 Pa)	Addition of glutaraldehyde	GA increases shear modulus; Voigt-Kelvin model describes creep test well	[30]

44

Table 3-5 (continued): Review of collagen hydrogel mechanical characterization.

Deformation mode	Time scale of deformation	Strain scale of deformation	Parameters varied	Highlights of Study	Ref.
Multi-mode studies					
Tension	0.03-0.04%/s	0-40%	Polymerization temperature, pH, ionic strength	Tensile and compression moduli increase with pH; fabrication at physiological temperature and pH does not result in physiological strength	[35]
Compression (unconfined)	3.6%/s	15-30%			
Tension	0.6%/s	20-80%	Collagen source, concentration	High oligomer content may be linked to increased hydrogel strength	[12]
Compression (unconfined)	2.76%/s	15-60%			
Shear (oscillatory)	1Hz	1%			
Compression (unconfined)	2.76%/s	10-30%	Collagen concentration, molecular weight	Compression and shear moduli are positively correlated with oligomer content (molecular weight); effect is stronger than than of concentration	[53]
Shear (oscillatory)	1 Hz	1%			
Compression (confined)	0.08%/s for ramp tests	0-10%	none	Creep, ramp, and sinusoidal compression as well as oscillatory shear. Found that collagen hydrogels exhibit Maxwell behavior in both shear and compression with similar timescales; shear modulus is larger than compression modulus.	[76]
Shear (oscillatory)	0.016-16 Hz	1%			

45

3.7.2 Appendix B: Experimental methodology for data presented in Figure 3-4

Collagen I was obtained from rat tail tendon by solubilization in 0.01M HCl at 4°C overnight. Subsequently, the solution was centrifuged for 45 minutes at 30,000 g and the supernatant was removed, frozen, and lyophilized. Stock collagen solutions of 0- 20 mg/ml were obtained by reconstitution of lyophilized collagen in 0.01M HCl. Multiple stock solutions were prepared so that hydrogels of varying concentration could be fabricated while maintaining a 2:1 dilution factor for each.

Collagen hydrogels were fabricated by combining acidic collagen with a concentrated buffer (10X DMEM, no supplements, Sigma), neutralization agent (1N NaOH, Fisher), and physiological buffer (1X DMEM supplemented with glucose, sodium bicarbonate, and L-glutamine, Sigma). The volume fraction of each component was as follows: acidic collagen = 0.5, 10X DMEM = 0.1, NaOH = kNaOH = 0.0107-0.0267 (control variable), 1X DMEM = 0.373-0.389 (remaining volume).

3 mL hydrogels were prepared by combining all components over ice and stirring with a spatula. The data in Figure 4 were obtained at room temperature (23°C) using a glass pH electrode (Thermo) submerged in each hydrogel.

References

1. Kumar, V., et al., *Tissue Engineering of Blood Vessels: Functional Requirements, Progress, and Future Challenges.* Cardiovascular Engineering and Technology, 2011. **2**(3): p. 137-148.

2. Ingram, M., et al., *Tissue engineered tumor models.* Biotechnic & Histochemistry, 2010. **85**(4): p. 213-229.

3. Sung, J.H. and M.L. Shuler, *Microtechnology for Mimicking In Vivo Tissue Environment.* Annals of Biomedical Engineering, 2012. **40**(6): p. 1289-1300.

4. Buchanan, C. and M.N. Rylander, *Microfluidic culture models to study the hydrodynamics of tumor progression and therapeutic response.* Biotechnol Bioeng, 2013. **110**(8): p. 2063-72.

5. Tibbitt, M.W. and K.S. Anseth, *Hydrogels as extracellular matrix mimics for 3D cell culture.* Biotechnol Bioeng, 2009. **103**(4): p. 655-63.

6. Fischbach, C., et al., *Engineering tumors with 3D scaffolds.* Nat Methods, 2007. **4**(10): p. 855-60.

7. Kloxin, A.M., et al., *Mechanical Properties of Cellularly Responsive Hydrogels and Their Experimental Determination.* Advanced Materials, 2010. **22**(31): p. 3484-3494.

8. Hoffman, A.S., *Hydrogels for biomedical applications.* Adv Drug Deliv Rev, 2002. **54**(1): p. 3-12.

9. Aurand, E.R., K.J. Lampe, and K.B. Bjugstad, *Defining and designing polymers and hydrogels for neural tissue engineering.* Neurosci Res, 2012. **72**(3): p. 199-213.

10. Drury, J.L. and D.J. Mooney, *Hydrogels for tissue engineering: scaffold design variables and applications.* Biomaterials, 2003. **24**(24): p. 4337-51.

11. Parenteau-Bareil, R., R. Gauvin, and F. Berthod, *Collagen-Based Biomaterials for Tissue Engineering Applications.* Materials, 2010. **3**(3): p. 1863-1887.

12. Kreger, S.T., et al., *Polymerization and matrix physical properties as important design considerations for soluble collagen formulations.* Biopolymers, 2010. **93**(8): p. 690-707.

13. Yamamura, N., et al., *Effects of the mechanical properties of collagen gel on the in vitro formation of microvessel networks by endothelial cells.* Tissue Engineering, 2007. **13**(7): p. 1443-53.

14. Abraham, L.C., et al., *Guide to collagen characterization for biomaterial studies.* Journal of Biomedical Materials Research Part B-Applied Biomaterials, 2008. **87B**(1): p. 264-285.

15. Charulatha, V. and A. Rajaram, *Influence of different crosslinking treatments on the physical properties of collagen membranes.* Biomaterials, 2003. **24**(5): p. 759-67.

16. Ulrich, T.A., et al., *Probing cellular mechanobiology in three-dimensional culture with collagen-agarose matrices.* Biomaterials, 2010. **31**(7): p. 1875-1884.

17. Gribova, V., T. Crouzier, and C. Picart, *A material's point of view on recent developments of polymeric biomaterials: control of mechanical and biochemical properties.* Journal of Materials Chemistry, 2011. **21**(38): p. 14354-14366.

18. Levy-Mishali, M., J. Zoldan, and S. Levenberg, *Effect of Scaffold Stiffness on Myoblast Differentiation.* Tissue Engineering Part A, 2009. **15**(4): p. 935-944.

19. Ramanujan, S., et al., *Diffusion and convection in collagen gels: Implications for transport in the tumor interstitium.* Biophysical Journal, 2002. **83**(3): p. 1650-1660.

20. Wolf, K., et al., *Collagen-based cell migration models in vitro and in vivo.* Semin Cell Dev Biol, 2009. **20**(8): p. 931-41.

21. Stuart, K. and A. Panitch, *Influence of chondroitin sulfate on collagen gel structure and mechanical properties at physiologically relevant levels.* Biopolymers, 2008. **89**(10): p. 841-51.

22. Gronau, G., et al., *A review of combined experimental and computational procedures for assessing biopolymer structure-process-property relationships.* Biomaterials, 2012. **33**(33): p. 8240-8255.

23. Lu, P., V.M. Weaver, and Z. Werb, *The extracellular matrix: a dynamic niche in cancer progression.* J Cell Biol, 2012. **196**(4): p. 395-406.

24. Billiet, T., et al., *A review of trends and limitations in hydrogel-rapid prototyping for tissue engineering.* Biomaterials, 2012. **33**(26): p. 6020-41.

25. Miller, E.J. and R.K. Rhodes, *Preparation and characterization of the different types of collagen.* Methods Enzymol, 1982. **82 Pt A**: p. 33-64.

26. Raub, C.B., et al., *Noninvasive assessment of collagen gel microstructure and mechanics using multiphoton microscopy.* Biophysical Journal, 2007. **92**(6): p. 2212-22.

27. Erikson, A., et al., *Physical and chemical modifications of collagen gels: impact on diffusion.* Biopolymers, 2008. **89**(2): p. 135-43.

28. Saddiq, Z.A., J.C. Barbenel, and M.H. Grant, *The mechanical strength of collagen gels containing glycosaminoglycans and populated with fibroblasts.* J Biomed Mater Res A, 2009. **89**(3): p. 697-706.

29. Wolf, K., et al., *Amoeboid shape change and contact guidance: T-lymphocyte crawling through fibrillar collagen is independent of matrix remodeling by MMPs and other proteases.* Blood, 2003. **102**(9): p. 3262-9.

30. Sheu, M.T., et al., *Characterization of collagen gel solutions and collagen matrices for cell culture.* Biomaterials, 2001. **22**(13): p. 1713-9.

31. Lu, P., et al., *Extracellular matrix degradation and remodeling in development and disease.* Cold Spring Harb Perspect Biol, 2011. **3**(12).

32. Baaijens, F., C. Bouten, and N. Driessen, *Modeling collagen remodeling.* J Biomech, 2010. **43**(1): p. 166-75.

33. Kadler, K.E., et al., *Collagens at a glance.* Journal of Cell Science, 2007. **120**(12): p. 1955-1958.

34. Raub, C.B., et al., *Image correlation spectroscopy of multiphoton images correlates with collagen mechanical properties.* Biophysical Journal, 2008. **94**(6): p. 2361-73.

35. Achilli, M. and D. Mantovani, *Tailoring Mechanical Properties of Collagen-Based Scaffolds for Vascular Tissue Engineering: The Effects of pH, Temperature and Ionic Strength on Gelation.* Polymers, 2010. **2**(4): p. 664-680.

36. Gentleman, E., et al., *Mechanical characterization of collagen fibers and scaffolds for tissue engineering.* Biomaterials, 2003. **24**(21): p. 3805-13.

37. Parenteau-Bareil, R., et al., *Comparative study of bovine, porcine and avian collagens for the production of a tissue engineered dermis.* Acta Biomaterialia, 2011. **7**(10): p. 3757-3765.

38. Gelman, R.A., D.C. Poppke, and K.A. Piez, *Collagen fibril formation in vitro. The role of the nonhelical terminal regions.* J Biol Chem, 1979. **254**(22): p. 11741-5.

39. Carey, S.P., et al., *Biophysical control of invasive tumor cell behavior by extracellular matrix microarchitecture.* Biomaterials, 2012. **33**(16): p. 4157-65.

48

40. Miron-Mendoza, M., J. Seemann, and F. Grinnell, *The differential regulation of cell motile activity through matrix stiffness and porosity in three dimensional collagen matrices.* Biomaterials, 2010. **31**(25): p. 6425-35.

41. Zaman, M.H., et al., *Migration of tumor cells in 3D matrices is governed by matrix stiffness along with cell-matrix adhesion and proteolysis.* Proc Natl Acad Sci U S A, 2006. **103**(29): p. 10889-94.

42. Chrobak, K.M., D.R. Potter, and J. Tien, *Formation of perfused, functional microvascular tubes in vitro.* Microvascular Research, 2006. **71**(3): p. 185-196.

43. Cross, V.L., et al., *Dense type I collagen matrices that support cellular remodeling and microfabrication for studies of tumor angiogenesis and vasculogenesis in vitro.* Biomaterials, 2010. **31**(33): p. 8596-607.

44. Marotta, M. and G. Martino, *Sensitive spectrophotometric method for the quantitative estimation of collagen.* Anal Biochem, 1985. **150**(1): p. 86-90.

45. Rodriguez-Rodriguez, P., et al., *A simple dot-blot-Sirius red-based assay for collagen quantification.* Anal Bioanal Chem, 2013. **405**(21): p. 6863-71.

46. Yang, Y.L., S. Motte, and L.J. Kaufman, *Pore size variable type I collagen gels and their interaction with glioma cells.* Biomaterials, 2010. **31**(21): p. 5678-88.

47. Gobeaux, F., et al., *Fibrillogenesis in dense collagen solutions: a physicochemical study.* J Mol Biol, 2008. **376**(5): p. 1509-22.

48. Sung, K.E., et al., *Control of 3-dimensional collagen matrix polymerization for reproducible human mammary fibroblast cell culture in microfluidic devices.* Biomaterials, 2009. **30**(27): p. 4833-41.

49. Naciri, M., D. Kuystermans, and M. Al-Rubeai, *Monitoring pH and dissolved oxygen in mammalian cell culture using optical sensors.* Cytotechnology, 2008. **57**(3): p. 245-50.

50. Kuntz, R.M. and W.M. Saltzman, *Neutrophil motility in extracellular matrix gels: Mesh size and adhesion affect speed of migration.* Biophysical Journal, 1997. **72**(3): p. 1472-1480.

51. Roeder, B.A., K. Kokini, and S.L. Voytik-Harbin, *Fibril microstructure affects strain transmission within collagen extracellular matrices.* J Biomech Eng, 2009. **131**(3): p. 031004.

52. Saltzman, W.M., et al., *Three-dimensional cell cultures mimic tissues.* Ann N Y Acad Sci, 1992. **665**: p. 259-73.

53. Bailey, J.L., et al., *Collagen oligomers modulate physical and biological properties of three-dimensional self-assembled matrices.* Biopolymers, 2011. **95**(2): p. 77-93.

54. Williams, B.R., et al., *Collagen fibril formation. Optimal in vitro conditions and preliminary kinetic results.* J Biol Chem, 1978. **253**(18): p. 6578-85.

55. Brightman, A.O., et al., *Time-lapse confocal reflection microscopy of collagen fibrillogenesis and extracellular matrix assembly in vitro.* Biopolymers, 2000. **54**(3): p. 222-234.

56. Lo, C.M., et al., *Cell movement is guided by the rigidity of the substrate.* Biophysical Journal, 2000. **79**(1): p. 144-152.

57. Paszek, M.J., et al., *Tensional homeostasis and the malignant phenotype.* Cancer Cell, 2005. **8**(3): p. 241-254.

58. Brandl, F., F. Sommer, and A. Goepferich, *Rational design of hydrogels for tissue engineering: impact of physical factors on cell behavior.* Biomaterials, 2007. **28**(2): p. 134-46.

59. Haugh, M.G., et al., *Crosslinking and mechanical properties significantly influence cell attachment, proliferation, and migration within collagen glycosaminoglycan scaffolds.* Tissue Eng Part A, 2011. **17**(9-10): p. 1201-8.

60. Provenzano, P.P., et al., *Collagen density promotes mammary tumor initiation and progression.* Bmc Medicine, 2008. **6**.

61. Koumoutsakos, P., I. Pivkin, and F. Milde, *The Fluid Mechanics of Cancer and Its Therapy.* Annual Review of Fluid Mechanics, Vol 45, 2013. **45**: p. 325-355.

62. Polacheck, W.J., I.K. Zervantonakis, and R.D. Kamm, *Tumor cell migration in complex microenvironments.* Cell Mol Life Sci, 2013. **70**(8): p. 1335-56.

63. Sieminski, A.L., R.P. Hebbel, and K.J. Gooch, *The relative magnitudes of endothelial force generation and matrix stiffness modulate capillary morphogenesis in vitro.* Exp Cell Res, 2004. **297**(2): p. 574-84.

64. Saunders, R.L. and D.A. Hammer, *Assembly of Human Umbilical Vein Endothelial Cells on Compliant Hydrogels.* Cell Mol Bioeng, 2010. **3**(1): p. 60-67.

65. Califano, J.P. and C.A. Reinhart-King, *A Balance of Substrate Mechanics and Matrix Chemistry Regulates Endothelial Cell Network Assembly.* Cell Mol Bioeng, 2008. **1**(2-3): p. 122-132.

66. Levental, I., P.C. Georges, and P.A. Janmey, *Soft biological materials and their impact on cell function.* Soft Matter, 2007. **3**(3): p. 299-306.

67. Wells, R.G., *The role of matrix stiffness in regulating cell behavior.* Hepatology, 2008. **47**(4): p. 1394-1400.

68. Chandran, P.L. and V.H. Barocas, *Microstructural mechanics of collagen gels in confined compression: poroelasticity, viscoelasticity, and collapse.* J Biomech Eng, 2004. **126**(2): p. 152-66.

69. Evans, D.W., et al., *Nano-Indentation Device for Investigating the Mechanics of Compliant Materials.* Experimental Mechanics, 2013. **53**(2): p. 217-229.

70. Thiele, J., et al., *25th Anniversary Article: Designer Hydrogels for Cell Cultures: A Materials Selection Guide.* Advanced Materials, 2013.

71. Gunzer, M., et al., *Migration of dendritic cells within 3-D collagen lattices is dependent on tissue origin, state of maturation, and matrix structure and is maintained by proinflammatory cytokines.* J Leukoc Biol, 2000. **67**(5): p. 622-9.

72. Friedl, P., et al., *Migration of highly aggressive MV3 melanoma cells in 3-dimensional collagen lattices results in local matrix reorganization and shedding of alpha2 and beta1 integrins and CD44.* Cancer Research, 1997. **57**(10): p. 2061-70.

73. Gillette, B.M., et al., *Dynamic hydrogels: switching of 3D microenvironments using two-component naturally derived extracellular matrices.* Advanced Materials, 2010. **22**(6): p. 686-91.

74. Ng, C.P., B. Hinz, and M.A. Swartz, *Interstitial fluid flow induces myofibroblast differentiation and collagen alignment in vitro.* Journal of Cell Science, 2005. **118**(Pt 20): p. 4731-9.

75. Sundararaghavan, H.G., et al., *Neurite growth in 3D collagen gels with gradients of mechanical properties.* Biotechnol Bioeng, 2009. **102**(2): p. 632-43.

76. Knapp, D.M., et al., *Rheology of reconstituted type I collagen gel in confined compression.* Journal of Rheology, 1997. **41**(5): p. 971-993.

77. Sun, S., J. Wise, and M. Cho, *Human fibroblast migration in three-dimensional collagen gel in response to noninvasive electrical stimulus. I. Characterization of induced three-dimensional cell movement.* Tissue Engineering, 2004. **10**(9-10): p. 1548-57.

78. Lake, S.P. and V.H. Barocas, *Mechanical and Structural Contribution of Non-Fibrillar Matrix in Uniaxial Tension: A Collagen-Agarose Co-Gel Model.* Annals of Biomedical Engineering, 2011. **39**(7): p. 1891-1903.

79. Guarnieri, D., et al., *Effects of fibronectin and laminin on structural, mechanical and transport properties of 3D collageneous network.* J Mater Sci Mater Med, 2007. **18**(2): p. 245-53.

80. Leddy, H.A., M.A. Haider, and F. Guilak, *Diffusional anisotropy in collagenous tissues: fluorescence imaging of continuous point photobleaching.* Biophysical Journal, 2006. **91**(1): p. 311-6.

81. Seiffert, S. and W. Oppermann, *Systematic evaluation of FRAP experiments performed in a confocal laser scanning microscope.* J Microsc, 2005. **220**(Pt 1): p. 20-30.

82. Berk, D.A., et al., *Fluorescence photobleaching with spatial Fourier analysis: measurement of diffusion in light-scattering media.* Biophysical Journal, 1993. **65**(6): p. 2428-36.

83. Taylor, J.M., S. Cohen, and W.M. Mitchell, *Epidermal growth factor: high and low molecular weight forms.* Proc Natl Acad Sci U S A, 1970. **67**(1): p. 164-71.

84. Mcinnes, I., *Kelley's textbook of rheumatology*, G.S. Firestein and W.N. Kelley, Editors. 2009, Saunders/Elsevier: Philadelphia, PA.

85. Stylianopoulos, T., et al., *Diffusion of particles in the extracellular matrix: the effect of repulsive electrostatic interactions.* Biophysical Journal, 2010. **99**(5): p. 1342-9.

86. Raeber, G.P., M.P. Lutolf, and J.A. Hubbell, *Molecularly engineered PEG hydrogels: a novel model system for proteolytically mediated cell migration.* Biophysical Journal, 2005. **89**(2): p. 1374-88.

87. Shreiber, D.I., P.A. Enever, and R.T. Tranquillo, *Effects of pdgf-bb on rat dermal fibroblast behavior in mechanically stressed and unstressed collagen and fibrin gels.* Exp Cell Res, 2001. **266**(1): p. 155-66.

88. Haessler, U., et al., *Migration dynamics of breast cancer cells in a tunable 3D interstitial flow chamber.* Integr Biol (Camb), 2012. **4**(4): p. 401-9.

89. Huang, Y.C., et al., *Epidermal morphogenesis in an in-vitro model using a fibroblasts-embedded collagen scaffold.* Journal of Biomedical Science, 2005. **12**(6): p. 855-867.

90. Whittington, C.F., M.C. Yoder, and S.L. Voytik-Harbin, *Collagen-polymer guidance of vessel network formation and stabilization by endothelial colony forming cells in vitro.* Macromol Biosci, 2013. **13**(9): p. 1135-49.

91. Chung, S., et al., *Cell migration into scaffolds under co-culture conditions in a microfluidic platform.* Lab on a Chip, 2009. **9**(2): p. 269-275.

92. Polacheck, W.J., J.L. Charest, and R.D. Kamm, *Interstitial flow influences direction of tumor cell migration through competing mechanisms.* Proceedings of the National Academy of Sciences of the United States of America, 2011. **108**(27): p. 11115-11120.

93. Song, J.W. and L.L. Munn, *Fluid forces control endothelial sprouting.* Proc Natl Acad Sci U S A, 2011. **108**(37): p. 15342-7.

94. Jeon, J.S., et al., *In vitro model of tumor cell extravasation.* PLoS One, 2013. **8**(2): p. e56910.

95. Leung, A.D., K.H. Wong, and J. Tien, *Plasma expanders stabilize human microvessels in microfluidic scaffolds.* J Biomed Mater Res A, 2012. **100**(7): p. 1815-22.

96. Krishnan, L., et al., *Design and application of a test system for viscoelastic characterization of collagen gels.* Tissue Engineering, 2004. **10**(1-2): p. 241-252.

97. Chandrakasan, G., D.A. Torchia, and K.A. Piez, *Preparation of intact monomeric collagen from rat tail tendon and skin and the structure of the nonhelical ends in solution.* J Biol Chem, 1976. **251**(19): p. 6062-7.

98. Buchanan, C.F., et al., *Three-Dimensional Microfluidic Collagen Hydrogels for Investigating Flow-Mediated Tumor-Endothelial Signaling and Vascular Organization.* Tissue Eng Part C Methods, 2014. **20**(1): p. 11.

99. Zervantonakis, I.K., et al., *Three-dimensional microfluidic model for tumor cell intravasation and endothelial barrier function.* Proc Natl Acad Sci U S A, 2012. **109**(34): p. 13515-20.

100. Ng, C.P. and M.A. Swartz, *Fibroblast alignment under interstitial fluid flow using a novel 3-D tissue culture model.* Am J Physiol Heart Circ Physiol, 2003. **284**(5): p. H1771-7.

4 Tunable collagen I hydrogels for engineered physiological tissue micro-environments[*]

Elizabeth Antoine[1], Pavlos Vlachos[2], M. Nichole Rylander[3]

[1] Department of Mechanical Engineering, Virginia Tech, Blacksburg, Virginia, USA

[2] School of Mechanical Engineering, Purdue University, West Lafayette, Indiana, USA

[3] VT-WFU School of Biomedical Engineering and Sciences, Virginia Tech, Blacksburg, Virginia, USA

4.1   Abstract

Collagen I hydrogels are commonly used to mimic the extracellular matrix (ECM) for tissue engineering applications. However, the ability to design collagen I hydrogels to match the functionality of physiological tissues has been elusive. This is primarily due to the relative unavailability of quantitative correlations between fabrication parameters and resulting material properties. This study aims to enable informed design and fabrication of collagen hydrogels in order to reliably and reproducibly mimic a variety of soft tissues. We developed empirical predictive models relating fabrication parameters with material and transport properties. The models were obtained through extensive experimental characterization of these properties, which include stiffness, pore and fiber diameter, and diffusivity, within a large fabrication parameter space. Fabrication parameters were varied within biologically relevant ranges and included collagen concentration, polymerization pH, and polymerization temperature. This study elucidates previously unknown fabrication-function relationships; namely, we found that the effects on the compression modulus and the fiber structure of the fabrication parameters considered herein are each significant but independent of one another, while the concentration and polymerization temperature interactively regulate polymerization half-time with no significant contribution from pH. All fabrication parameters had a small but significant effect on diffusivity. The equations resulting from this study permit informed *a priori* design of collagen hydrogels with prescribed properties and functional performance. By enabling hydrogel fabrication by design, this study has the potential to greatly enhance the utility and relevance of collagen hydrogels for developing physiological tissue microenvironments for a wide range of tissue engineering applications.

---

[*] In preparation.

4.2 Introduction

Hydrogels using collagen I obtained from native tissues are in widespread use as scaffolds for 3D cell culture and tissue engineering. Historically, while desirable for tissue engineering due to their natural biocompatibility and similarity to native extracellular matrix (ECM) [1-3], collagen hydrogels have been at a disadvantage when compared with synthetic ECM mimics because of their complex nature [4, 5]. In order to effectively use collagen hydrogels for tissue engineering, the ability to optimize hydrogel material properties to better match those of the target tissue is essential [5, 6]; however, this is challenging because the properties of collagen hydrogels depend on a broad range of fabrication parameters, including but not limited to source tissue, solubilization method, pH and temperature of polymerization, solution components, ionic strength, and collagen concentration [7].

In recent years, significant effort has been devoted to characterization of functionally relevant bulk properties of collagen hydrogels in order to enable hydrogel design for specific applications. Functional properties including stiffness, fiber structure, and diffusivity of bioactive molecules have all been subject to investigation [8-13]. Stiffness is one of the key bulk properties used for tuning engineered scaffolds, as it regulates cell membrane stiffness, adhesion, differentiation, morphology, migration, and more [14-19]. The stiffness of hydrated biological tissues varies from 10^2 to 10^6 Pa [20]; therefore, characterization of collagen hydrogels with stiffness spanning a similar range is desirable. Fiber structure, another important factor for designing tissue-mimicking hydrogels, regulates cell morphology and migration [11, 15, 21-24]. In collagenous *in vivo* tissues, pore size is generally heterogeneous and can vary from 1 to 20 μm [11]. Nutrient transport and drug delivery within tissues are generally limited by diffusivity, which depends on both the tissue and the diffusing molecule.

Correlations of these functional properties with various fabrication parameters have been demonstrated; however, due to wide variation in fabrication protocols and characterization techniques used by different groups, the data is difficult to interpret and often in disagreement [7]. Furthermore, the relative influence of different fabrication parameters on hydrogel properties cannot be easily determined from the existing data, making it difficult to choose an optimal set of fabrication parameters for any given application.

In this study, we aim to fill this gap and measure the response of a set of hydrogel functional properties to three important fabrication parameters, varied within ranges that correspond to biological applications. The fabrication parameters under consideration here were (1) collagen concentration, (2) polymerization temperature, (3) polymerization pH, and (4) molecule size (for diffusion measurements). Concentrations of 4, 6, 8, and 10 mg/ml (0.4, 0.6, 0.8, and 1.0% wt.) were studied because this range has been shown to support microfabrication and cell culture while matching concentrations which are found in natural tissues [8, 25, 26]. Temperatures of 23°C and 37°C were selected because they are easily attainable in tissue engineering laboratories and support cell viability during polymerization. A pH range of 7.4-8.4 was selected because it represents the range over which cell growth can be maintained [27, 28] and several previous studies have suggested that pH can be a valuable tool for controlling hydrogel material properties [10, 13, 15]. Finally, fluorescently labeled dextrans with hydrodynamic radii mimicking cytokines and other bioactive molecules (1.4, 4.5, 6.0, and 8.5 nm corresponding to 4, 40, 70, and 150 kDa) were used for diffusion studies.

The functional properties characterized for this study were stiffness measured in confined compression, fiber structure evaluated in terms of fiber diameter and pore size and measured using confocal reflectance microscopy (CRM), and diffusivity measured using fluorescence recovery after photobleaching (FRAP). Furthermore, polymerization kinetics were measured using spectrophotometry in order to link and provide temporal metrics for design considerations such as device assembly time or dependence of cell viability on time spent at suboptimal temperature. These data were used to develop empirical models of the fabrication/function relationship for collagen I hydrogels as well as sensitivity analysis to understand the relative importance of each fabrication parameter for each functional property.

4.3 Experimental Methods

4.3.1 Preparation of Collagen Hydrogels

Type I collagen was acid-extracted as follows: Tendons removed from rat tails were added to 0.01 M (pH 2.0) hydrochloric acid (HCl, Sigma) at 4°C, with a volume of approximately 30 mL/tail. The solution was placed in an ice bath and stirred overnight using a magnetic stir plate. Subsequently, the solution was centrifuged at 30,000 g for 45 minutes to remove insoluble

55

components. The supernatant was frozen and lyophilized to obtain pure collagen protein. Lyophilized collagen was stored up to 6 months at -20°C.

For reconstitution, a mass of lyophilized collagen was weighed and added to an appropriate volume of 0.01 M HCl to achieve monomeric solution concentrations of 8, 12, 16, and 20 mg/ml. Collagen and acid were mixed thoroughly and allowed to reconstitute overnight at 4°C. Subsequently, the solution was mixed again and centrifuged for 60 seconds at 1800 *g* to remove bubbles. Monomeric collagen solutions were stored up to 6 weeks at 4°C.

Hydrogels were prepared by combining acidic monomeric collagen with concentrated buffer (10X Dulbecco's Modified Eagle's Medium (DMEM), Sigma), physiological buffer (1X DMEM supplemented with glucose, sodium bicarbonate, and L-glutamine, Sigma), and neutralization agent (1N sodium hydroxide (NaOH), Fisher) according to the following recipe (by volume): 0.1 units 10X DMEM, 0.5 units monomeric collagen solution, k_{NaOH} units 1N NaOH (dependent on desired pH and absolute collagen concentration, Equation 4-1), remaining units 1X DMEM. In order to obtain consistent hydrogel pH, a monomeric solution with twice the final hydrogel concentration was always used. A calibration formula for pH was obtained by adjusting absolute collagen concentration (maintaining the 2:1 dilution ratio) and NaOH fraction in hydrogels and measuring pH of the resulting solution:

$$k_{NaOH} = 0.0052 pH + 0.00051 C - 0.028 \qquad \textbf{Equation 4-1}$$

where k_{NaOH} is the volume fraction of 1N NaOH in the hydrogel and C is the collagen concentration in the hydrogel, in mg/ml.

For fabrication of all hydrogels, 10X DMEM, 1X DMEM, and 1N NaOH were mixed over ice. After the monomeric collagen was added, the solution was mixed thoroughly using a spatula, taking care to avoid bubble formation. The hydrogel was transferred to an application-specific mold (Figure 4-1) and incubated at either 23°C or 37°C for a duration at least twice the polymerization half-time as determined by kinetics measurements (described in the following section).

56
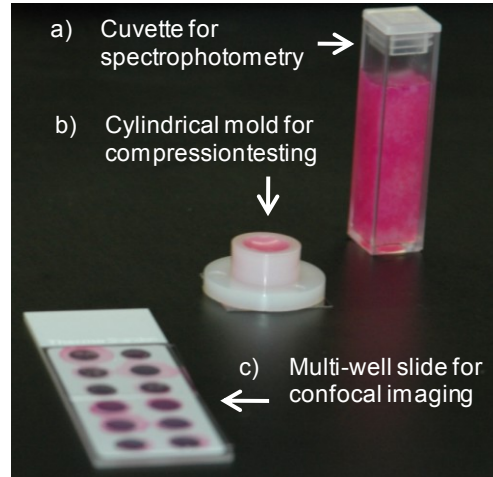
Figure 4-1: Hydrogel configurations for characterization.
a) capped cuvette for spectrophotometric kinetics measurements, b) cylindrical mold for confined compression measurements (confining plug not shown), c) multi-well slide for fiber structure and diffusion measurements. Samples shown are 4 mg/ml hydrogels polymerized at pH 8.4 and 37° C.

Hydrogels for polymerization kinetics measurements were prepared directly in polystyrene spectrophotometric cuvettes (Schaumaplast 10 mm lightpath, Fisher) (Figure 4-1a). After mixing, cuvettes were capped, placed into a spectrophotometer sample block preset to the desired incubation temperature with a Peltier device, and data recording begun immediately.

Hydrogels for stiffness measurements (confined compression) were prepared in 15mL centrifuge tubes. After mixing, 600uL volumes were dispensed using a syringe into cylindrical molds (Ø 9.5 mm, height 9.35 mm), sealed with coverslips to prevent evaporation, and polymerized in an incubator set to the desired temperature. The resulting cylindrical hydrogels had diameter 9.5 mm and height 8.5 mm (Figure 4-1b). After polymerization was complete, distilled water was placed on each sample to ensure full hydration.

For confocal imaging, solutions were prepared similarly to those for stiffness measurements but pipetted into multi-well slides (Shandon Multi-Spot Slides, Thermo) to obtain hydrogels approximately 100 um thick with diameter 6 mm (Figure 4-1c). Furthermore, during solution preparation, a portion of the 1X DMEM (1% of the total hydrogel volume) was replaced with an aqueous dextran solution (50 mg/ml for 1.4, 4.5, and 6.0 nm dextrans; 40 mg/ml for 8.5 nm dextran) for a final dextran concentration in the hydrogel of 0.4-0.5 mg/ml. The Stokes' radii R_H for FITC-dextrans (1.4, 4.5, 6.0 and 8.5 nm for 4, 40, 70, 150 kDa), which scale almost linearly

with the square root of the molecular weight, were obtained from the supplier (Sigma Product Information Sheet FD-4).

Fabrication parameters which can affect functional properties but were not varied in this study were selected to match those most prevalent in the literature. They include collagen source and solubilization (hydrochloric acid-extracted rat tail tendon), solution components (DMEM and NaOH), and ionic strength (~130 mM). The numerical data presented in this study should be interpreted in the context of these fixed parameters.

4.3.2   Polymerization Kinetics Experimental Methodology

Before characterization of functional properties, the kinetics of collagen self-assembly was measured. In this study, polymerization kinetics was quantified from spectrophotometric measurements of light absorbance in the sample during self-assembly, a parameter which has been shown to correlate with degree of polymerization [12, 29].Turbidity of the hydrogels was recorded throughout polymerization using a Cary 5000 UV-Vis-NIR spectrophotometer (Varian) equipped with a Peltier temperature controller. Absorbance at 405nm, zeroed against a reference sample of deionized water, was recorded every 3.6 seconds for up to 2 hours. Following Kreger et al. [12], four parameters were measured from the absorbance profiles: total change in absorbance ΔAbs, polymerization half-time $t_{1/2}$ (measured at the time at which half the total change in absorbance was achieved), polymerization rate $dAbs/dt$ (measured as the slope of the absorbance profile at the half-time), and lag time (t_L) (measured as the initial-absorbance intercept of the line intersecting [$t_{1/2}$, ΔAbs] with slope $dAbs/dt$) (Figure 4-2).
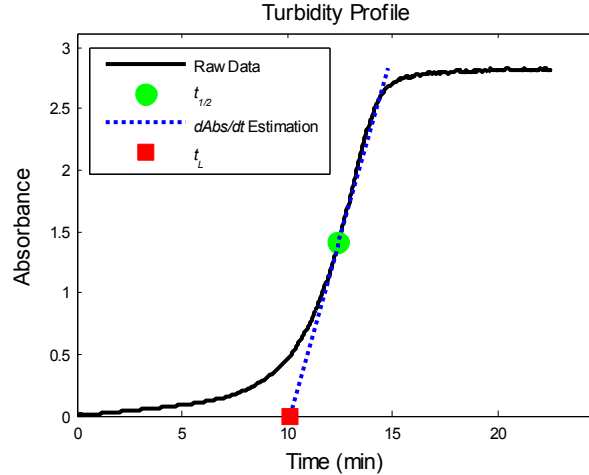
Figure 4-2: Representative turbidity profile annotated with quantitative metrics. Data shown is for 8 mg/ml collagen polymerized at pH 7.9 and 23°C.

4.3.3 Stiffness Experimental Methodology

Here we assumed that slow small-strain compression is the most relevant deformation mode for tissues mimicked by collagen hydrogels and that the hydrogel is linear elastic under such deformation; therefore we measured the stiffness of collagen hydrogels in quasi-steady uniaxial confined compression. Hydrogels were prepared as described in Section 4.3.1. Before compression, the coverslip was removed from each sample, a confining nylon plug (8 mm diameter, 6 mm height) was placed on the surface of the hydrogel and the entire sample assembly was placed on the lower platen of a mechanical load frame (Electroforce 3100, Bose) fitted with either a high-resolution low-force transducer (250 g_f, Honeywell) for 4 mg/ml samples or a low-resolution high-force transducer (22 N, Bose) for 6-10 mg/ml samples. The upper platen was lowered approximately to the upper surface of the plug and displaced 1.7 mm at a rate of 0.0085 mm/s. With a sample height of 8.5 mm, this protocol achieved 0.1% strain/s over a range of 0-20% strain. Stress was calculated from force response divided by the area of the nylon plug (50.3 mm^2). The radial gap between the nylon plug and sample confinement cylinder (0.75 mm) was designed to permit fluid to escape during confined compression. All measurements were performed at room temperature (23° C).

4.3.4 Stiffness Analysis

Due to inhomogeneities inherent in collagen hydrogels, escape of bubbles during compression, and imperfections in alignment of system components, stress measurements were not always

59

linear. Therefore, data filtering was necessary to obtain accurate stiffness estimates from slow-displacement measurements of collagen (Figure 4-3). As this has not been explicitly addressed in previous studies, we have developed a robust algorithm for an automated and fully objective analysis of compression data using MATLAB. First, initial contact of the upper platen with the sample was identified as the position at which the signal from the load cell deviated from the initial value by more than 5 times the sensor RMS noise (Figure 4-3a). Samples with greater than 5% thickness variation from the nominal value of 8.5 mm (425 µm), as determined by contact position, were discarded. Next, a robust loess-smoothing filter with a large kernel (75% of the data) was applied to minimize the effect of outliers and nonlinearities in the measurements and force/position were converted to stress/strain measurements (Figure 4-3b). Subsequently, a linear regression was performed on the robust loess-smoothed data between 5-15% strain (Figure 4-3c). At this point, samples with negative slope were discarded, as physics require that stiffness be positive. Finally, poroviscoelastic theory and previous experimental characterization indicate that collagen hydrogel compression modulus is nearly constant between 0 and 20% strain at low displacement rates [14]. Samples with strong nonlinearities due to experimental artifacts, identified as those with regression R^2 below 0.5, were discarded as unreliable.
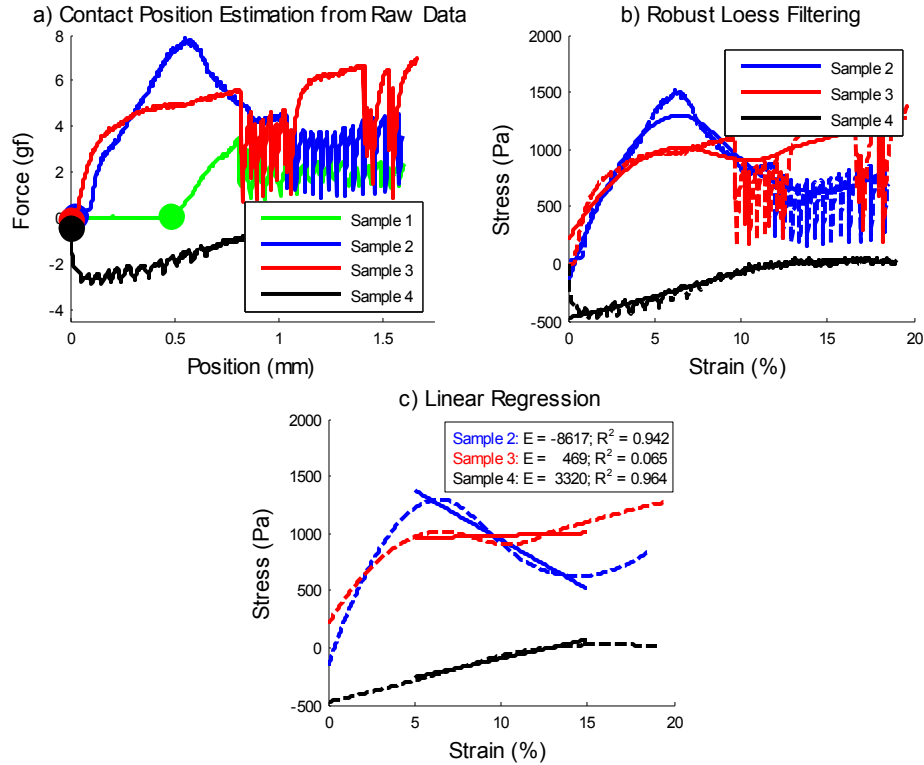
Figure 4-3: Analysis of compression data from four representative hydrogel samples.

All samples are 4 mg/ml, pH 8.4, 37°C. a) Identification of contact position, marked by a filled circle. b) Robust loess smoothing. c) Linear regression of smoothed data from 5-15% strain. Sample 1 (green) is discarded after step (a) because the sample thickness, determined from the contact position, is 6.9% (585 µm) less than the nominal thickness. Sample 2 (blue) is discarded after step (c) because E = -8617 Pa < 0. Sample 3 (red) is also discarded after step (c) because the regression R^2 = 0.065 < 0.5. Sample 4 (black) is considered valid and returns a compression modulus of 3320 Pa which contributes to the mean stiffness calculated for this fabrication condition.

4.3.5   Fiber Structure Experimental Methodology

In this study, confocal reflectance microscopy was used as it requires no sample preparation or drying and therefore provides accurate dimensional information of samples in the hydrated state [11]. Fiber structure images were acquired using a laser-scanning confocal microscope (LSM 510, Zeiss) configured with a 40X water immersion objective (C-Apochromat, NA=1.2), pinhole set to 1 Airy unit, and 80/20 beamsplitter to record reflected light from a 543 nm HeNe laser. The image size was set to 112.5 x 112.5 µm with a field of view of 2048 x 2048 pixels for a pixel resolution of 54.9 nm. Images were acquired in the center plane of the hydrogels in multi-well slides in order to maximize the distance from artificial boundaries.

61

4.3.6 Fiber Structure Analysis

In order to accurately evaluate fiber structure images for the relatively high collagen concentrations investigated in this study, an algorithm based on the Frangi vesselness enhancement filter [30] was implemented in MATLAB using the Image Processing Toolbox as well as algorithms available on the MATLAB File Exchange [31, 32]. Processing steps are demonstrated in Figure 4-4, beginning with a subset of a sample raw image (Figure 4-4a). First, histogram equalization *histeq* was applied to the fiber structure image. Subsequently, the Frangi vesselness filter was applied to enhance fibers (Figure 4-4b). The parameters for the vesselness filter were selected as follows: the first correction constant, which represents the deviation of the fibers from a blob-like structure, was set to 0.5 as suggested by Frangi [30]. Similarly, the second correction constant, which provides scaling based on the image intensity distribution, was selected as suggested by Frangi to be half the maximum Hessian norm for the image [30]. Finally, the range and step size of vessel scales in the filter kernel were specified based on an expected vessel diameter D_{exp} of 0.4 μm [12]. The scale range was set to 0.5 D_{exp} - 2 D_{exp} with a step size of 0.5 D_{exp}.

After enhancement of fiber structures using the Frangi vesselness filter, the image was binarized to obtain white fibers on a black background using Otsu's method for thresholding (Figure 4-4c). Subsequently, small objects which were unlikely to represent fibers were removed. The object size threshold for removal was the area corresponding to a circular region with diameter D_{exp}. Finally, morphological artifacts such as holes in fibers and small tendrils were eliminated using *imopen* and *imclose* with a disk-shaped structural element with diameter D_{exp} /4 (Figure 4-4d).

To determine fiber size, a distance map of the white regions (fibers) was computed using *bwdist* and skeletonized using *bwmorph* with option *skel*. The remaining pixel values, representing the distance of the central pixel of each fiber from the nearest background pixel, were taken as a measure of fiber radius. The distribution of fiber diameter is Figure 4-4e. Similarly, pore size was obtained from a distance map of the black regions (pores) followed by a shrink operation using *bwmorph* with option *shrink*. The remaining pixel values, representing the distance of the central pixel of each pore from the nearest fiber pixel, were taken as a measure of pore radius. The distribution of pore diameter is shown in Figure 4-4f. The mean fiber and pore diameter were used as representative metrics for each image.
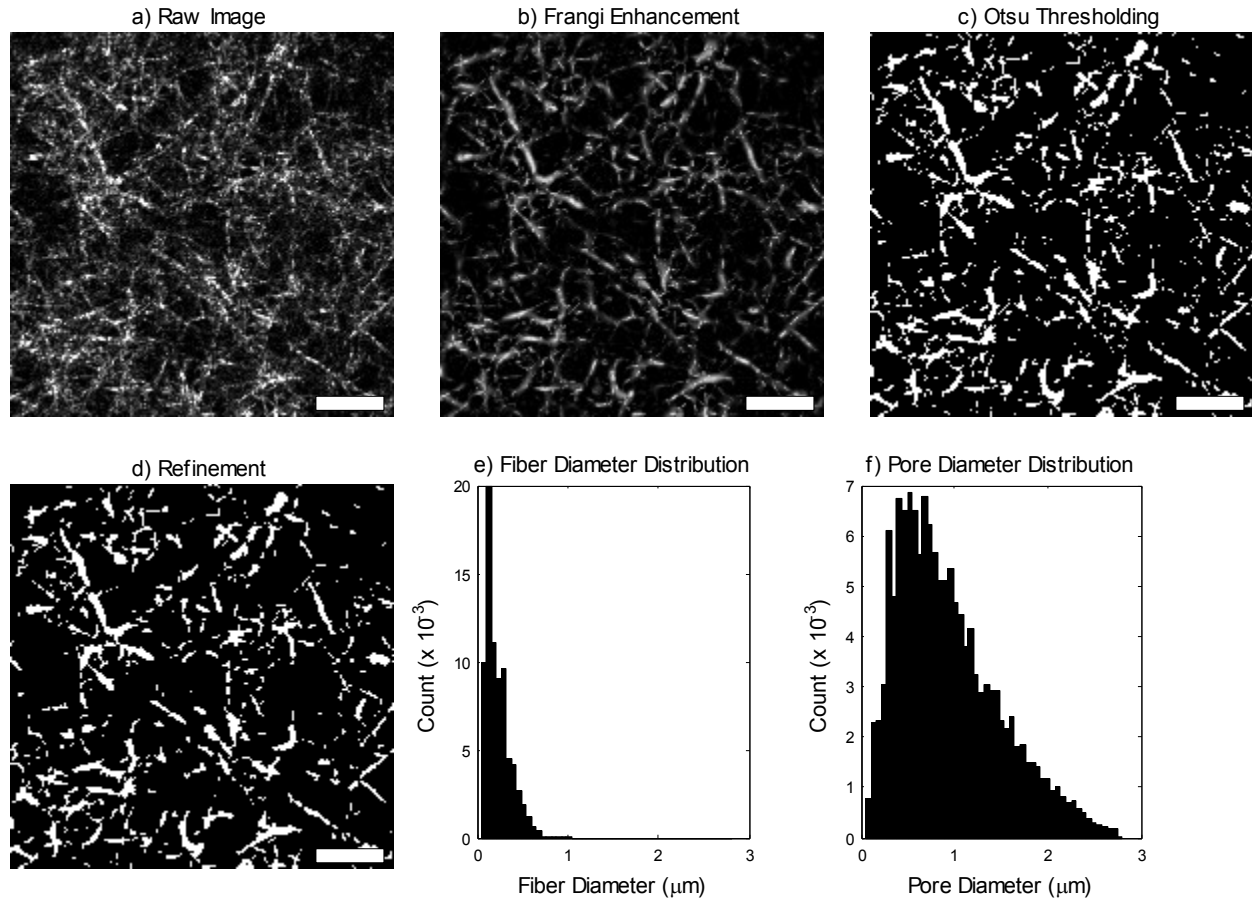
Figure 4-4: Implementation of fiber analysis.

Sample shown is a 1024x1024 pix subimage of a 4 mg/ml hydrogel polymerized at pH 7.4 and 37° C. Scale bar 10 μm.

4.3.7 Diffusivity Experimental Methodology

FRAP is a well-established technique in which a region of a sample containing fluorescent molecules is bleached using a laser-scanning confocal microscope; the subsequent exchange of bleached molecules with fluorescing molecules due to diffusion is imaged and used to calculate the rate of diffusion [8, 9, 33, 34]. Diffusivity measurements using FRAP were acquired at the same sample locations as fiber structure images. The confocal microscope was reconfigured for fluorescence imaging of the FITC-labeled dextran (488 nm beamsplitter/505 nm longpass) with the same 40X water immersion objective and pinhole of 1 Airy unit. The image size was set to 225 x 225 μm with a field of view of 512 x 512 pixels for a pixel resolution of 0.439 μm. Images were acquired every 1.5 s using bidirectional scanning to minimize acquisition time. Five pre-bleach images were acquired using 488nm Argon laser at 1% power in order to obtain a

background image. Subsequently, all available lasers and wavelengths (Argon 458/488/514 nm, HeNe 543 nm, HeNe 642 nm) were used at full power to bleach a horizontal region in the center of the sample with a height of 10 pixels and width of 768 pixels. The width of the bleach region was set to 150% of the image width in order to eliminate diffusion edge effect. After bleaching, 5 post-bleach images were recorded using the pre-bleach image settings. FRAP was performed at room temperature of $24 \pm 1°C$.

4.3.8 Diffusivity Analysis

Analysis of FRAP images to obtain diffusion rates was performed using the MATLAB-based algorithm developed by Seiffert and Oppermann [35]. Briefly, this algorithm fits a Gaussian distribution to the fluorescent intensity profile in each post-bleach image and estimates the diffusion rate from the decay of the Gaussian over time. Pre-bleach image subtraction was implemented to minimize the effect of background heterogeneity mentioned previously, while a high threshold of 0.8 was selected as the maximum acceptable change in Gaussian standard deviation between frames in order to capture the rapid diffusion of 1.5 nm (4 kDa) dextran. FRAP samples with an overall regression R^2 below 0.9 were discarded. In particular, the diffusion rate for the 1.5 nm dextran was near the limit of what could be captured with the confocal microscope used here, and a significant number of samples were discarded based on this criterion. Measurement of diffusion of smaller molecules would require either more powerful lasers or a spinning disk confocal.

4.3.9 Statistical Analysis

All statistical analysis was performed using JMP software (SAS). A two-way ANOVA was applied to data from each characterization method to identify statistically significant interactions. Tukey's HSD means comparison was used to determine the degree of significance (p-value) of interactions. In all subsequent figures, p-values are denoted with either asterisks (*) or pound symbols (#) as follows: * or #: significant at $p<0.05$, ** or ##: significant at $p<0.01$, *** or ###: significant at $p<0.001$, and **** or ####: significant at $p<0.0001$.

4.4   Results

4.4.1   Polymerization Kinetics

Regardless of fabrication conditions, polymerization of all samples followed the characteristic sigmoid function measured as early as 1960 for collagen fibril formation [36] (Figure 4-2). Early in the polymerization process, nucleation events begin to occur and absorbance increases slowly. The increase in absorbance accelerates as fibrils formed at nucleation sites assemble into fibers and the network develops, and finally slows to a saturation level at which no unpolymerized collagen remains. Figure 4-5 summarizes the mean and standard error (SE) of polymerization half time and lag time across the range of fabrication conditions in this study. All polymerization kinetics data, including polymerization rate and total change in absorbance, are tabulated in the Appendix (Section 0, Table 4-2) Figure 4-5 reveals the strength of correlation between temperature and time scales of polymerization (p-value of temperature means comparison indicated with # in Figure 4-5). Increasing collagen concentration contributes to more rapid initiation of polymerization (shorter lag times) as well as shorter half-times at room temperature (23°C); however, the effect of concentration on polymerization time scales becomes insignificant at the higher temperature (37°C). No significant relationships between pH and polymerization kinetics metrics were found (p>0.05) except for total change in absorbance (p<0.0001).
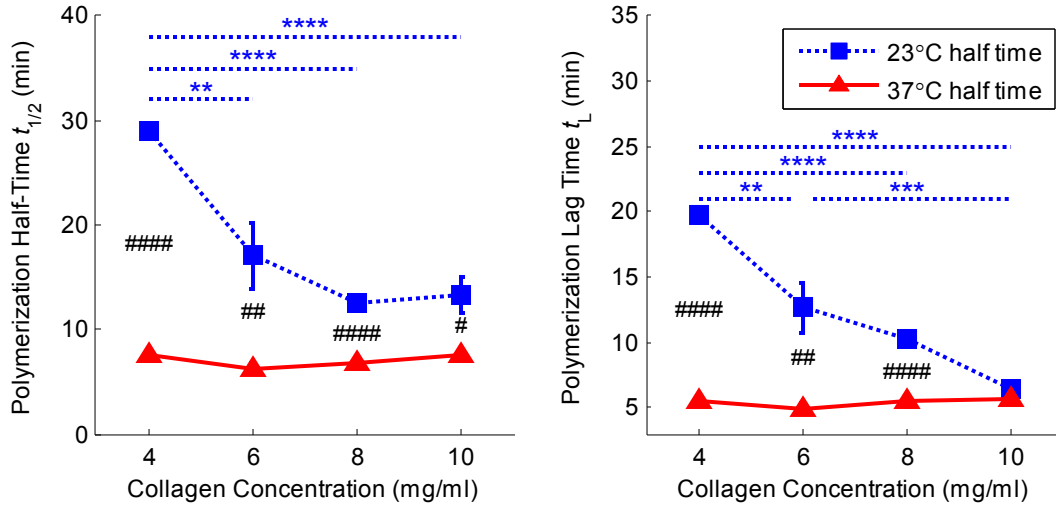
Figure 4-5: Kinetics of collagen hydrogel polymerization.

Blue square symbols with dashed lines represent hydrogels polymerized at 23°C while red triangle symbols with solid lines represent hydrogels polymerized at 37°C. As the effect of pH was statistically non-significant (p>0.05), data is averaged over all three pH groups. Data shown are mean + SE with N=6-12. Significance was calculated for pH-averaged groups: temperature means comparison is indicated with # while concentration means comparison is indicated with *. At 37°C (solid red lines), concentration had no significant effect on either polymerization half-time or polymerization lag time.

4.4.2 Compression Modulus

The slope measurements from all valid data sets for each fabrication condition were averaged to obtain the mean compression modulus, with a total of 4 to 16 valid runs for each fabrication condition. The results for all fabrication conditions are shown in Figure 4-6 and tabulated in the Appendix (Section 0, Table 4-3). Unlike polymerization kinetics, which was independent of pH and only dependent on concentration at low temperature, compression modulus was found to increase with all three fabrication parameters (pH means comparison and significance not shown).
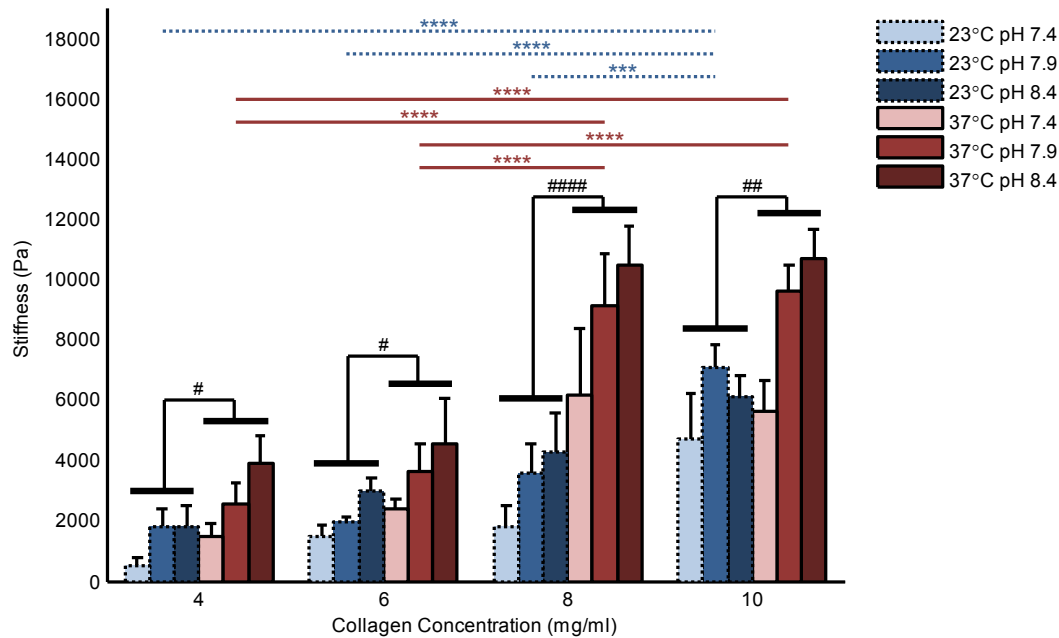
Figure 4-6: Compression modulus of collagen hydrogels at 0.1%/s deformation rate.
Blue bars with dashed lines represent hydrogels polymerized at 23°C while red bars with solid lines represent
hydrogels polymerized at 37°C. pH is indicated by color saturation. Data shown are mean + SE with N = 4-16
per bar. Significance was calculated for pH-averaged groups (N = 12-48) as indicated by horizontal black
bars. Temperature means comparison is indicated with # while hydrodynamic radius means comparison is
indicated with *.

4.4.3   Fiber Structure

Fiber images obtained using confocal reflectance microscopy were qualitatively similar to those
previously reported [28]. However, our images exhibited somewhat denser, less organized
networks because our hydrogels contained higher concentrations of collagen than those imaged
in previous studies. Hydrogels polymerized at low temperature exhibited more network-like
structures (Figure 4-7a-b), while those polymerized at high temperatures produced more
homogeneously distributed fibers with a smaller mesh size (Figure 4-7c-d). High-concentration
hydrogels polymerized at low temperature were often very heterogeneous despite careful sample
preparation and mixing (Figure 4-7b); this effect, although still present, decreased at high
temperature (Figure 4-7d). The wide distribution of pore and fiber diameter within a single
image can be seen in Figure 4-7e-f. Fibers in reflectance images often appear discontinuous

because some reflected light is blocked by near-field (out-of-plane) fibers and does not reach the sensor.
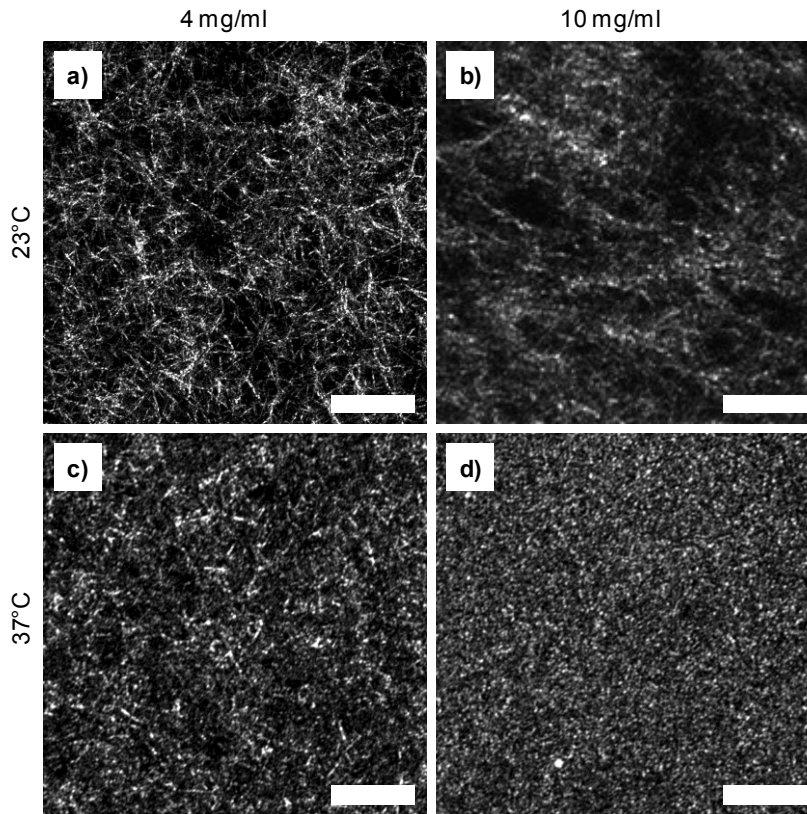
Figure 4-7: Fiber structure images obtained from confocal reflectance.
Images shown are for hydrogels polymerized at pH 7.4. Scale bar 25 μm.

The results of fiber structure image analysis for all fabrication conditions are shown in Figure 4-8 and tabulated in the Appendix (Section 0, Table 4-4). While pH and concentration had no significant impact on fiber structure, increasing temperature reduced both pore and fiber diameter significantly ($p<0.0001$). The mean pore diameter at 23°C was 2.54 ± 0.37 μm while the mean pore diameter at 37°C was 1.63 ± 0.23 μm. The temperature dependence of fiber diameter, although statistically significant, had a far smaller magnitude as the mean fiber diameter was 404 ± 26 nm at 23°C and 355 ± 12 nm at 37°C.
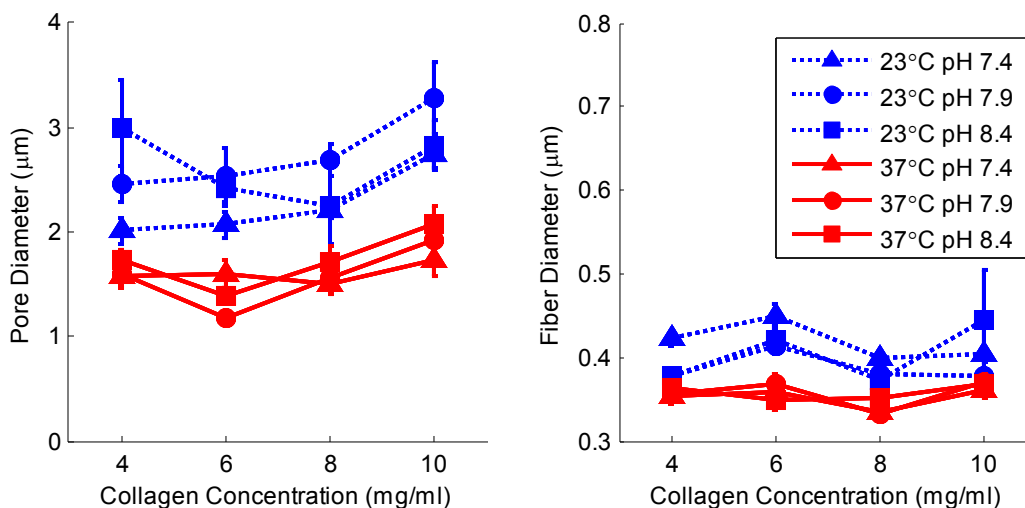
Figure 4-8: Pore and fiber diameter of collagen hydrogels.

Blue symbols with dashed lines represent hydrogels polymerized at 23°C while red symbols with solid lines represent hydrogels polymerized at 37°C. Data shown are mean + SE with N = 12. Significance was calculated for pH-averaged groups. At each concentration, the difference between means at T=23°C and T=37°C is significant at $p<0.0001$ for both pore diameter and fiber diameter.

4.4.4 Diffusivity

FRAP measurements were successfully obtained for all dextrans and fabrication conditions. Figure 4-9 shows a sequence of sample images from a FRAP data set. Many data sets (especially those with high MW dextran) contained some heterogeneity in the level of background fluorescence, including the sample shown in Figure 4-9. Diffusion occurred rapidly for all dextrans, as reflected in Figure 4-9 where high contrast is seen in the bleached region in the first post-bleach image, but little to no contrast remains in the image acquired 18 seconds post-bleach.
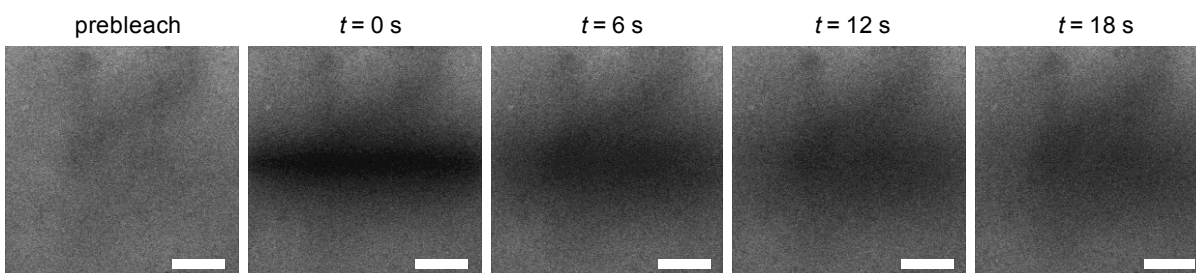
Figure 4-9: Representative FRAP image sequence.

Data shown is for 40 kDa dextran in 10 mg/ml collagen hydrogel polymerized at pH 7.4 and 23°C. Left to right: Prebleach; t = 0 s, t = 6 s, t = 12 s, t = 18 s. Scale bar 50 μm.

69

Figure 4-10 shows the dependence of diffusion rate on dextran size and polymerization temperature (tabulated data, including concentration and pH dependence, can be found in the Appendix (Section 0,Table 4-5)). The data are plotted as a function of the inverse of the Stokes (hydrodynamic) radius R_H of the dextrans considered rather than their molecular weight.
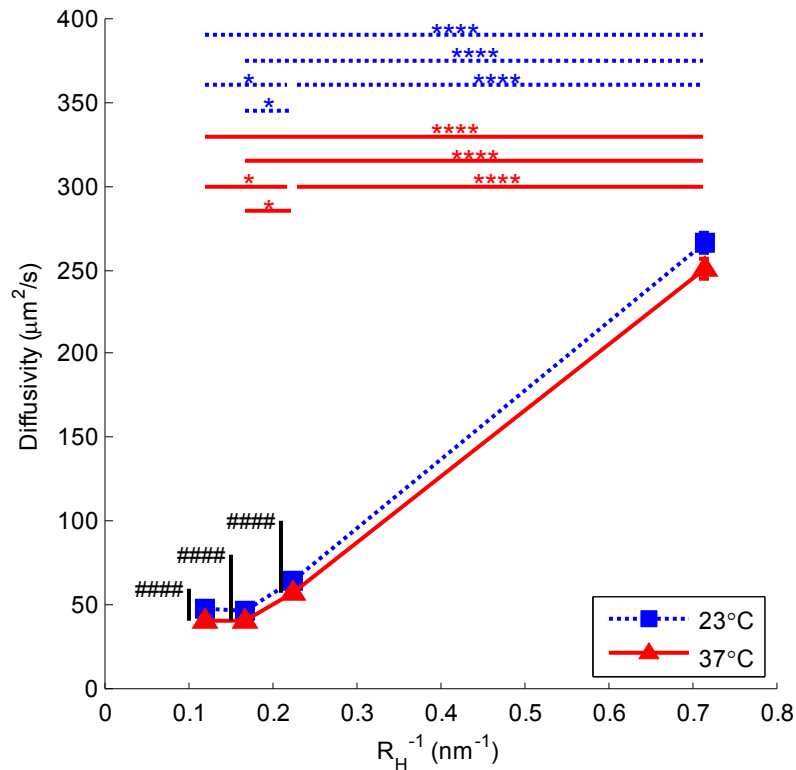
Figure 4-10: Rate of diffusion of dextran in collagen hydrogels.

Blue square symbols with dashed lines represent hydrogels polymerized at 23°C while red triangle symbols with solid lines represent hydrogels polymerized at 37°C. Data shown are mean + SE with N = 72. Each measurement is averaged over pH and concentration. Significance was calculated for pH- and concentration-averaged groups: temperature means comparison is indicated with # while hydrodynamic radius means comparison is indicated with *.

A nearly linear relationship between diffusivity and R_H^{-1} is revealed, similar to that predicted by the Stokes-Einstein relation for diffusion of spherical particles in a homogeneous fluid (Equation 4-2):

70

$$D = \frac{k_B T}{6\pi \eta R_H}$$

Equation 4-2

where k_B is Boltzmann's constant, T is temperature (K), and η is the kinematic viscosity of the fluid. Two-way ANOVA indicates relationships between diffusion rate and all fabrication parameters and inverse Stokes radius as well as second- and third-order interactions between control parameters. Although means comparisons confirms the significance of hydrogel fabrication parameters, their influence on the diffusivity was negligible compared with the influence of dextran size. Interestingly, the diffusivities of 70 and 150 kDa dextran were statistically indistinguishable at each temperature, despite the 40% difference in Stokes radius. Increasing polymerization temperature resulted in a decrease in diffusivity for all dextran sizes except 4 kDa. This data set had the largest uncertainty due to the measurement limitations of laser-scanning confocal microscopy for FRAP of high-diffusivity molecules, which has been previously noted [34, 35]. Increasing concentration also correlated significantly with decreased diffusivity (data not shown); the absolute effect was similar in magnitude to the effect of temperature and much less than the effect of molecule size.

4.5   Discussion

The results presented here demonstrate characterization of functional properties of collagen I hydrogels as well as polymerization kinetics over a range of collagen concentration, polymerization temperature, and polymerization pH. The following sections discuss in detail the correlations found between fabrication parameters and functional properties; furthermore, an empirical model predicting functional properties from fabrication parameters and a sensitivity analysis are presented.

4.5.1   Correlations between fabrication parameters and functional properties
Polymerization Kinetics

The time scales of polymerization, specifically half time and lag time, were inversely correlated with polymerization temperature and collagen concentration while the polymerization rate generally increased with temperature and concentration. This is in good agreement with previous studies [12, 13, 37, 38] as well as basic polymer chemistry and collision theory. At the higher

71

temperature (37°C), the correlation with concentration vanishes. This indicates that thermal energy is likely the rate-limiting factor at the low temperature condition, while a different factor (e.g. steric hindrance) becomes the rate-limiting factor at the higher temperature condition. Quantitatively, the measurements obtained in this study agree well with those previously published [12].

There is some disagreement in the literature with regards to the correlation between pH and polymerization kinetics [13, 36, 37]; however, differences in other fabrication parameters are likely the cause of discrepancies. Here we report no significant correlation of kinetic metrics with pH; however, this is unsurprising considering the limited range studied here (7.4-8.4). Although increased pH has been reported to correlate with decreased polymerization rate under fabrication conditions similar to those used here, this was for a large pH range (7-10) [13]; Over the pH range used in our study, no significant correlation has been previously demonstrated.

Stiffness

The positive correlation between hydrogel concentration and stiffness demonstrated here is well-known [12, 19, 38-40]. However, the relationship between polymerization temperature and compressive modulus has not been well characterized, and previous studies present contradictory findings [7]. The relationship seems to be dependent on pH and concentration ranges, and possibly deformation mode and rate as well. In this study, a significant positive correlation was found between temperature and compressive modulus. We hypothesize that, although no significant interaction between temperature and concentration was found within the ranges examined in this study, the effect of temperature may indeed be enhanced as concentration increases, and that the high absolute concentration studied here, relative to previous studies, enables the conclusive correlation of stiffness with temperature found here. The positive correlation of pH with stiffness found in the present study is supported by previous studies [13, 41] and likely due to the effect of stronger intermolecular forces as suggested by Rosenblatt et al. [42]. Despite the limited data available in the literature for confined compression of collagen hydrogels, which does not enable direct comparison due to differences in fabrication parameters as well as experimental parameters such as deformation rate, our numerical data are qualitatively in good agreement with previous studies [13, 15].

72

Fiber Structure

In this study, no correlation was found between collagen concentration and fiber diameter, a conclusion supported by previous studies [12, 39]. We measured a weak, but statistically significant (p = 0.032 at 23°C, p = 0.0035 at 37°C, pH-averaged), positive correlation between collagen concentration and pore diameter which contradicts previous studies [39, 43]; however, the absolute change in pore diameter was less than 0.5 μm over an increase of 6 mg/ml collagen content. Both decreased fiber diameter and decreased pore diameter were correlated with increased temperature due to faster precipitation and the presence of more nucleation sites, as demonstrated previously [11, 13, 23, 41]. Although previous studies identified a similar relationship with pH [10, 13, 28], no correlation was found with pH in this study, likely due to the limited range. Our results are in good agreement with previous studies, especially when sample shrinkage and resulting negative measurement bias is taken into consideration for data acquired using scanning electron microscopy (SEM) [11, 12, 39, 44].

Diffusion

The overall inverse relationship between diffusivity of dextrans in collagen hydrogels and their hydrodynamic radii matches that predicted by the Stokes-Einstein equation (Equation 4-2), although that equation is only strictly valid for spherical molecules diffusing in a homogeneous fluid. Surprisingly, the 150 kDa dextran did not continue this trend, but instead diffused at the same rate as the 70 kDa molecule. We note that an interaction between inverse hydrodynamic radius and pH was found by ANOVA to be significant for diffusion (p<0.0001), and hypothesize these may be related phenomena. Because intermolecular forces are strongly pH dependent and molecule shape depends on the balance of those forces, we hypothesize that the hydrodynamic radius of dextran also varies with pH and that the unexpectedly high diffusivity measured for 150 kDa dextran is in fact due to this deviation of R_H from the nominal value reported by the manufacturer (a measurement for which the pH was not specified). In support of this hypothesis, FRAP images with 150 kDa dextran in hydrogels polymerized at high pH (8.4) often contained small (several pixel) regions with high fluorescence intensity, indicating a degree of aggregation of the FITC-dextran (data not shown); this phenomenon only occurred for this particular combination of parameters.

73

The influence of hydrodynamic radius on diffusivity was far stronger than the influence of any hydrogel fabrication parameters, reinforcing previous observations that the hydrogel fiber structure does not significantly impede diffusion of particles with hydrodynamic radius (here: 1.4-8.5 nm) significantly smaller than the pore size of the network (here: 1.6-2.5 µm) [8, 34]. However, weak correlations were found between each parameter and diffusion rate. Increasing concentration resulted in reduced diffusivity, similarly to results published by Ramanujan et al. and Erikson et al., who examined concentration ranges of 0-45 mg/ml and 2-20 mg/ml, respectively [8, 9]. To our knowledge, the relationship between diffusivity and hydrogel polymerization temperature and pH has not been previously measured. Here, we report a small but statistically significant ($p = 0.002$) negative correlation between polymerization temperature and diffusivity. We also measure a positive but small relationship between pH and diffusivity. In fact, the effect of pH on diffusivity was ultimately most significant in the interaction with hydrodynamic radius.

4.5.2 Empirical linear regression for predictive modeling of hydrogel properties

The objective of this study was not only to elucidate the relationship between collagen material properties and a broad range of fabrication conditions, but also to generate a set of equations that can be used to optimize fabrication conditions to obtain a target functionality or *in vivo* tissue model. Multiple linear least squares regression was performed on the characterization data to obtain the following system of equations covering polymerization half-time (Equation 4-3) as well as functional properties compression modulus (Equation 4-4), pore diameter (Equation 4-5), and diffusivity (Equation 4-6). Regression equations for other parameters can be provided upon request.

$$
\begin{aligned}
t_{1/2} &= 21.89 \quad -13.69C' \quad -17.45T' \quad +13.77C' \cdot T' & \text{\textbf{Equation 4-3}} \\
E &= -853 \quad +5725C' \quad +2720T' \quad +2241pH' & \text{\textbf{Equation 4-4}} \\
\theta_P &= 2.236 \quad +0.369C' \quad -0.915T' \quad +0.245pH' & \text{\textbf{Equation 4-5}} \\
D &= 49.02 \quad -21.1C' \quad -0.33T' \quad -5.73pH' \quad +190.23(R_H^{-1})' \quad +0.37pH' \cdot (R_H^{-1})' & \text{\textbf{Equation 4-6}}
\end{aligned}
$$

where $t_{1/2}$ is in minutes, E is in Pa, $\emptyset_P$ is in µm, and D is in µm^2/s. C, T, pH, and R_H^{-1} have been transformed from the experimental domain to nondimensional parameters C', T', pH' and $(R_H^{-1})'$, each spanning a domain of 0-1 in order to enable comparison (Equation 4-7 - Equation 4-10):

$$C' \quad = \quad \frac{C - C_{MIN}}{C_{MAX} - C_{MIN}} \quad = \quad \frac{C - 4}{6} \qquad \text{Equation 4-7}$$

$$T' \quad = \quad \frac{T - T_{MIN}}{T_{MAX} - T_{MIN}} \quad = \quad \frac{T - 23}{14} \qquad \text{Equation 4-8}$$

$$pH' \quad = \quad \frac{pH - pH_{MIN}}{pH_{MAX} - pH_{MIN}} \quad = \quad pH - 7.4 \qquad \text{Equation 4-9}$$

$$(R_H^{-1})' \quad = \quad \frac{R_H^{-1} - \left(R_{H,MAX}\right)^{-1}}{\left(R_{H,MIN}\right)^{-1} - \left(R_{H,MAX}\right)^{-1}} \quad = \quad \frac{R_H^{-1} - 0.118}{0.597} \qquad \text{Equation 4-10}$$

where C is in mg/ml, T is in °C, pH is unitless, R_H is in nm, and *MIN* and *MAX* denote the extents of the experimental ranges (4-10 mg/ml, 23-37°C, 7.4-8.4, and 1.4-8.5, respectively). It should be noted that, if the equations are used as a predictive model to estimate the required fabrication condition to obtain desired properties, it remains strictly valid only within the experimental ranges, i.e. where the nondimensionalized fabrication parameters remain between 0 and 1. Values outside this range represent extrapolation of the data and should be used with caution.

Using the full set of raw data, higher-order optimization can be performed using functions available in statistical software. For example, the Prediction Profiler in JMP can be applied to the multivariate data set in conjunction with a set of desirability functions in order to find a fabrication condition which maximizes overall desirability. For the reader interested in performing such analysis, the raw data set can be provided upon request.

A sensitivity table demonstrating the relative influence of each fabrication parameter and interaction term on each functional property was derived from these equations (Table 4-1). By normalizing to the largest coefficient, the utility of each parameter for control of functional properties is elucidated. Here, the relationships examined in detail earlier in the discussion can be easily seen; for instance, the lack of correlation between polymerization half-time and pH contrasted with the strength of the interaction between concentration and temperature, which is comparable to the concentration term and nearly as great as the temperature term. This table is meant to be used as a quick guide for preliminary design of fabrication parameters for collagen hydrogels.

Table 4-1. Sensitivity of key hydrogel material properties to fabrication parameters. Sensitivities are obtained from the multiple regression coefficients, normalized to the largest coefficient in each model. The R^2 of the multivariate fit is indicated for each property. Analysis was performed on transformed (nondimensionalized) parameters. Only factors with $p<0.01$ (ANOVA) are shown.

Polymerization Half-Time ($R^2 = 0.565$)				Compression Modulus ($R^2 = 0.504$)				Pore Diameter ($R^2 = 0.332$)				Diffusivity ($R^2 = 0.867$)				
	C	T	pH		C	T	pH		C	T	pH		C	T	pH	r_H^{-1}
C	-0.78	0.79	-	C	1	-	-	C	0.40	-	-	C	-0.11	-	-	-
T	0.79	-1	-	T	-	0.48	-	T	-	-1	-	T	-	-0.002	-	-
pH	-	-	-	pH	-	-	0.39	pH	-	-	0.27	pH	-	-	-0.03	0.37
												r_H^{-1}	-	-	0.37	1

4.6 Implications for design of hydrogels

This work has quantitatively measured the sensitivity of a variety of collagen hydrogel functional properties, including stiffness, pore size, and diffusivity, to fabrication parameters varied within biological ranges. The characterization equations given here provide good coverage of functional properties within the domain; stiffnesses from 540 Pa to 10700 Pa and pore sizes from 1.2 to 3.2 µm can be obtained through optimization of all three parameters. While these ranges are not as large as those found *in vivo*, this represents the broadest range of functional properties demonstrated to be feasible for a single type of collagen hydrogel.

For the first time, we report here the sensitivity of hydrogel properties to multiple fabrication parameters. Although diffusivity depends most significantly on molecule size and is not strongly influenced by hydrogel preparation, the other properties measured here show significant correlation with multiple fabrication parameters. We expect that the results of this study will serve as an invaluable tool for tissue engineers across a range of applications, and hope that it will aid in standardization of hydrogel protocols between research groups.

4.7 Acknowledgements

4.8 Appendix: Characterization Data

Table 4-2: Polymerization kinetics (mean ± SE).

Concentration (mg/ml)	Polymerization Temperature (°C)	Polymerization pH	Polymerization Half-Time (min)	Polymerization Lag Time (min)	Polymerization Rate (min⁻¹)	Total Change in Absorbance
4	23	7.4	30.05 ± 1.86	19.78 ± 1.89	0.085 ± 0.008	1.75 ± 0.17
4	23	7.9	27.90 ± 0.43	19.17 ± 0.33	0.089 ± 0.002	1.56 ± 0.06
4	23	8.4	29.30 ± 1.32	20.53 ± 1.10	0.080 ± 0.001	1.40 ± 0.03
4	37	7.4	7.32 ± 0.06	5.13 ± 0.29	0.337 ± 0.006	1.47 ± 0.18
4	37	7.9	7.41 ± 0.18	5.42 ± 0.20	0.326 ± 0.003	1.30 ± 0.02
4	37	8.4	8.02 ± 0.65	5.82 ± 0.30	0.306 ± 0.038	1.32 ± 0.04
6	23	7.4	19.80 ± 6.93	14.23 ± 4.18	0.426 ± 0.167	2.97 ± 0.22
6	23	7.9	20.12 ± 6.04	14.41 ± 3.77	0.460 ± 0.197	2.54 ± 0.27
6	23	8.4	11.42 ± 1.46	9.43 ± 1.35	0.639 ± 0.071	2.48 ± 0.03
6	37	7.4	7.05 ± 0.37	5.49 ± 0.09	0.896 ± 0.391	2.44 ± 0.40
6	37	7.9	5.37 ± 1.05	4.23 ± 1.05	1.199 ± 0.107	2.71 ± 0.24
6	37	8.4	6.48 ± 0.74	5.24 ± 0.69	0.933 ± 0.062	2.31 ± 0.06
8	23	7.4	12.22 ± 0.22	9.32 ± 0.57	0.571 ± 0.064	3.16 ± 0.15
8	23	7.9	11.89 ± 1.06	10.52 ± 0.81	0.635 ± 0.076	2.83 ± 0.10
8	23	8.4	13.46 ± 0.99	11.09 ± 0.99	0.558 ± 0.054	2.60 ± 0.13
8	37	7.4	6.76 ± 0.21	5.58 ± 0.17	1.265 ± 0.150	2.98 ± 0.25
8	37	7.9	6.16 ± 0.85	4.86 ± 0.85	0.969 ± 0.019	2.51 ± 0.04
8	37	8.4	7.46 ± 0.46	5.94 ± 0.42	0.830 ± 0.037	2.51 ± 0.05
10	23	7.4	12.04 ± 2.61	7.95 ± 1.42	0.467 ± 0.099	3.02 ± 0.12
10	23	7.9	12.63 ± 2.91	5.91 ± 1.12	0.320 ± 0.114	2.78 ± 0.09
10	23	8.4	15.37 ± 3.93	5.26 ± 1.19	0.218 ± 0.085	2.51 ± 0.04
10	37	7.4	7.16 ± 1.08	5.45 ± 0.35	0.819 ± 0.365	2.25 ± 0.04
10	37	7.9	7.92 ± 0.38	5.94 ± 0.12	0.511 ± 0.037	2.00 ± 0.12
10	37	8.4	7.51 ± 0.53	5.58 ± 0.19	0.570 ± 0.146	2.10 ± 0.18

Table 4-3: Compression modulus (mean ± SE).

Concentration (mg/ml)	Polymerization Temperature (°C)	Polymerization pH	Compression Modulus (Pa)
4	23	7.4	538 ± 270
4	23	7.9	1794 ± 634
4	23	8.4	1834 ± 666
4	37	7.4	1473 ± 432
4	37	7.9	2576 ± 700
4	37	8.4	3933 ± 875
6	23	7.4	1501 ± 368
6	23	7.9	1954 ± 186
6	23	8.4	2991 ± 446
6	37	7.4	2399 ± 303
6	37	7.9	3641 ± 940
6	37	8.4	4578 ± 1498
8	23	7.4	1826 ± 700
8	23	7.9	3569 ± 985
8	23	8.4	4269 ± 1309
8	37	7.4	6158 ± 2256
8	37	7.9	9134 ± 1725
8	37	8.4	10517 ± 1298
10	23	7.4	4747 ± 1499
10	23	7.9	7088 ± 779
10	23	8.4	6111 ± 718
10	37	7.4	5655 ± 1001
10	37	7.9	9652 ± 846
10	37	8.4	10691 ± 1020

79

Table 4-4: Fiber structure metrics (mean ± SE).

Concentration (mg/ml)	Polymerization Temperature (°C)	Polymerization pH	Fiber Diameter (µm)	Pore Diameter (µm)
4	23	7.4	0.422 ± 0.009	2.01 ± 0.12
4	23	7.9	0.377 ± 0.006	2.46 ± 0.17
4	23	8.4	0.378 ± 0.006	2.99 ± 0.46
4	37	7.4	0.353 ± 0.008	1.57 ± 0.11
4	37	7.9	0.357 ± 0.005	1.59 ± 0.08
4	37	8.4	0.362 ± 0.004	1.73 ± 0.09
6	23	7.4	0.451 ± 0.013	2.07 ± 0.12
6	23	7.9	0.415 ± 0.012	2.54 ± 0.26
6	23	8.4	0.422 ± 0.010	2.43 ± 0.17
6	37	7.4	0.358 ± 0.007	1.59 ± 0.13
6	37	7.9	0.367 ± 0.012	1.17 ± 0.03
6	37	8.4	0.348 ± 0.010	1.38 ± 0.08
8	23	7.4	0.399 ± 0.007	2.22 ± 0.09
8	23	7.9	0.381 ± 0.006	2.69 ± 0.15
8	23	8.4	0.374 ± 0.008	2.25 ± 0.37
8	37	7.4	0.335 ± 0.004	1.49 ± 0.09
8	37	7.9	0.333 ± 0.004	1.56 ± 0.15
8	37	8.4	0.351 ± 0.008	1.71 ± 0.16
10	23	7.4	0.403 ± 0.008	2.75 ± 0.15
10	23	7.9	0.378 ± 0.002	3.28 ± 0.34
10	23	8.4	0.445 ± 0.608	2.83 ± 0.24
10	37	7.4	0.361 ± 0.008	1.73 ± 0.16
10	37	7.9	0.370 ± 0.009	1.92 ± 0.16
10	37	8.4	0.367 ± 0.007	2.07 ± 0.17

Table 4-5: Diffusivity (mean ± SE).

Dextran MW (kDa)	Stokes (Hydrodynamic) Radius (nm)	Concentration (mg/ml)	Polymerization Temperature (°C)	Polymerization pH	Diffusivity ($\mu m^2/s$)
4	1.4	4	23	7.4	220 ± 14
4	1.4	4	23	7.9	302 ± 19
4	1.4	4	23	8.4	387 ± 29
4	1.4	4	37	7.4	234 ± 21
4	1.4	4	37	7.9	277 ± 9
4	1.4	4	37	8.4	324 ± 14
4	1.4	6	23	7.4	202 ± 9
4	1.4	6	23	7.9	252 ± 8
4	1.4	6	23	8.4	225 ± 11
4	1.4	6	37	7.4	232 ± 7
4	1.4	6	37	7.9	233 ± 42
4	1.4	6	37	8.4	236 ± 19
4	1.4	8	23	7.4	255 ± 14
4	1.4	8	23	7.9	313 ± 19
4	1.4	8	23	8.4	262 ± 62
4	1.4	8	37	7.4	232 ± 15
4	1.4	8	37	7.9	293 ± 32
4	1.4	8	37	8.4	324 ± 33
4	1.4	10	23	7.4	233 ± 28
4	1.4	10	23	7.9	276 ± 31
4	1.4	10	23	8.4	267 ± 26
4	1.4	10	37	7.4	169 ± 9
4	1.4	10	37	7.9	185 ± 11
4	1.4	10	37	8.4	269 ± 43
40	4.5	4	23	7.4	69.2 ± 1.8
40	4.5	4	23	7.9	67.1 ± 2.3
40	4.5	4	23	8.4	72.2 ± 1.5
40	4.5	4	37	7.4	62.6 ± 3.1
40	4.5	4	37	7.9	61.1 ± 2.1
40	4.5	4	37	8.4	57.6 ± 0.7
40	4.5	6	23	7.4	71.4 ± 2.0
40	4.5	6	23	7.9	75.3 ± 1.1
40	4.5	6	23	8.4	77.8 ± 4.8
40	4.5	6	37	7.4	69.7 ± 2.4
40	4.5	6	37	7.9	62.5 ± 2.0
40	4.5	6	37	8.4	74.4 ± 3.2
40	4.5	8	23	7.4	59.2 ± 1.3
40	4.5	8	23	7.9	67.4 ± 2.5
40	4.5	8	23	8.4	63.4 ± 1.7
40	4.5	8	37	7.4	41.7 ± 1.6
40	4.5	8	37	7.9	50.2 ± 1.7
40	4.5	8	37	8.4	63.9 ± 3.0
40	4.5	10	23	7.4	55.7 ± 2.0
40	4.5	10	23	7.9	48.9 ± 1.3
40	4.5	10	23	8.4	51.0 ± 0.9
40	4.5	10	37	7.4	46.1 ± 2.5
40	4.5	10	37	7.9	44.3 ± 1.8
40	4.5	10	37	8.4	47.0 ± 1.1

81

Table 4-5 (continued): Diffusivity (mean ± SE).

Dextran MW (kDa)	Stokes (Hydrodynamic) Radius (nm)	Concentration (mg/ml)	Polymerization Temperature (°C)	Polymerization pH	Diffusivity (μm^2/s)
70	6.0	4	23	7.4	50.5 ± 1.6
70	6.0	4	23	7.9	57.4 ± 5.7
70	6.0	4	23	8.4	51.2 ± 4.0
70	6.0	4	37	7.4	50.7 ± 1.3
70	6.0	4	37	7.9	46.7 ± 1.4
70	6.0	4	37	8.4	50.8 ± 5.2
70	6.0	6	23	7.4	45.0 ± 0.4
70	6.0	6	23	7.9	49.1 ± 2.8
70	6.0	6	23	8.4	40.9 ± 0.6
70	6.0	6	37	7.4	45.6 ± 1.6
70	6.0	6	37	7.9	29.2 ± 0.3
70	6.0	6	37	8.4	41.9 ± 2.8
70	6.0	8	23	7.4	53.9 ± 1.4
70	6.0	8	23	7.9	55.5 ± 0.7
70	6.0	8	23	8.4	48.7 ± 1.3
70	6.0	8	37	7.4	38.4 ± 1.0
70	6.0	8	37	7.9	39.4 ± 2.6
70	6.0	8	37	8.4	50.4 ± 1.8
70	6.0	10	23	7.4	38.7 ± 2.0
70	6.0	10	23	7.9	35.9 ± 1.4
70	6.0	10	23	8.4	38.0 ± 1.5
70	6.0	10	37	7.4	30.6 ± 1.8
70	6.0	10	37	7.9	29.9 ± 0.7
70	6.0	10	37	8.4	29.5 ± 1.9
150	8.5	4	23	7.4	50.2 ± 2.3
150	8.5	4	23	7.9	51.9 ± 2.5
150	8.5	4	23	8.4	51.5 ± 2.7
150	8.5	4	37	7.4	59.0 ± 8.6
150	8.5	4	37	7.9	43.9 ± 2.3
150	8.5	4	37	8.4	42.1 ± 0.9
150	8.5	6	23	7.4	52.6 ± 2.1
150	8.5	6	23	7.9	56.4 ± 3.2
150	8.5	6	23	8.4	54.4 ± 2.4
150	8.5	6	37	7.4	48.9 ± 1.6
150	8.5	6	37	7.9	42.1 ± 1.3
150	8.5	6	37	8.4	42.2 ± 2.6
150	8.5	8	23	7.4	43.9 ± 2.5
150	8.5	8	23	7.9	49.3 ± 1.8
150	8.5	8	23	8.4	41.0 ± 1.4
150	8.5	8	37	7.4	41.9 ± 1.7
150	8.5	8	37	7.9	32.3 ± 3.1
150	8.5	8	37	8.4	39.7 ± 2.2
150	8.5	10	23	7.4	40.5 ± 2.7
150	8.5	10	23	7.9	38.0 ± 1.5
150	8.5	10	23	8.4	41.6 ± 3.8
150	8.5	10	37	7.4	32.1 ± 3.4
150	8.5	10	37	7.9	34.4 ± 1.6
150	8.5	10	37	8.4	29.6 ± 1.6

82

References

1. Tibbitt, M.W. and K.S. Anseth, *Hydrogels as extracellular matrix mimics for 3D cell culture.* Biotechnol Bioeng, 2009. **103**(4): p. 655-63.

2. Parenteau-Bareil, R., R. Gauvin, and F. Berthod, *Collagen-Based Biomaterials for Tissue Engineering Applications.* Materials, 2010. **3**(3): p. 1863-1887.

3. Ravi, S. and E.L. Chaikof, *Biomaterials for vascular tissue engineering.* Regenerative Medicine, 2010. **5**(1): p. 107-120.

4. Drury, J.L. and D.J. Mooney, *Hydrogels for tissue engineering: scaffold design variables and applications.* Biomaterials, 2003. **24**(24): p. 4337-51.

5. Gribova, V., T. Crouzier, and C. Picart, *A material's point of view on recent developments of polymeric biomaterials: control of mechanical and biochemical properties.* Journal of Materials Chemistry, 2011. **21**(38): p. 14354-14366.

6. Abraham, L.C., et al., *Guide to collagen characterization for biomaterial studies.* Journal of Biomedical Materials Research Part B-Applied Biomaterials, 2008. **87B**(1): p. 264-285.

7. Antoine, E.E., P.P. Vlachos, and M.N. Rylander, *Collagen I Hydrogels for Tissue Engineering: Characterization of Functional Material Properties.* Tissue Engineering Part B: Reviews, in review.

8. Ramanujan, S., et al., *Diffusion and convection in collagen gels: Implications for transport in the tumor interstitium.* Biophysical Journal, 2002. **83**(3): p. 1650-1660.

9. Erikson, A., et al., *Physical and chemical modifications of collagen gels: impact on diffusion.* Biopolymers, 2008. **89**(2): p. 135-43.

10. Raub, C.B., et al., *Image correlation spectroscopy of multiphoton images correlates with collagen mechanical properties.* Biophysical Journal, 2008. **94**(6): p. 2361-73.

11. Wolf, K., et al., *Collagen-based cell migration models in vitro and in vivo.* Semin Cell Dev Biol, 2009. **20**(8): p. 931-41.

12. Kreger, S.T., et al., *Polymerization and matrix physical properties as important design considerations for soluble collagen formulations.* Biopolymers, 2010. **93**(8): p. 690-707.

13. Achilli, M. and D. Mantovani, *Tailoring Mechanical Properties of Collagen-Based Scaffolds for Vascular Tissue Engineering: The Effects of pH, Temperature and Ionic Strength on Gelation.* Polymers, 2010. **2**(4): p. 664-680.

14. Wells, R.G., *The role of matrix stiffness in regulating cell behavior.* Hepatology, 2008. **47**(4): p. 1394-1400.

15. Yamamura, N., et al., *Effects of the mechanical properties of collagen gel on the in vitro formation of microvessel networks by endothelial cells.* Tissue Engineering, 2007. **13**(7): p. 1443-53.

16. Califano, J.P. and C.A. Reinhart-King, *Exogenous and endogenous force regulation of endothelial cell behavior.* Journal of Biomechanics, 2010. **43**(1): p. 79-86.

17. Lo, C.M., et al., *Cell movement is guided by the rigidity of the substrate.* Biophysical Journal, 2000. **79**(1): p. 144-152.

18. Haugh, M.G., et al., *Crosslinking and mechanical properties significantly influence cell attachment, proliferation, and migration within collagen glycosaminoglycan scaffolds.* Tissue Eng Part A, 2011. **17**(9-10): p. 1201-8.

19. Sieminski, A.L., R.P. Hebbel, and K.J. Gooch, *The relative magnitudes of endothelial force generation and matrix stiffness modulate capillary morphogenesis in vitro.* Exp Cell Res, 2004. **297**(2): p. 574-84.

20. Levental, I., P.C. Georges, and P.A. Janmey, *Soft biological materials and their impact on cell function.* Soft Matter, 2007. **3**(3): p. 299-306.

21. Gunzer, M., et al., *Migration of dendritic cells within 3-D collagen lattices is dependent on tissue origin, state of maturation, and matrix structure and is maintained by proinflammatory cytokines.* J Leukoc Biol, 2000. **67**(5): p. 622-9.

22. Carey, S.P., et al., *Biophysical control of invasive tumor cell behavior by extracellular matrix microarchitecture.* Biomaterials, 2012. **33**(16): p. 4157-65.

23. Yang, Y.L., S. Motte, and L.J. Kaufman, *Pore size variable type I collagen gels and their interaction with glioma cells.* Biomaterials, 2010. **31**(21): p. 5678-88.

24. Provenzano, P.P., et al., *Collagen density promotes mammary tumor initiation and progression.* Bmc Medicine, 2008. **6**.

25. Chrobak, K.M., D.R. Potter, and J. Tien, *Formation of perfused, functional microvascular tubes in vitro.* Microvascular Research, 2006. **71**(3): p. 185-196.

26. Cross, V.L., et al., *Dense type I collagen matrices that support cellular remodeling and microfabrication for studies of tumor angiogenesis and vasculogenesis in vitro.* Biomaterials, 2010. **31**(33): p. 8596-607.

27. Naciri, M., D. Kuystermans, and M. Al-Rubeai, *Monitoring pH and dissolved oxygen in mammalian cell culture using optical sensors.* Cytotechnology, 2008. **57**(3): p. 245-50.

28. Sung, K.E., et al., *Control of 3-dimensional collagen matrix polymerization for reproducible human mammary fibroblast cell culture in microfluidic devices.* Biomaterials, 2009. **30**(27): p. 4833-41.

29. Gelman, R.A., D.C. Poppke, and K.A. Piez, *Collagen fibril formation in vitro. The role of the nonhelical terminal regions.* J Biol Chem, 1979. **254**(22): p. 11741-5.

30. Frangi, A.F., et al., *Multiscale vessel enhancement filtering.* Medical Image Computing and Computer-Assisted Intervention - Miccai'98, 1998. **1496**: p. 130-137.

31. Kroon, D.-J. *Hessian based Frangi Vesselness filter*. 24409 2009; Available from: http://www.mathworks.com/matlabcentral/fileexchange/24409-hessian-based-frangi-vesselness-filter.

32. Garcia, D. *Image segmentation using Otsu thresholding*. 26532 2010; Available from: http://www.mathworks.com/matlabcentral/fileexchange/26532-image-segmentation-using-otsu-thresholding.

33. Leddy, H.A., M.A. Haider, and F. Guilak, *Diffusional anisotropy in collagenous tissues: fluorescence imaging of continuous point photobleaching.* Biophysical Journal, 2006. **91**(1): p. 311-6.

34. Gillette, B.M., et al., *Dynamic hydrogels: switching of 3D microenvironments using two-component naturally derived extracellular matrices.* Advanced Materials, 2010. **22**(6): p. 686-91.

35. Seiffert, S. and W. Oppermann, *Systematic evaluation of FRAP experiments performed in a confocal laser scanning microscope.* J Microsc, 2005. **220**(Pt 1): p. 20-30.

36. Wood, G.C. and M.K. Keech, *The formation of fibrils from collagen solutions. 1. The effect of experimental conditions: kinetic and electron-microscope studies.* Biochem J, 1960. **75**: p. 588-98.

37. Williams, B.R., et al., *Collagen fibril formation. Optimal in vitro conditions and preliminary kinetic results.* J Biol Chem, 1978. **253**(18): p. 6578-85.
38. Bailey, J.L., et al., *Collagen oligomers modulate physical and biological properties of three-dimensional self-assembled matrices.* Biopolymers, 2011. **95**(2): p. 77-93.
39. Miron-Mendoza, M., J. Seemann, and F. Grinnell, *The differential regulation of cell motile activity through matrix stiffness and porosity in three dimensional collagen matrices.* Biomaterials, 2010. **31**(25): p. 6425-35.
40. Roeder, B.A., K. Kokini, and S.L. Voytik-Harbin, *Fibril microstructure affects strain transmission within collagen extracellular matrices.* J Biomech Eng, 2009. **131**(3): p. 031004.
41. Raub, C.B., et al., *Noninvasive assessment of collagen gel microstructure and mechanics using multiphoton microscopy.* Biophysical Journal, 2007. **92**(6): p. 2212-22.
42. Rosenblatt, J., B. Devereux, and D.G. Wallace, *Injectable Collagen as a Ph-Sensitive Hydrogel.* Biomaterials, 1994. **15**(12): p. 985-995.
43. Gobeaux, F., et al., *Fibrillogenesis in dense collagen solutions: a physicochemical study.* J Mol Biol, 2008. **376**(5): p. 1509-22.
44. Brightman, A.O., et al., *Time-lapse confocal reflection microscopy of collagen fibrillogenesis and extracellular matrix assembly in vitro.* Biopolymers, 2000. **54**(3): p. 222-234.

5 Flow Measurements in a Blood-Perfused Collagen Vessel Using X-Ray Micro-Particle Image Velocimetry[*]

Elizabeth Antoine[1], Cara Buchanan[2], Kamel Fezzaa[3], Wah-Keat Lee[3],
M. Nichole Rylander[1,2], and Pavlos Vlachos[4]

[1]Department of Mechanical Engineering, Virginia Tech, Blacksburg, Virginia, USA

[2]VT-WFU School of Biomedical Engineering and Sciences, Virginia Tech, Blacksburg, Virginia, USA

[3]Advanced Photon Source, Argonne National Laboratory, Argonne, Illinois, USA

[4]School of Mechanical Engineering, Purdue University, West Lafayette, Indiana, USA

5.1 Abstract

Blood-perfused tissue models are joining the emerging field of tumor engineering because they provide new avenues for modulation of the tumor microenvironment and preclinical evaluation of the therapeutic potential of new treatments. The characterization of fluid flow parameters in such *in-vitro* perfused tissue models is a critical step towards better understanding and manipulating the tumor microenvironment. However, traditional optical flow measurement methods are inapplicable because of the opacity of blood and the thickness of the tissue sample. In order to overcome the limitations of optical method we demonstrate the feasibility of using phase-contrast x-ray imaging to perform microscale particle image velocimetry (PIV) measurements of flow in blood perfused hydrated tissue representative microvessels. However, phase contrast x-ray images significantly depart from the traditional PIV image paradigm, as they have high intensity background, very low signal-to-noise ratio, and volume integration effects. Hence, in order to achieve accurate measurements special attention must be paid to the image processing and PIV cross-correlation methodologies. Therefore we develop and demonstrate a methodology that incorporates image preprocessing as well as advanced PIV cross-correlation methods to result in measured velocities within experimental uncertainty.

5.2 Introduction

Three-dimensional (3D) engineered microfluidic tissue models have recently emerged as valuable tools for the study of the progression of disease such as cancers, the development of therapeutics under controlled conditions, and regenerative medicine [1-9]. Three-dimensional tissue models are not only superior to two-dimensional cultures that poorly reflect the pathological microenvironment, but are also inexpensive and easily controlled in comparison to animal models and clinical trials [3, 8-13]. Collagen I has become one of the most popular tissue models, as it forms the basis of natural extracellular matrix and can be easily formed into a 3D substrate for cell culture [14, 15]. Because fluid shear stress is known to play a pivotal role in several disease development processes such as tumor cell expansion, angiogenesis and metastasis [5, 16] as well as hemolysis and thrombosis formation [17], microfluidic vascular models are superior to static cultures. Characterization of the flow within perfused bioreactors in order to quantify fluid shear stress is critical towards understanding fluid-cell interactions [7, 18]. Particle image velocimetry (PIV) is a well-established noninvasive optical flow measurement technique that has been successfully used within various biological systems [19-21]. Our group has recently developed a novel *in-vitro* 3D perfused collagen-based tissue model for the study of cancer development and metastasis and successfully measured flow in this platform using microscopic PIV (μPIV); our initial studies have provided new insights into tumor-endothelial crosstalk under dynamic conditions [22].

A key challenge in tissue engineering is the transition from simple devices to more physiologically representative platforms. For example, vascular tumor models should be perfused with whole blood rather than cell culture media to better reproduce biological conditions of the *in-vivo* vasculature. However, because conventional PIV requires optical access to the region of interest, its use is limited to thin-walled transparent tissues perfused with a transparent fluid. Lima et al. have produced groundbreaking work in the development of μPIV techniques for blood flow measurement using a spinning-disk confocal PIV system [23-27]. Although their method has provided measurements at higher hematocrit and flow rates than were previously achieved, it is still restricted to measurement of flow in non-tissue transparent materials (PDMS or glass capillaries) with narrow channels (less than 100 μm along the optical axis) and sub-physiological flow rates (Re<0.025). Therefore the implementation of μPIV in

87

whole blood-perfused cellularized thick tissues necessitates the development of a new methodology for μPIV.

Phase-contrast x-ray PIV is a recently developed variation of standard optical PIV that permits measurement of flow within opaque vessels [28-31]. In contrast to other technologies for flow measurement in opaque systems, such as magnetic resonance imaging and nuclear imaging, x-ray PIV has high spatial and temporal resolution [32]. For conventional PIV measurements, tracer particles seeded within the flow of interest are illuminated by laser light and imaged with a high-speed camera. Subsequently, image pairs are correlated to calculate a velocity field with high spatio-temporal resolution [33, 34]. X-ray PIV replaces optical imaging with phase contrast imaging of x-ray-illuminated particles in the fluid volume. As such, the method is well-suited to characterization of *in vitro* and *in vivo* biological flows and a limited number of initial efforts have demonstrated PIV measurement in blood flows [35-38].

A significant limitation of phase-contrast x-ray imaging is that it provides extremely low signal to noise ratio (SNR) images that are generally inadequate for PIV cross-correlation. Several groups have developed complex techniques to improve the quality of x-ray PIV, including optimization of experimental conditions [38, 39], alternative image processing algorithms [40], and application of various correlation algorithms [37, 41]. However, the techniques previously published are application-specific. Furthermore, previous work in x-ray PIV has focused on thin-walled rigid vessel geometries as well as *in vivo* measurements in very small microvessels near the tissue surface [32, 36-38]. It is hypothesized that that quality of phase-contrast x-ray images obtained in thick-walled tissues or tissue models will be still further decreased and require additional consideration for PIV processing. To our knowledge, no data have yet been published demonstrating successful measurement of blood flow in a thick-walled perfused tissue representative such as collagen.

This work demonstrates the feasibility of accurate x-ray phase contrast PIV in a thick tissue model and contrasts with data acquired in thin-walled rigid vessels. Experimental data is acquired in a blood-perfused collagen hydrogel, and a methodology is presented for PIV analysis of the resulting low SNR images using advanced methods. These include image preprocessing for enhancement of the signal-to-noise ratio as well as the use and advanced phase correlation

approach to obtain more accurate velocity measurements. The following sections include descriptions of the experimental procedure used to obtain x-ray phase contrast images, discussion of advanced image processing and correlation techniques that are used to improve the PIV measurements, presentation of an optimal methodology, and evaluation of the results and performance of these methods.

5.3   Materials and Methods

5.3.1   Microvasculature models

Three sets of experimental conditions with varying experimental complexity were considered. The most basic condition was a rigid polymer polytetrafluoroethylene (PTFE) channel (756 μm diameter) perfused with a glycerine solution. The second channel (867 μm diameter) was rigid fluorinated ethylene propylene (FEP) perfused with whole bovine blood. Finally, the most complex experiment used a collagen I vessel bioreactor (742 μm diameter) perfused with whole bovine blood. PTFE and FEP are similar semi-rigid polymers that are non-reactive with blood, and tubing made of these materials is readily available with dimensions similar to microvasculature. Collagen I was selected for this experiment because it comprises the majority of tissue extracellular matrix, can be easily extracted from rat tail tendon, and is widely used as a matrix substrate for in vitro engineered tissues [42]. The collagen hydrogel provides mechanical and chemical stability while supporting cellular growth, organization, and structural remodeling similar to that found in vivo [14, 15].

The collagen vessel was fabricated as described previously [22]: type I collagen stock solution was prepared from rat tail tendons dissolved in pH-2.0 HCl and combined with 10X Dulbecco's Modified Eagle Medium (DMEM), 1N NaOH and deionized water to prepare a solution with 10 mg/mL collagen. The collagen solution was injected into a 5 cm long, 3 mm diameter cylindrical FEP shell fitted concentrically with a 5 cm long 22 gauge (711 μm) stainless steel needle and sealed at the ends with acrylic sleeves. The solution was cured for 30 minutes at 37°C, after which a cylindrical microchannel was created in the collagen hydrogel by removal of the needle. 1.27 cm long stainless steel needles were inserted into the acrylic sleeves at the ends of the collagen vessel to provide luer interfaces for connection with the flow system. Figure 5-1 depicts the collagen microchannel (not to scale). The PTFE and FEP channels were perfused with the

same flow system using identical needles inserted into the ends of 5 cm sections of tubing and sealed with silicon adhesive.
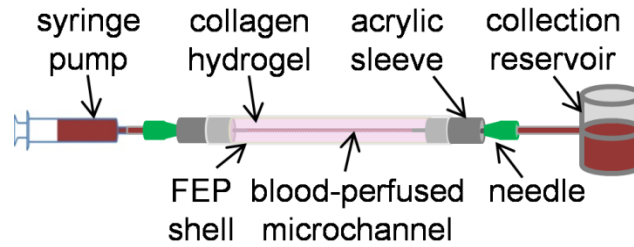

Figure 5-1: Diagram of blood-perfused collagen vessel bioreactor.

5.3.2   Working fluids and flow condition

Two working solutions were used for these experiments. A 50% v/v solution of water and glycerine was perfused in the PTFE channel. This solution was chosen because it closely matches the viscosity and density of blood and could therefore be perfused at the same rate as blood to achieve the same Reynolds number for flow similarity. The matched density also permitted the same neutrally buoyant tracer particles to be used in both blood and the glycerine solution. Fresh whole bovine blood (Bovine Blood in Citrate Anticoagulant, Quad Five) was perfused in both the FEP and collagen channels. The difference in source species between hydrogel and fluid (rat vs. bovine) is not expected to significantly affect the results as the hydrogel is formed after denaturation and reconstitution of tendon. Experiments were performed within 48 hours of the time that blood was drawn, and all procedures involving blood were performed under sterile conditions and using equipment washed with phosphate buffer solution (PBS). Blood was kept refrigerated until shortly before experiments were performed, at which time it was heated to room temperature (22 C). The dynamic viscosity of whole blood was measured to be 8.15 cP $\pm$ 5% and the viscosity of the 50% v/v water/glycerine solution was measured to be 9.5 cP $\pm$ 5%. Measurements were taken at 22°C and a shear rate of 30 s^{-1} using a Brookfield DVII+ Pro cone-plate viscometer. Because bovine red blood cells (RBCs) do not form rouleaux as do human RBCs [43], and the addition of citrate anticoagulant further reduces the shear dependence of viscosity, blood viscosity was assumed to be shear-independent in this study. The density of whole blood (1.06 g/cm^3) [44] is nearly that of water, while that of a 50% v/v water/glycerine solution at 22°C is slightly higher at 1.14 g/cm^3 [45].

90

The fluids were seeded with ~4% v/v neutrally buoyant hollow glass microspheres (Sphericel, Potters Industries) with 10 μm nominal diameter. Hollow glass particles were selected because the density interface between air and glass creates high contrast for x-ray imaging; furthermore, they are suitable flow tracers as they are neutrally buoyant at a diameter of 10 μm. Because the negative surface charge acquired by glass immersed in water can activate the platelets in whole blood and initiate coagulation, it was necessary to first treat the glass microspheres with blood plasma to provide a protective protein coating on the glass surfaces before making a suspension of whole blood and particles. Whole bovine blood was centrifuged and the plasma supernatant was extracted. 220 mg of dry neutrally buoyant particles were suspended in 1 mL of plasma and incubated for 24 hours at 37° C. Finally, 5 mL whole blood was added to the plasma solution for the final working solution: blood seeded with 37 mg/mL neutrally buoyant hollow glass microspheres. For the water/glycerine working fluid, the highly concentrated filtered particle solution was diluted with distilled water to approximately twice the concentration of the whole blood solution and mixed with an equal volume of glycerine to obtain the second final working solution: 50% v/v water/glycerine seeded with approximately 40 mg/mL neutrally buoyant hollow glass microspheres.

Flow was generated using a syringe pump (Harvard Apparatus, PhD). Prior to flow measurements, the vessel was primed with the working fluid and flushed for several seconds at 5mL/min to clear adhered and aggregated particles from the vessel. During flow measurements, the fluid was perfused steadily through the vessel at a flow rate Q = 5 μL/min for a theoretical peak velocity of 0.3-0.4 mm/s depending on vessel diameter. The Reynolds number was approximately 0.03 for all experimental cases.

5.3.3 Phase-contrast X-Ray Imaging

X-ray particle images were acquired at the X-ray Science Division beamline 32-ID of the Advanced Photon Source (APS) at Argonne National Laboratory. For each experiment, the vessel (PTFE, FEP, or collagen microvessel) was fixed in the path of a monochromatic x-ray beam with 1 mm^2 cross-sectional area. The x-ray source was the standard APS undulator A, set to 15.5 mm gap. The energy of the beam, controlled by a cryogenically cooled double crystal monochromator (DCM) (Si 1 1 1) with energy band pass dE/E~10^{-4}, was 18 keV. The beam was converted into visible light by a 100 μm thick YAG:Ce scintillator crystal and magnified with a

5x lens (LWD objective, Mitutoyo) for imaging (Figure 5-2). 1.2 megapixel 8-bit images were recorded at f = 20 or 30 Hz (depending on the experimental case) with a machine-vision camera (AVT Pike F-505B). Images of a 400-mesh gold transmission electron microscopy (TEM) reference grid were recorded and used to measure the effective pixel size of 1.32 μm/pixel. A minimum of 2000 images was collected for each experimental case.
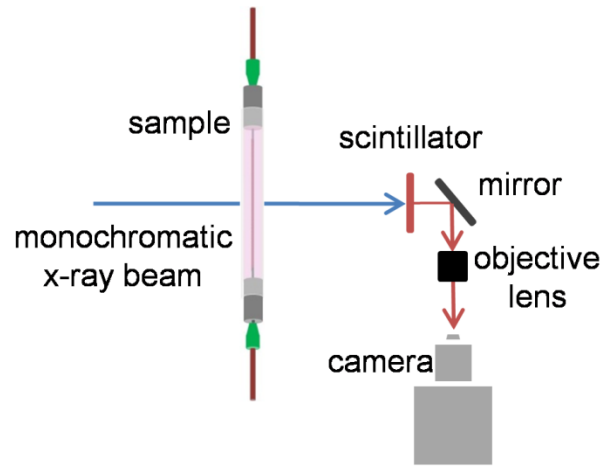

Figure 5-2: Schematic of x-ray PIV in collagen vessel bioreactor.

5.4   Results

5.4.1   Effect of Image Preprocessing on Image Signal-to-Noise Ratio and PIV Accuracy

While fluorescent particles used in optical μPIV are excited by and emit high intensity light, in phase-contrast x-ray imaging intensity variations are generated due to material density differences that result in changes in the index of refraction for propagating monochromatic x-ray beams. Particle images in optical PIV ideally have a Gaussian intensity distribution, while particle information in x-ray phase contrast images is manifested by interference patterns in the intensity distribution, such as a bright center and dark circumference for a hollow glass sphere [46]. Furthermore, phase-contrast x-ray images can exhibit high and non-uniform background intensity due to artifacts in the incident beam and image formation process, and experimental conditions can lead to the presence of particle aggregation and further artifacts, as shown by a representative image in Figure 3A. Hence, image pre-processing is essential.

Typical image processing involves background removal using subtraction of the mean image generated by averaging across the whole dataset [47]. For the data presented here, this procedure

92

was modified and a temporal mean background subtraction [48] with a window of 10 images was performed. In temporal mean background subtraction, at each time point the mean image subtracted from the current frame is computed as the average of frames in a temporal window centered on the current frame. This processing technique was used to overcome particle aggregation effects: despite the plasma treatment, glass flow tracers form aggregates that roll slowly along the walls of the channel, not following the flow and biasing the velocity measurements. The particle aggregates move sufficiently during recording of a data set (>2000 frames) that they do not contribute to the mean of the entire data set and are retained in traditional background subtraction; however, they remain stationary in a 10-image mean and can thus be effectively removed. In contrast, flow-tracing particles, even those near the vessel walls, move sufficiently during the 10-frame window that they are retained after background subtraction and their signal is not lost.

Subsequently, a high-pass frequency-domain Gaussian filter was selected to equalize illumination across the image, revealing intensity fluctuations due to the flow tracers or other density variations. Finally, the process of manufacturing the collagen microchannels produces unavoidable micro-bubbles in the hydrogel. Given the high density difference between the collagen and the micro-bubbles and the volume integration nature of x-ray image recording, such artifacts can completely obscure the flow. This was addressed by applying a binary mask to the image so that correlations would not be performed in the regions where the image is known to have no meaningful information. Here, the mask was manually drawn over collagen inclusions based on visual inspection of the raw images.
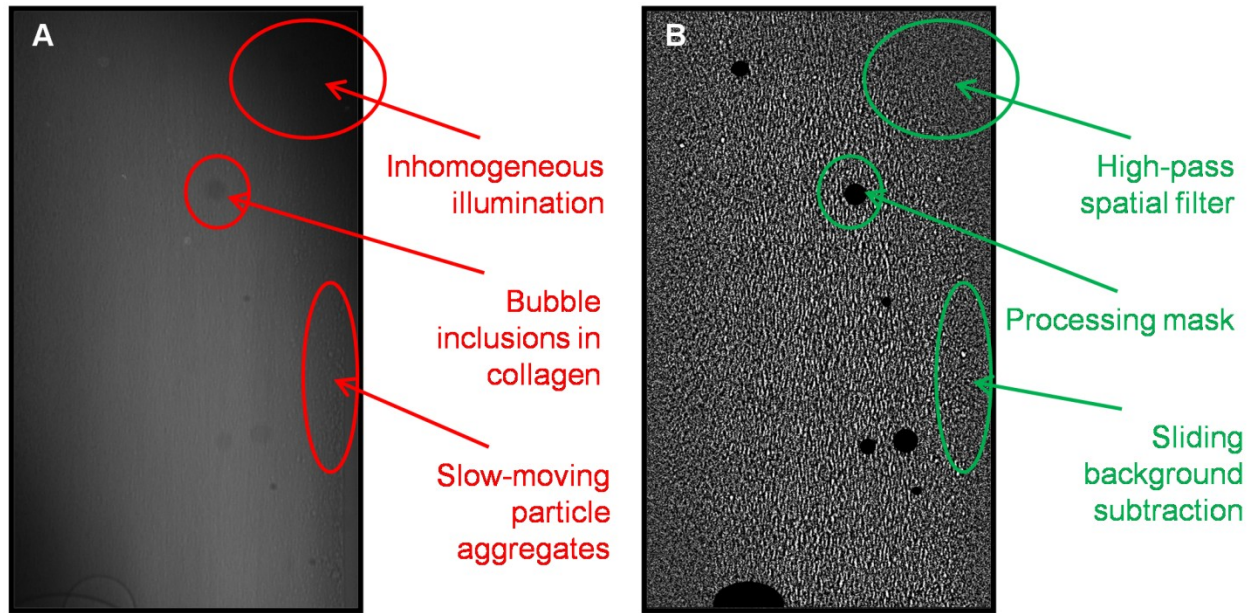
Figure 5-3: Sample images of blood flow in the collagen microchannel.
A: Raw image after reorientation and cropping to vessel diameter. B: Processed image (sliding mean background subtraction, high-pass filter, and mask). Image B has been brightness- and contrast-enhanced for visualization.

The effect of image processing is shown in Figure 5-3B. In comparison with the raw image in Figure 5-3A, individual particles can be visually identified in the processed image and, although contrast enhancement is necessary for visualization for Figure 5-3B, it is clear that the contrast between particles and background is significantly higher. Furthermore, near-wall particle aggregates have been effectively removed and low-frequency intensity variation across the image has been successfully eliminated. Masked regions are shown in solid black in Figure 5-3B. From Figure 5-3B however, it is evident that the resulting images are more representative of a speckle pattern. Furthermore, the particles exhibit a degree of longitudinal "smearing" due to their displacement during the camera exposure. The images therefore do not resemble conventional PIV images.

To determine the effect of image processing on velocity field accuracy, PIV was performed on both raw and processed images. Correlation windows of 4x64 pixels with 75% overlap were selected to satisfy the optimization conditions published in [49] for the case of uniaxial high-shear flow. Single-pass standard cross-correlation (SCC) with zero-mean windows and three-point Gaussian (3PG) peak detection was applied and correlations were validated using a median

94

universal outlier detection (UOD) scheme [50] with a 9x9 stencil and velocity thresholding. Secondary peaks were interrogated as potential replacements for invalid vectors. Instantaneous vector fields were averaged in time for post-processing; the results are shown in Figure 5-4. The volume-adjusted velocity profile used as a reference for comparison with the volumetric PIV data is computed by integration of the axisymmetric Poiseuille solution along the x-ray beam path through the channel. This results in a parabolic profile with two-thirds the magnitude of the centerline velocity profile [31]. For all three experimental cases, the unprocessed images result in severe underestimation of the velocity field, with root-mean-square (RMS) deviation of the velocity profile from the true value near 60% for all cases. Image processing significantly increases the accuracy of the velocity field, resulting in vector fields with only 10-30% RMS deviation from the true value. Although this error is still significant and further improvement of data processing is necessary, this result demonstrates that basic image processing alone can reduce the error in mean PIV velocity fields by over 50%.
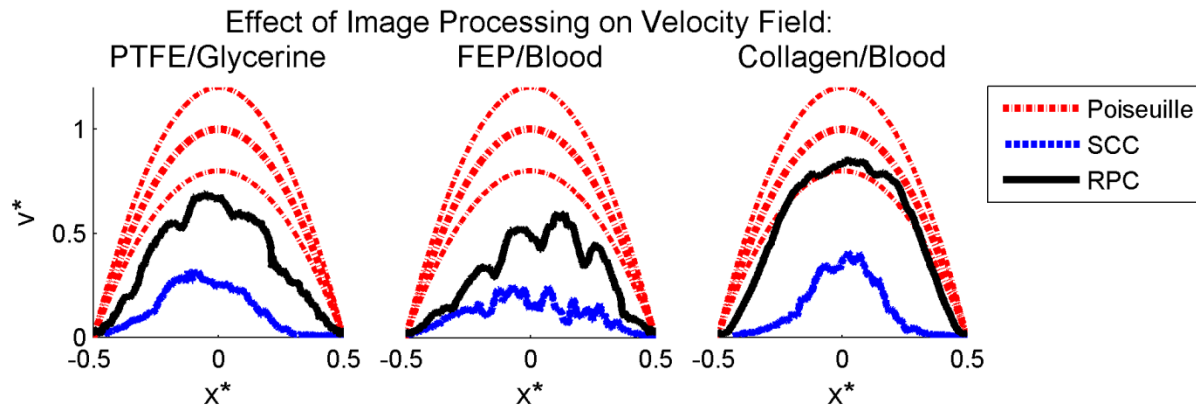

Figure 5-4: Effect of image preprocessing on PIV accuracy.
Mean velocity profiles obtained using standard PIV correlation applied to raw images (dashed blue lines) and processed images (solid black lines) are plotted with the volume-adjusted Poiseuille solution (dashed red lines) for each experimental case. The uncertainty based on measured flow rate and vessel diameter is plotted for the theoretical solution (upper and lower dashed red lines). The 95% confidence interval on the mean for the experimental data is not distinguishable from the mean. Left to right: glycerine-perfused PTFE, blood-perfused FEP, and blood-perfused collagen. Data shown is averaged in time and along the length of the vessel and is normalized for each experimental case by the vessel diameter and theoretical maximum velocity.

The improvement in correlation accuracy after image processing is expected to be due to removal of the non-moving background and artifacts, or "noise", which were correlating far more strongly than the weak signal provided by the particles. Removal of this background, artifacts, and error-generating intensity fluctuations should have increased the signal-to-noise ratio, resulting in correlation peaks closer to the true particle displacement. To determine quantitatively the effect of image processing, the SNR of each image set was examined before and after image processing.

In microPIV applications, SNR has previously been calculated as the ratio of the peak intensity of a typical particle to the mean background intensity [51]. This definition not only assumes that the particle images have a Gaussian distribution, but also requires that individual particles be readily identified. Neither of these conditions is met by x-ray phase contrast images, requiring the use of an alternative definition of SNR. Here we calculate SNR using the peak-to-root mean square ratio (PRMSR) as described by Kumar et al. [52], where the signal component is represented by the magnitude of the image autocorrelation peak y_0 and noise component is the RMS of values outside the correlation peak y_{RMS} (Equation 5-1). Here, following Kumar et al., the threshold to separate the peak from the noise is chosen to be 50% of the peak magnitude. This SNR provides an estimate of image quality with no dependence on external experimental parameters or assumptions about image properties.

$$PRMSR = \left(\frac{y_0}{y_{RMS}} \right)^2$$

Equation 5-1

The PRMSR was calculated for 32x32 pixel blocks of each image and the median value of all blocks was taken as the SNR of each image. Finally, the SNR of each experimental case was computed as the mean SNR of all images in the data set, for both the raw and processed images. The results, shown in Figure 5-5, confirm the hypothesis that the image processing significantly improved image quality: the SNR for the processed images is at least 7 dB higher than the SNR for the raw images. This higher SNR for the processed images corresponds to the improved accuracy of the corresponding velocity fields in Figure 5-3, indicating that this definition of SNR

can be a good predictor of relative correlation accuracy even though it contains only single-image intensity information.
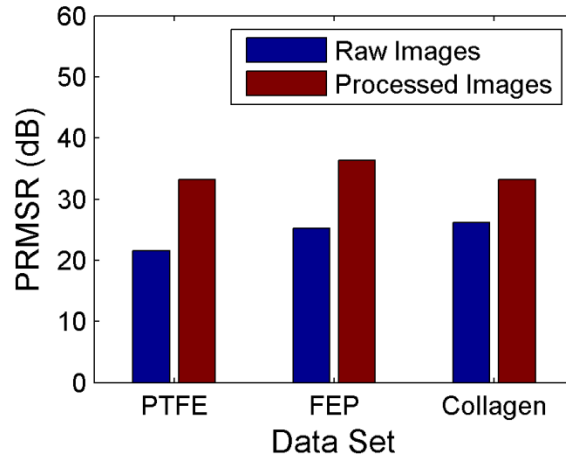

Figure 5-5: Comparison of image signal-to-noise ratio before and after image preprocessing. The mean SNR of all images (>2000) is plotted for each data set.

5.4.2 Effect of Robust Phase Correlation on PIV Accuracy

The benefit of image processing to improve SNR for low-quality images has been established; however, even improved images give inaccurate results using SCC. This is because the images still contain significant noise levels, and the correlation peaks are too broad for accurate peak detection. Eckstein et al. developed an advanced correlation technique known as robust phase correlation (RPC) which applies an SNR filter to the image cross-correlation [53, 54]. The SNR filter is a spectral filter weighted based on a theoretical SNR, which assumes that the signal is composed of Gaussian particles with a specified input diameter, here defined as 2.8 pixels. Typically RPC provides a sharper peak with better peak detectability than SCC and results in higher accuracy for velocity measurements.

PIV correlations are typically performed in the Fourier domain to improve computational efficiency; however, the application of Fourier transforms to discrete data introduces error. A 50% Gaussian windowing filter, which has been shown by Eckstein et al. to increase measurement resolution and accuracy by minimizing this error [55], was applied in the Fourier domain to 8x128 pixel regions to obtain post-filter correlation windows of 4x64 pixels, the same dimensions as used for SCC processing. Single-pass RPC with 2.8 pixel particle diameter was applied using the same zero-mean windows, 3PG peak detection, and validation scheme as used

97

for SCC processing, and the resulting vector fields were subsequently time-averaged. Figure 5-6 shows both the original SCC and the new RPC velocity profiles. For all three experimental cases, the application of RPC and the windowing filter has a smoothing effect on the velocity profile but has little effect on the magnitude of the velocity profile. In fact, for the case of blood-perfused collagen the addition of RPC and windowing negatively biased the resulting velocity field.
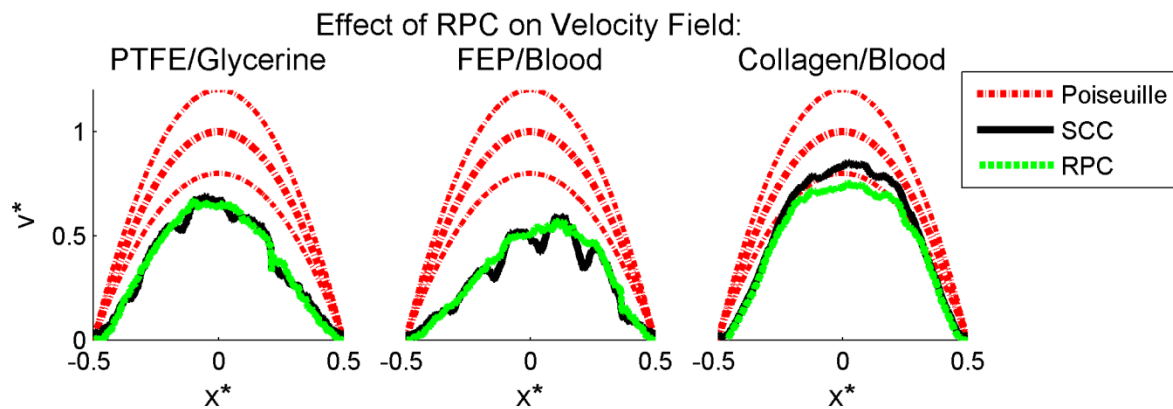

Figure 5-6: Effect of PIV correlation method on PIV accuracy.
Mean velocity profiles obtained using standard cross-correlation (solid black lines) and robust phase correlation with 2.8 pixel diameter (dashed green lines) applied to processed images are plotted with the volume-adjusted Poiseuille solution (dashed red lines) for each experimental case. The uncertainty based on measured flow rate and vessel diameter is plotted for the theoretical solution (upper and lower dashed red lines). The 95% confidence interval on the mean for the experimental data is not distinguishable from the mean. Left to right: glycerine-perfused PTFE, blood-perfused FEP, and blood-perfused collagen. Data shown is averaged in time and along the length of the vessel and is normalized for each experimental case by the vessel diameter and theoretical maximum velocity.

To examine the effect of RPC on correlation accuracy, SCC and RPC correlation planes from a representative correlation region positioned midway between the centerline and wall were plotted for each experimental case (Figure 5-7). Although RPC provides sharper peaks in the correlation plane, multiple peaks of similar magnitude can still be present. This indicates that while subpixel accuracy is improved for RPC over SCC, the peak corresponding to the correct displacement may not be accurately determined.
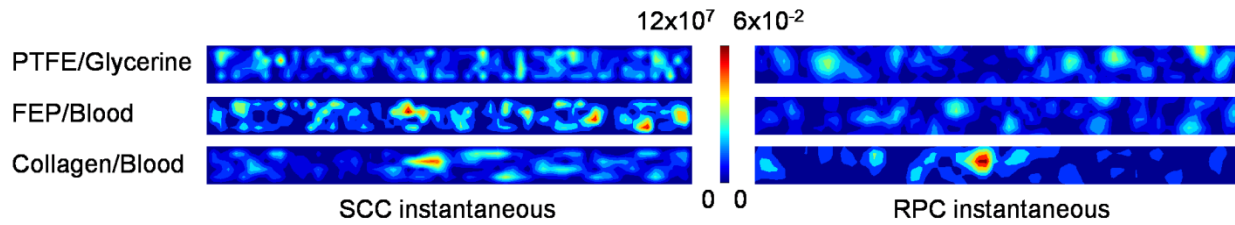
98

Figure 5-7: Contours of SCC and RPC correlation planes.
The contour indicates relative correlation magnitude. Only the central 50% window is shown for RPC correlation planes.

5.4.3 Sum-of-Correlation for Improved Correlation Accuracy

As demonstrated in the previous section, even with the use of RPC, multiple peaks remain in the correlation planes, leading to invalid vector detection and contaminating the mean velocity profiles. Sum-of-correlation, also known as ensemble correlation, is a technique which can be applied to steady or periodic flows and is performed by averaging instantaneous correlation functions prior to peak detection rather than after estimation of velocity fields [56, 57]. This technique increases correlation accuracy and resolution by effectively increasing the signal in each correlation, and has been used to enable accurate measurements in flows with low seeding and/or low SNR. Because of this, sum-of-correlation is ideally suited to this experimental data.

Image pairs were correlated using a single-pass RPC sum-of-correlation algorithm. All other parameters were identical to the previous processing algorithm, including 50% Gaussian windowing, window dimensions, RPC diameter, zero-mean windows and 3PG peak detection. Validation was again performed using a 9x9 UOD scheme and thresholding with secondary peak replacement. Because sum-of-correlation uses the temporal component of the data in the correlation, a single vector field resulted, which was subsequently averaged along the length of the vessel. Figure 5-8 compares instantaneous and sum-of-correlation velocity profiles. For all three experimental cases, sum-of-correlation increases the magnitude of the velocity profile, increasing its accuracy.
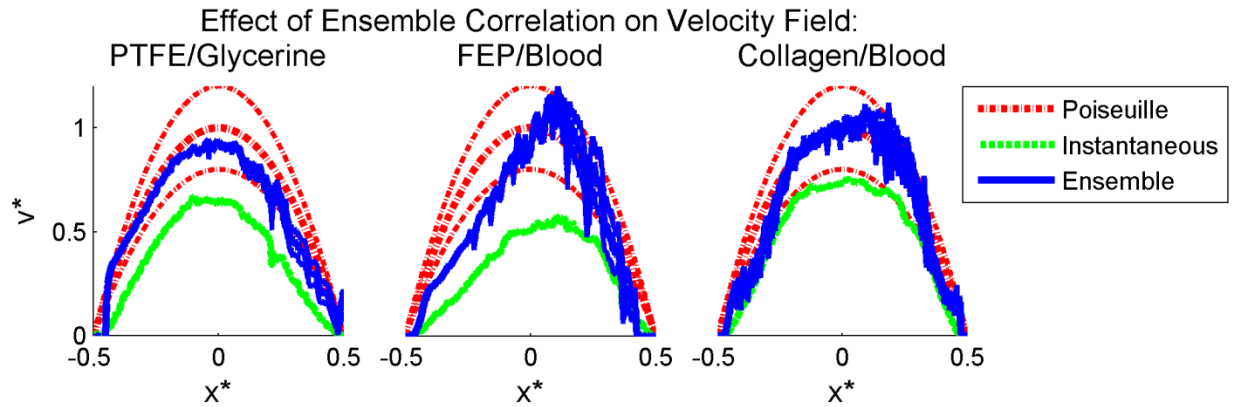
99

Figure 5-8: Effect of sum-of-correlation on PIV accuracy.

Mean velocity profiles obtained using instantaneous (dashed green lines) and sum-of-correlation (solid blue lines) RPC applied to processed images are plotted with the volume-adjusted Poiseuille solution (dashed red lines) for each experimental case. The uncertainty based on measured flow rate and vessel diameter is plotted for the theoretical solution (upper and lower dashed red lines). The 95% confidence interval on the mean for the experimental data is not distinguishable from the mean. Left to right: glycerine-perfused PTFE, blood-perfused FEP, and blood-perfused collagen. Data shown is averaged in time for the instantaneous sets and along the length of the vessel for all sets and is normalized for each experimental case by the vessel diameter and theoretical maximum velocity.

As done previously to compare SCC and RPC, correlation planes were plotted for a representative correlation region positioned midway between the centerline and wall to examine the effect of sum-of-correlation on correlation accuracy (Figure 5-9). The effect of sum-of-correlation is clear: where multiple scattered peaks are present in the instantaneous correlation planes, the sum of all correlation planes at that location provides a single peak at the correct displacement, indicating that this technique is very effective at removing random noise.
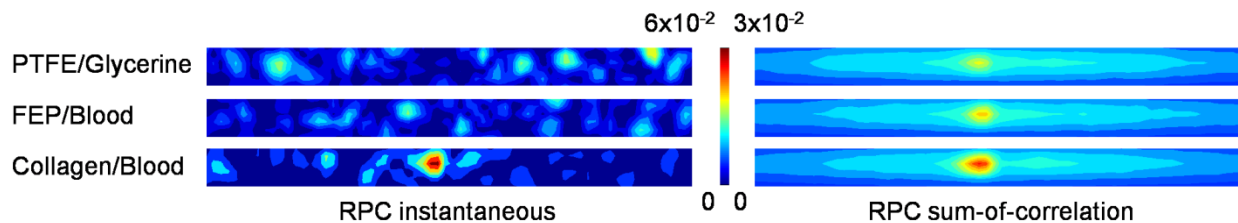

Figure 5-9: Contours of RPC instantaneous and sum-of-correlation planes.

The contour indicates relative correlation magnitude. Only the central 50% window is shown.

5.5   Discussion

The experimental error for all analyses, calculated as the RMS of the error in the experimentally measured velocity fields, is given in Table 5-1. These data quantify the improved accuracy obtained by each successive modification of the PIV algorithm. For all experimental cases and correlation schemes, advanced image preprocessing increases accuracy. For all experimental cases, the optimal PIV processing scheme includes not only image processing, but also RPC sum-of-correlation. For the glycerine-perfused PTFE and blood-perfused collagen cases, the resulting velocity field has less than 10% error, which is less than the 14.6% uncertainty of the theoretical solution. The FEP case deviates more strongly from the Poiseuille profile, with just over 17% error. For this case, there is significant asymmetry in the measured velocity profiles; this is most likely an experimental artifact due to slight curvature along the length of the vessel.

Table 5-1: RMS deviation of experimental mean velocity profile from volume-adjusted theoretical solution, normalized by volume-adjusted theoretical maximum displacement.

Experimental Case	Image Set	PIV Processing Scheme	RMS Error (normalized)
PTFE/glycerine	Raw	SCC instantaneous	0.5807
	Processed	SCC instantaneous	0.3092
		RPC instantaneous	0.3087
		RPC sum-of-correlation	0.0966*
FEP/ blood	Raw	SCC instantaneous	0.6062
	Processed	SCC instantaneous	0.3989
		RPC instantaneous	0.3836
		RPC sum-of-correlation	0.1732
Collagen/blood	Raw	SCC instantaneous	0.5719
	Processed	SCC instantaneous	0.1576
		RPC instantaneous	0.2077
		RPC sum-of-correlation	0.0890*

* These values are within the uncertainty of the theoretical solution. The RMS uncertainty of the theoretical Poiseuille solution was computed by propagation of error obtained from manufacturer-provided uncertainties of the pump flow rate and tubing diameter and was determined to be 0.1461 (normalized by the volume-adjusted theoretical maximum displacement).

5.6   Limitations and Future Directions

Due to limited access to the APS facility, multiple runs of these experiments were not feasible. In particular, this limits the information that can be derived from the FEP case because of the channel asymmetry. While the flow rate was lower than physiological in vessels of this diameter,

101

this is not expected to detract from the results as it is still high enough to obtain shear-independent viscosity and Newtonian flow characteristics. Finally, it is clear from the data that it is not of sufficient fidelity for accurate near-wall flow measurements, but rather provides an overall picture of the velocity magnitude and distribution across the channel. Although the collagen hydrogel was not cellularized in these experiments, is it possible that their presence could contribute to image noise; however, as they would be stationary during the duration of experiments, this effect could be removed in the background subtraction stage of image processing.

It should be noted that comparison of experimental data with the Poiseuille solution integrated along the beam axis implicitly assumes that the experimental solution is derived from the geometric mean of velocities within the correlation window. However, as demonstrated by Fouras et al. [29], this is not strictly accurate as correlation peak detection returns a velocity which represents the mode rather than the mean. Optimization of PIV methods could be used to improve the velocity estimation. Similarly, the RPC filter, which was optimized for particles with Gaussian intensity distribution in optical PIV, could be modified for more effective application to x-ray phase contrast images. This would require assessment of x-ray phase contrast image formation for development of a new SNR model to be used in the filter.

5.7   Conclusions

This work advances previous x-ray PIV technology by demonstrating for the first time flow measurement in an opaque blood-perfused *in vitro* microvascular engineered tissue. We found that the use of a thick, hydrated collagen tissue model has no effect on the quality of the phase-contrast x-ray images, which is promising for future work in complex cellularized tissue models. The methodology presented here outlines an approach for the design of PIV analysis to obtain high-quality flow measurements for challenging data, paving the way toward future experimental investigation of *in vitro* tissue vascular flow.

References

1. Buchanan, C. and M.N. Rylander, *Microfluidic culture models to study the hydrodynamics of tumor progression and therapeutic response.* Biotechnol Bioeng, 2013. **110**(8): p. 2063-72.
2. Salieb-Beugelaar, G.B., et al., *Latest developments in microfluidic cell biology and analysis systems.* Anal Chem, 2010. **82**(12): p. 4848-64.
3. Ghajar, C.M. and M.J. Bissell, *Tumor Engineering: The Other Face of Tissue Engineering.* Tissue Engineering Part A, 2010. **16**(7): p. 2153-2156.
4. Yamada, K.M. and E. Cukierman, *Modeling tissue morphogenesis and cancer in 3D.* Cell, 2007. **130**(4): p. 601-610.
5. Verbridge, S.S., E.M. Chandler, and C. Fischbach, *Tissue-Engineered Three-Dimensional Tumor Models to Study Tumor Angiogenesis.* Tissue Engineering Part A, 2010. **16**(7): p. 2147-2152.
6. Smalley, K.S., M. Lioni, and M. Herlyn, *Life isn't flat: taking cancer biology to the next dimension.* In Vitro Cell Dev Biol Anim, 2006. **42**(8-9): p. 242-7.
7. Youssef, K., et al., *Macro-scale topology optimization for controlling internal shear stress in a porous scaffold bioreactor.* Biotechnol Bioeng, 2012. **109**(7): p. 1844-54.
8. Minchinton, A.I. and I.F. Tannock, *Drug penetration in solid tumours.* Nature Reviews Cancer, 2006. **6**(8): p. 583-592.
9. Polacheck, W.J., I.K. Zervantonakis, and R.D. Kamm, *Tumor cell migration in complex microenvironments.* Cell Mol Life Sci, 2013. **70**(8): p. 1335-56.
10. Brown, J.M. and A.J. Giaccia, *The unique physiology of solid tumors: Opportunities (and problems) for cancer therapy.* Cancer Research, 1998. **58**(7): p. 1408-1416.
11. Whatcott, C.J., et al., *Desmoplasia and chemoresistance in pancreatic cancer*, in *Pancreatic Cancer and Tumor Microenvironment*, P.J. Grippo and H.G. Munshi, Editors. 2012: Trivandrum (India).
12. Ingram, M., et al., *Tissue engineered tumor models.* Biotechnic & Histochemistry, 2010. **85**(4): p. 213-229.
13. Stroock, A.D. and C. Fischbach, *Microfluidic Culture Models of Tumor Angiogenesis.* Tissue Engineering Part A, 2010. **16**(7): p. 2143-2146.
14. Chrobak, K.M., D.R. Potter, and J. Tien, *Formation of perfused, functional microvascular tubes in vitro.* Microvascular Research, 2006. **71**(3): p. 185-196.
15. Tibbitt, M.W. and K.S. Anseth, *Hydrogels as extracellular matrix mimics for 3D cell culture.* Biotechnol Bioeng, 2009. **103**(4): p. 655-63.
16. Shin, Y., et al., *Microfluidic assay for simultaneous culture of multiple cell types on surfaces or within hydrogels.* Nature Protocols, 2012. **7**(7): p. 1247-1259.
17. Bark, D.L., Jr., A.N. Para, and D.N. Ku, *Correlation of thrombosis growth rate to pathological wall shear rate during platelet accumulation.* Biotechnol Bioeng, 2012. **109**(10): p. 2642-50.
18. Dusting, J., J. Sheridan, and K. Hourigan, *A fluid dynamics approach to bioreactor design for cell and tissue culture.* Biotechnol Bioeng, 2006. **94**(6): p. 1196-208.
19. Voigt, E., et al., *Wall Shear Stress Measurements in an Arterial Flow Bioreactor.* Cardiovascular Engineering and Technology, 2012. **3**(1): p. 101-111.
20. Poelma, C., et al., *In vivo blood flow and wall shear stress measurements in the vitelline network.* Experiments in Fluids, 2008. **45**(4): p. 703-713.

103

21. Rossi, M. and I. Ekeberg. *In vitro study of shear stress over endothelial cells by Micro Particle Image Velocimetry (uPIV)*. in *13th International Symposium on Applied Laser Techniques to Fluid Mechanics*. 2006. Lisbon, Portugal.

22. Buchanan, C.F., et al., *Three-Dimensional Microfluidic Collagen Hydrogels for Investigating Flow-Mediated Tumor-Endothelial Signaling and Vascular Organization.* Tissue Eng Part C Methods, 2014. **20**(1): p. 11.

23. Lima, R., et al., *Confocal micro-PIV measurements of three-dimensional profiles of cell suspension flow in a square microchannel.* Measurement Science & Technology, 2006. **17**(4): p. 797-808.

24. Lima, R., et al., *In vitro confocal micro-PIV measurements of blood flow in a square microchannel: the effect of the haematocrit on instantaneous velocity profiles.* J Biomech, 2007. **40**(12): p. 2752-7.

25. Lima, R., et al., *In vitro blood flow in a rectangular PDMS microchannel: experimental observations using a confocal micro-PIV system.* Biomedical Microdevices, 2008. **10**(2): p. 153-67.

26. Lima, R., et al., *Measurement of individual red blood cell motions under high hematocrit conditions using a confocal micro-PTV system.* Annals of Biomedical Engineering, 2009. **37**(8): p. 1546-59.

27. Leble, V., et al., *Asymmetry of red blood cell motions in a microchannel with a diverging and converging bifurcation.* Biomicrofluidics, 2011. **5**(4): p. 44120-4412015.

28. Dubsky, S., et al., *Computed tomographic x-ray velocimetry.* Applied Physics Letters, 2010. **96**(2): p. 023702.

29. Fouras, A., et al., *Three-dimensional synchrotron x-ray particle image velocimetry.* Journal of Applied Physics, 2007. **102**(6): p. -.

30. Irvine, S.C., et al., *Vector tomographic X-ray phase contrast velocimetry utilizing dynamic blood speckle.* Optics Express, 2010. **18**(3): p. 2368-2379.

31. Lee, S.J. and G.B. Kim, *X-ray particle image velocimetry for measuring quantitative flow information inside opaque objects.* Journal of Applied Physics, 2003. **94**(5): p. 3620-3623.

32. Fouras, A., et al., *The past, present, and future of x-ray technology for in vivo imaging of function and form.* Journal of Applied Physics, 2009. **105**(10).

33. Westerweel, J., *Fundamentals of digital particle image velocimetry.* Measurement Science & Technology, 1997. **8**(12): p. 1379-1392.

34. Adrian, R.J., *Twenty years of particle image velocimetry.* Experiments in Fluids, 2005. **39**(2): p. 159-169.

35. Kim, G.B. and S.J. Lee, *X-ray PIV measurements of blood flows without tracer particles.* Experiments in Fluids, 2006. **41**(2): p. 195-200.

36. Lee, S.J. and G.B. Kim, *Synchrotron microimaging technique for measuring the velocity fields of real blood flows.* Journal of Applied Physics, 2005. **97**(6): p. 6.

37. Dubsky, S., et al., *Computed tomographic X-ray velocimetry for simultaneous 3D measurement of velocity and geometry in opaque vessels.* Experiments in Fluids, 2012. **52**(3): p. 543-554.

38. Jamison, R.A., et al., *X-ray Velocimetry and Haemodynamic Forces Within a Stenosed Femoral Model at Physiological Flow Rates.* Annals of Biomedical Engineering, 2011. **39**(6): p. 1643-1653.

104

39. Kim, G.B. and S.J. Lee, *Contrast enhancement of speckle patterns from blood in synchrotron X-ray imaging.* Journal of Biomechanics, 2009. **42**(4): p. 449-454.

40. Irvine, S.C., et al., *Phase retrieval for improved three-dimensional velocimetry of dynamic x-ray blood speckle.* Applied Physics Letters, 2008. **93**(15): p. -.

41. Rae, P.J., D.M. Williamson, and J. Addiss, *A Comparison of 3 Digital Image Correlation Techniques on Necessarily Suboptimal Random Patterns Recorded By X-Ray.* Experimental Mechanics, 2011. **51**(4): p. 467-477.

42. Abraham, L.C., et al., *Guide to collagen characterization for biomaterial studies.* Journal of Biomedical Materials Research Part B-Applied Biomaterials, 2008. **87B**(1): p. 264-285.

43. Kaibara, M., *Rheological behaviors of bovine blood forming artificial rouleaux.* Biorheology, 1983. **20**(5): p. 583-92.

44. Cutnell, J.D. and K.W. Johnson, *Physics*. 4th ed1998, New York: Wiley.

45. Bosart, L.W. and A.O. Snoddy, *Specific Gravity of Glycerol.* Industrial Engineering Chemistry, 1928. **19**(506): p. 1377-1379.

46. Mayo, S.C., A.W. Stevenson, and S.W. Wilkins, *In-Line Phase-Contrast X-ray Imaging and Tomography for Materials Science.* Materials, 2012. **5**(5): p. 937-965.

47. Piccardi, M., *Background subtraction techniques: a review.* 2004 Ieee International Conference on Systems, Man & Cybernetics, Vols 1-7, 2004: p. 3099-3104.

48. Lo, B.P.L. and S.A. Velastin, *Automatic congestion detection system for underground platforms.* Proceedings of 2001 International Symposium on Intelligent Multimedia, Video and Speech Processing, 2001: p. 158-161.

49. Adrian, R.J. and J. Westerweel, *Particle Image Velocimetry*. Cambridge Aerospace Series2011, Cambridge ; New York: Cambridge University Press. xxvi, 558 pages.

50. Westerweel, J. and F. Scarano, *Universal outlier detection for PIV data.* Experiments in Fluids, 2005. **39**(6): p. 1096-1100.

51. Meinhart, C.D., S.T. Wereley, and M.H.B. Gray, *Volume illumination for two-dimensional particle image velocimetry.* Measurement Science & Technology, 2000. **11**(6): p. 809-814.

52. Kumar, B.V.K.V. and L. Hassebrook, *Performance-Measures for Correlation Filters.* Applied Optics, 1990. **29**(20): p. 2997-3006.

53. Eckstein, A.C., J. Charonko, and P. Vlachos, *Phase correlation processing for DPIV measurements.* Experiments in Fluids, 2008. **45**(3): p. 485-500.

54. Eckstein, A. and P.P. Vlachos, *Digital particle image velocimetry (DPIV) robust phase correlation.* Measurement Science & Technology, 2009. **20**(5).

55. Eckstein, A. and P.P. Vlachos, *Assessment of advanced windowing techniques for digital particle image velocimetry (DPIV).* Measurement Science & Technology, 2009. **20**(7): p. -.

56. Meinhart, C.D., S.T. Wereley, and J.G. Santiago, *A PIV algorithm for estimating time-averaged velocity fields.* Journal of Fluids Engineering-Transactions of the Asme, 2000. **122**(2): p. 285-289.

57. Delnoij, E., et al., *Ensemble correlation PIV applied to bubble plumes rising in a bubble column.* Chemical Engineering Science, 1999. **54**(21): p. 5159-5171.

6 Conclusions

This work provides a new *in vitro* tissue microenvironment platform which will facilitate future studies of human biology, disease, and drug delivery optimization across a broad range of applications. First, the dimensions and geometries within the device provide much better reproduction of *in vivo* conditions than the current paradigm utilizing PDMS-based microfluidic chips. The incorporation of ECM-mimicking collagen hydrogels with highly tunable mechanical properties allows the platform to be easily tuned to mimic many *in vivo* tissues; the primary limitation is that it can only be used to mimic soft tissues and not load-bearing tissue. Integration of one or more perfusion channels with quantification of flow conditions enables well-defined convective transport within the channels as well as diffusion transport between channels.

With this device, in-depth studies of tumor metastasis can be performed. In ongoing work, we investigate the interactive roles of matrix stiffness and growth factor gradients on chemotaxis of human breast cancer cells. This study is only the first of many that can be performed using this system; with the introduction of an endothelium to the perfusion channels, intravasation of tumor cells into the vasculature could be recapitulated. Variables such as perfusion rate, chemotactic gradients, and matrix mechanics could be altered independently or simultaneously in order to better understand the conditions which enable or prevent intravasation. Similarly, the platform could be perfused with suspended tumor cells for investigation of conditions which favor extravasation. In all such studies, the physiological accuracy of the platform could be enhanced through introduction of additional cells such as fibroblasts and/or ECM proteins such as elastin or fibronectin to the collagen hydrogel. The potential of this microenvironment platform is limited only by time and resources available.

Appendix: Interactive roles of growth factor gradients and matrix mechanics on breast cancer chemotaxis in three dimensions[4]

Elizabeth Antoine[1], M. Nichole Rylander[2], Pavlos Vlachos[3]

[1] Department of Mechanical Engineering, Virginia Tech, Blacksburg, Virginia, USA

[2] VT-WFU School of Biomedical Engineering and Sciences, Virginia Tech, Blacksburg, Virginia, USA

[3] School of Mechanical Engineering, Purdue University, West Lafayette, Indiana, USA

A.1 Abstract

An important factor in tumor development and metastatic potential is directed migration of cancerous cells. This migration can be driven by spatial and/or temporal gradients in the tumor microenvironment, which differs significantly from the normal tissue microenvironment. Here we investigate the role of epidermal growth factor (EGF) gradients in directed migration of human breast cancer cells (MDA-MB-231) within a fully three-dimensional collagen hydrogel microenvironment. We examine the effect of mechanics of the microenvironment, specifically stiffness and pore diameter, on tumor chemotaxis. We quantify migration characteristics including speed, path length, and chemotactic index of tumor cells in response to EGF concentration ranges of 0-50 ng/mL and 0-100 ng/mL, corresponding to gradients of approximately 70 pg/mL/µm and 140 pg/mL/µm in hydrogels with stiffness from 2000-4000 Pa and corresponding pore size between 2.3 and 1.3 µm. These experiments will enable identification of any nonlinear interactions between matrix mechanics and the steepness of the EGF gradient on chemotactic index; furthermore, it will enable quantification of the relevance of tuning the tumor microenvironment to *in vivo* conditions for chemotaxis studies.

---

[4] In preparation.

A.2 Introduction

Current research suggests that the altered tumor microenvironment may drive cancer aggression and metastatic potential [1, 2]. One characteristic of the tumor microenvironment is the presence of steep gradients in oxygen, nutrients, and other chemical components such as growth factors. These gradients result from the combined effects of high interstitial fluid pressure, dense extracellular matrix (ECM), and poor perfusion [3, 4]. It has been hypothesized that tumor motility and aggressive migration may be caused in part by chemotaxis in response to these gradients [1]. In particular, breast tumor cells are particularly susceptible to gradients in epidermal growth factor (EGF) due to overexpression of EGF receptors and related proteins and receptors [2, 5-8].

With recent advances in tissue engineering and microtechnology, fabrication of *in vitro* tissue microenvironments containing temporally stable chemical gradients has become feasible, while live imaging and cell tracking have enabled a distinction to be made between chemokinesis and chemotaxis [9]. Using soft lithography-based two-dimensional polydimethylsiloxane (PDMS) perfusion chambers, studies have been performed investigating the effect of EGF concentration on chemotaxis: Wang, Saadi, et al. found that the shape of EGF gradients (linear or nonlinear polynomial) and the magnitude regulate chemotaxis of MDA-MB-231 metastatic human breast cancer cells, while Mosadegh et al. found an interaction between uniform EGF concentration and gradients in the chemokine CXCL12 [7, 10, 11]. [12] et al. measured chemotaxis of metastatic rat mammary adenocarcinoma cells (MtLN3) in response to EGF gradients, while Abhyankar et al. performed similar studies in a similar device but incorporated a three-dimensional hydrogel [13]. Raja et al. designed a PDMS microdevice containing an EGF reservoir fabricated from polyethylene glycol diacrylate (PEGDA) for controlled release of EGF to measure chemotaxis *in vitro* or *in vivo* [14]. Polacheck et al. found relationships between interstitial flow velocity, which alters chemokine concentration, and cell density (between 5 and 25 x 10^4 cells/mL) on chemotaxis of MDA-MB-231 cells in a 3D collagen matrix [15].

Despite the importance of such studies, the complex mechanical, chemical, and perfusion components of the tumor microenvironment have not yet been successfully recapitulated. Previous studies have focused on understanding specific biological cues rather than improving

108

the fidelity of the microenvironment platform. Experiments performed on 2D substrates, even those treated with extracellular matrix proteins such as collagen or fibronectin, are unable to provide the three-dimensional microenvironment which has been repeatedly shown to have a momentous effect on cell morphology, signaling, and migration through mechanical and structural interactions [16, 17]. Studies in three-dimensional matrices generally lack direct perfusion of the microenvironment [13, 14, 18] and therefore cells are subjected to gradients in all growth factors and nutrients. Furthermore, although the importance of the role of matrix mechanics in tumor aggresion has been noted, previous chemotaxis studies have not considered parameters such as ECM stiffness [9]. Interactions between microenvironment mechanics and self-expressed chemical cues have been studied, but still at low cell concentrations relative to those found *in vivo* [15].

In this study, we develop a novel tumor microenvironment platform incorporating a physiological concentration of MDA-MB-231 cells in a collagen I hydrogel scaffold with a fully three-dimensional geometry. The device is perfused at physiological flow rates using two parallel channels with diameter comparable to microvasculature. We quantify chemotaxis in response to EGF gradients of varying magnitude formed by diffusion of EGF from one channel into the surrounding hydrogel; these gradients are expected to be linear in the plane between channels but nonlinear in all other regions of the device. The linearity of the in-plane gradients is confirmed experimentally. Finally, we measure the chemotactic influence of microenvironment mechanics by altering stiffness as well as pore diameter for each EGF gradient. The experiments are intended to generate information about the interaction of chemical and mechanical cues in the microenvironment as well as the influence of cell-cell communication enabled by high cell concentrations.

A.3   Materials and Methods

A.3.1   Hydrogel design and fabrication

Human breast carcinoma cells (MDA-MB-231) (American Type Culture Collection) are used in this study. MDA-MB-231 cells are cultured in Dulbecco's modified Eagle's medium, nutrient mixture F-12 (DMEM/F12) (Invitrogen) supplemented with 10% fetal bovine serum (Sigma) and

1% penicillin/streptomycin (Invitrogen). Cell cultures are maintained in a 5% CO_2 atmosphere at 37°C in an incubator; cells with passage number between 38 and 40 are used for all experiments.

Collagen hydrogels mimicking the tumor interstitium are fabricated as described previously [19]. The hydrogel characterization data published in Antoine et al. is used to estimate collagen concentration, solution pH, and polymerization temperature necessary to obtain hydrogels with specified functional properties [19]. The first hydrogel condition, designated "soft" is designed for a compression modulus of 2000 Pa, corresponding to premalignant breast stiffness [20], and has a pore diameter of 2.3 μm. The second hydrogel condition "stiff", is designed with a compression modulus of 4000 Pa and pore diameter 1.3 μm, corresponding to the increased stiffness and reduced pore size of malignant breast tissue tumors [20, 21]. The required fabrication conditions for these hydrogels are as follows: "soft" was 6 mg/ml collagen, pH 7.8, polymerized at 23°C; "stiff" was 6 mg/ml collagen, pH 8.1, polymerized at 37°C.

Briefly, acid-extracted collagen I from rat tail tendon is lyophilized and reconstituted in 0.01M hydrochloric acid to twice the final hydrogel concentration. A neutralization buffer composed of 10X Dulbecco's modified Eagle's medium (DMEM) (Sigma), 1X DMEM supplemented with glucose, sodium bicarbonate, and L-glutamine (Sigma), and 1N sodium hydroxide (Fisher) is prepared according to the recipe in Antoine et al. to obtain the desired pH [19]. Neutralization buffer is added to a pellet of MDA-MB-231 cells and mixed thoroughly but quickly in order to avoid cell death due to the high pH of the buffer. An equal volume of acidic collagen is added to the cell-buffer solution over ice and mixed carefully with a spatula to avoid introducing bubbles. The resulting cell-collagen solution contains 2×10^6 cells/mL.

A.3.2 Tumor microenvironment platform

The hydrogel solution is used to fabricate a microfluidic platform similar to that described previously [22] but containing two smaller microchannels (Figure A-1). Briefly, 15 mm long fluorinated ethylene propylene (FEP) tubing with a diameter of 3 mm (McMaster) is stabilized in a 35 mm Petri dish fitted with a coverslip base. The FEP is plasma-treated to activate surface hydroxyl groups and crosslinked with 1% polyethyleneimine (PEI) in dH_2O for 10 min followed by 0.1% glutaraldehyde in dH_2O for 20 min. Polydimethylsiloxane (PDMS) sleeves containing two parallel channels are inserted in the ends of the FEP and sealed by slightly shrinking the

110

tubing with a soldering iron. The cell-collagen solution is injected into the FEP via one of the PDMS sleeves; subsequently, 1.5" long 26 gauge (464 μm) stainless steel needles are inserted through the PDMS sleeves and through the collagen solution into the opposing sleeves (Figure 7-1 (a)). The assembly is placed at 23°C for the "soft" condition or 37°C for the "stiff" condition and allowed to polymerize for twice the polymerization half-time, which is 18 min for the "soft" condition and 6 min for the "stiff" condition. After polymerization, the needles are removed, leaving parallel cylindrical microchannels separated by a region of hydrogel 700-800 μm wide in the cross-sectional plane (Figure A-1 (b)).
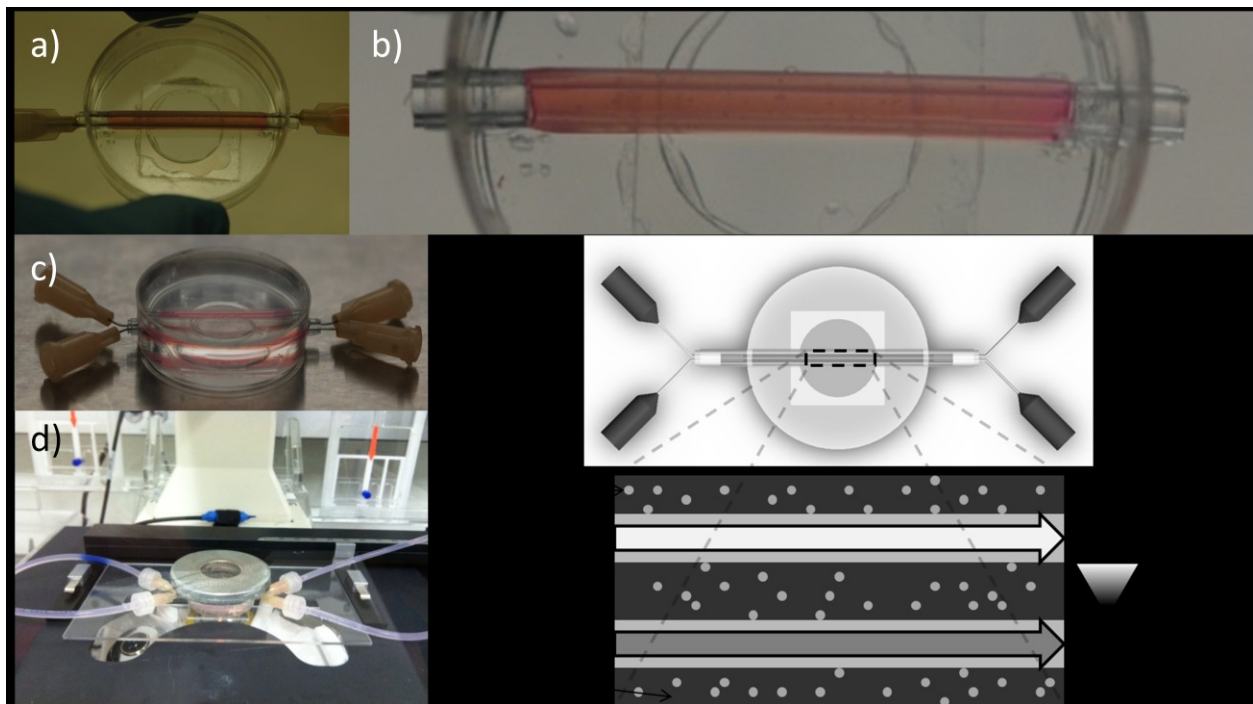

Figure A-1: Tumor microenvironment platform.

a) FEP stabilized in Petri dish, fitted with PDMS sleeves, filled with collagen solution with tumor cells, and containing microchannel-forming needles. b) Hydrogel containing parallel microchannels after removal of needles. c) Device fit with perfusion needles and dish filled with water to eliminate refraction at interfaces. d) Device *in situ* for time-lapse imaging. e) Schematic of device with cross-section depicting layout of cell-containing hydrogel, perfusion channels, and EGF gradient.

Next, the Petri dish is filled with distilled water (dH$_2$O) to enable refractive index matching across curved surfaces for imaging [22]. The dish is covered with a flat acrylic plate and sealed with vacuum grease at the interface to prevent evaporation of the water bath over the duration of the experiment. For perfusion, ½" 26G needles are bent slightly and inserted through the PDMS

111

sleeves into the microchannels (Figure A-1 (c)). These are connected via 1/16" ID silicon tubing (Tygon) to a syringe pump and collection reservoir. A perfusion rate of 21 µL/min for both microchannels was selected. Using an assumption of Poiseuille flow, which we previously validated experimentally [22], this flow rate corresponds to a physiological wall shear stress of 0.4 Pa (4 dyn/cm^2). The EGF gradient is induced by addition of 50 ng/mL or 100 ng/mL EGF (human recombinant epidermal growth factor, Sigma) to one of the two perfusion syringes. The diffusivity of EGF in collagen is estimated based on previous measurements of diffusion of dextran in collagen hydrogels [19]. For diffusion estimation, the hydrodynamic radius of EGF is assumed to be equivalent to that of dextran of the same molecular weight because both are composed of similarly structured branched protein chains. Hydrodynamic radius has been found to scale with the square root of molecular weight for dextrans (FD-4 data sheet, Sigma); this relation was used to interpolate the dextran data and estimate a hydrodynamic radius of 1.7 nm for EGF (6 kDa), which results in a diffusion rate of approximately 190 µm^2/s for both the "soft" and "stiff" hydrogels.

A.3.3 Time-lapse imaging

Cell migration is recorded using time-lapse imaging with an incubated microscope. The tumor microenvironment platform is placed on the stage of a Zeiss Axiovert 200 equipped with a PeCON incubation chamber and maintained at 37°C for the duration of experiments (Figure A-1 (d)). 50-megapixel images are obtained using a color digital single-lens reflex (dSLR) camera (D7000, Nikon) in conjunction with a triple-band filter (ET-DAPI/FITC/Texas Red, Chroma) and 10X magnification (0.41 µm/pix). A halogen lamp is used for brightfield illumination. Images are acquired once every 2 min over a duration of 48 hours. After 48 hours, the microchannel is disconnected from the perfusion system and stained with propidium iodide and calcein AM to determine live/dead cell fraction.

A.3.4 Image analysis for migration quantification

Automated image preprocessing to correct for whole-image illumination and spatial shifts is performed in MATLAB using the Image Processing toolbox as follows: First, the dynamic range of all three color channels of each image is histogram-equalized to the red channel of the first image in the sequence in order to maximize the signal contribution from both channels as well as match intensities between images (Figure A-2 (a-b)). Next, the image is oriented to align the

www.manaraa.com

channel walls with the image plane and cropped to the illuminated region (Figure A-2 (c)). Subsequently, particle image velocimetry (PIV) using standard cross-correlation is performed on sequential image pairs using a large correlation region (2048 x 2048 pixels, windowed to 1024 x 1024 with a Gaussian filter) in order to quantify the bulk image shift from one frame to the next (Figure A-2 (d)). The displacements estimated using PIV are combined with a final crop operation to locate and extract only the region of hydrogel between perfusion channels from each image (Figure A-2 (e-f)).
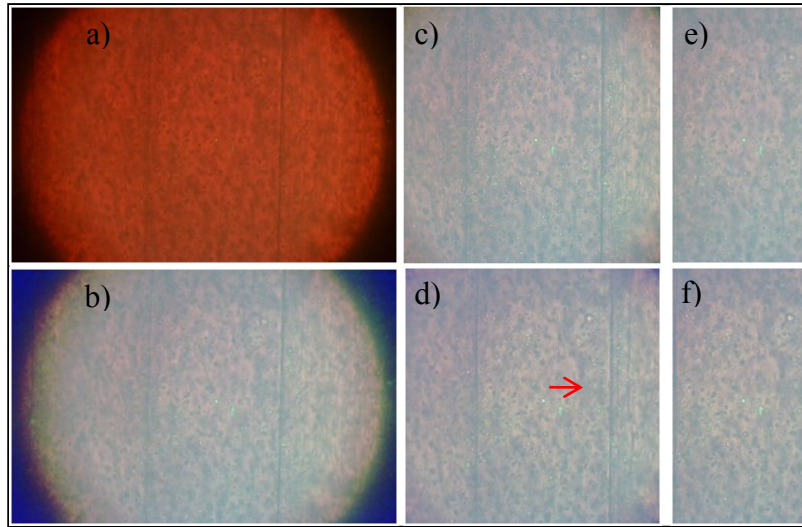

Figure A-2: Image preprocessing and registration.
a) Raw RGB image with visible central hydrogel and perfusion channel boundaries. The illumination source is brightest in the red channel. b) Image after dynamic range correction across all color channels. c) Image after rotation and preliminary crop. d) Subsequent image (32 minutes later) following same operations, with visible horizontal shift in hydrogel location as registered by the displacement vector obtained using PIV (vector length is scaled up by a factor of 5 for visibility). e) First image after crop to hydrogel region. f) Subsequent image with shift correction applied during crop operation.

Next cell tracking is performing by applying particle tracking velocimetry (PTV) techniques to preprocessed images. Cells are identified by a threshold-based blob identification scheme and subsequently sized based on the intensity-weighted centroid. A particle tracking methodology developed by Cardwell et al., which matches particles between frames based on a linear weighting function incorporating displacement, intensity, and particle diameter, is applied in order to track cell motion [23]. Distance between cells is given a weight of 1, while intensity and diameter matching are each weighted as 0.5. From the resulting time-resolved cell tracks, the

113

following parameters are calculated: path length (the sum of displacements between frames), speed (path length divided by time), net displacement (distance between initial and final position), net displacement towards chemoattractant (in this case, net displacement in the –x direction), and chemotactic index CI (net displacement towards chemoattractant divided by overall path length). Furthermore, any variations in cell size or shape can also be quantified.

A.4   Results

A.4.1   Confirmation of gradient linearity

It should be noted that the linear gradient of EGF exists only in the hydrogel in the central plane between the microchannels; elsewhere, the gradient is strongly nonlinear. The profile of the gradient within this plane has been confirmed experimentally. In an acellular hydrogel, 0.1 mg/mL fluorescein isothiocyanate labeled dextran (4 kDa FITC-dextran, Sigma) near the molecular weight of EGF (6 kDa) was added to dH_2O and perfused through one channel, while the other was perfused with dextran-free dH_2O, both at 21 µL/min. Images were acquired using the system described in Section A.3.3 at a rate of 1 frame/min. The red channel (brightfield) was used to monitor microchannel position while the green channel was used to record fluorescence intensity of the dextran diffusing out of the perfusion channel into the surrounding hydrogel (Figure A-3 (left)).
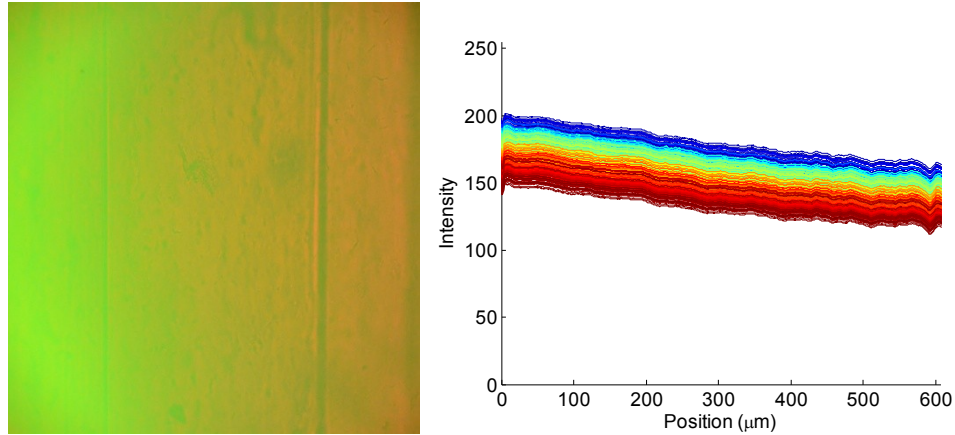
Figure A-3: Dextran perfusion for gradient measurement.

Left: Fluorescence image. The visible vertical lines are the microchannel boundaries; the region between them is collagen. The left channel is perfused with dextran-containing water while the right channel is perfused with dextran-free water. Right: Stability of linear gradient over time. Each line represents the mean intensity profile for a single image; position is measured from the left channel wall. Shading from blue to red represents progression of time; the total duration plotted is 8 hours.

Dextran concentration was estimated from the fluorescence intensity in the images. Intensity in the green channel was averaged along the length of each image to obtain a mean profile at each time (Figure A-3 (right)). A linear gradient was obtained between channels within several minutes of the start of perfusion (transient portion of data not shown) and maintained for the duration of the experiment.

A.5   Anticipated results and outlook

Because both the "soft" and "stiff" hydrogel conditions are fabricated using the same concentration of collagen (6 mg/ml), the same number of ligands is available for cellular adhesion in each condition. Therefore, the chemotactic response to variations in matrix mechanics which will be quantified in these experiments will not be dependent on number of adhesion sites. Similarly, while migration in 3D is regulated in part by proteolysis and matrix degradation [24], especially in matrices such as these with pore size significantly smaller than cell dimensions [25], proteolytic activity should be comparable in both conditions. Although the pore size differs between the hydrogel conditions, both mean pore diameters (2.3 μm and 1.3 μm for 2000 and 4000 Pa, respectively) are significantly smaller than the characteristic length of MDA-MB-231 cells (50 μm) [26]. As a result, we expect differences in migration speed between

115

the two hydrogels (under the same EGF stimulus) to result only from changes in cellular traction forces. Traction forces normally are greater in stiffer matrices; we hypothesize that this will result in faster migration.

A previous study performed in 2D suggests that chemotactic index is low with linear EGF gradients, regardless of magnitude, but is significant in nonlinear EGF gradients [10]. They hypothesized that the relative concentration difference across the cell is sufficiently altered due to the inflection of the nonlinear gradient to stimulate stronger chemotaxis. The cell response to linear gradients in 3D, as will be measured here, could conceivably be similar to the 2D case; however, the activation of EGF receptors on all surfaces of the cell rather than only the contact surface is likely to contribute in some way to chemotactic potential.

The proposed experiments will generate data that will help answer these outstanding questions and further our understanding of interactions between the tumor microenvironment, chemotaxis, and metastatic potential. Future work will include investigation of the chemotactic response of tumor cells with greater or lesser metastatic potential to the same microenvironmental stimuli.

References

1. Roussos, E.T., J.S. Condeelis, and A. Patsialou, *Chemotaxis in cancer.* Nature Reviews Cancer, 2011. **11**(8): p. 573-587.
2. Bissell, M.J., et al., *The organizing principle: microenvironmental influences in the normal and malignant breast.* Differentiation, 2002. **70**(9-10): p. 537-546.
3. Minchinton, A.I. and I.F. Tannock, *Drug penetration in solid tumours.* Nature Reviews Cancer, 2006. **6**(8): p. 583-592.
4. Whatcott, C.J., et al., *Desmoplasia and chemoresistance in pancreatic cancer*, in *Pancreatic Cancer and Tumor Microenvironment*, P.J. Grippo and H.G. Munshi, Editors. 2012: Trivandrum (India).
5. Philippar, U., et al., *A Mena invasion isoform potentiates EGF-induced carcinoma cell invasion and metastasis.* Developmental Cell, 2008. **15**(6): p. 813-28.
6. Hernandez, L., et al., *The EGF/CSF-1 paracrine invasion loop can be triggered by heregulin beta1 and CXCL12.* Cancer Research, 2009. **69**(7): p. 3221-7.
7. Mosadegh, B., et al., *Epidermal growth factor promotes breast cancer cell chemotaxis in CXCL12 gradients.* Biotechnol Bioeng, 2008. **100**(6): p. 1205-13.
8. Price, J.T., et al., *Epidermal growth factor promotes MDA-MB-231 breast cancer cell migration through a phosphatidylinositol 3'-kinase and phospholipase C-dependent mechanism.* Cancer Research, 1999. **59**(21): p. 5475-8.
9. Kim, B.J. and M. Wu, *Microfluidics for mammalian cell chemotaxis.* Annals of Biomedical Engineering, 2012. **40**(6): p. 1316-27.
10. Wang, S.J., et al., *Differential effects of EGF gradient profiles on MDA-MB-231 breast cancer cell chemotaxis.* Exp Cell Res, 2004. **300**(1): p. 180-9.
11. Saadi, W., et al., *A parallel-gradient microfluidic chamber for quantitative analysis of breast cancer cell chemotaxis.* Biomedical Microdevices, 2006. **8**(2): p. 109-118.
12. Fok, S., et al., *Planar microfluidic chamber for generation of stable and steep chemoattractant gradients.* Biophysical Journal, 2008. **95**(3): p. 1523-30.
13. Abhyankar, V.V., et al., *A platform for assessing chemotactic migration within a spatiotemporally defined 3D microenvironment.* Lab on a Chip, 2008. **8**(9): p. 1507-15.
14. Raja, W.K., et al., *A new chemotaxis device for cell migration studies.* Integr Biol (Camb), 2010. **2**(11-12): p. 696-706.
15. Polacheck, W.J., J.L. Charest, and R.D. Kamm, *Interstitial flow influences direction of tumor cell migration through competing mechanisms.* Proceedings of the National Academy of Sciences of the United States of America, 2011. **108**(27): p. 11115-11120.
16. Yamada, K.M. and E. Cukierman, *Modeling tissue morphogenesis and cancer in 3D.* Cell, 2007. **130**(4): p. 601-610.
17. Griffith, L.G. and M.A. Swartz, *Capturing complex 3D tissue physiology in vitro.* Nat Rev Mol Cell Biol, 2006. **7**(3): p. 211-24.
18. Haessler, U., et al., *An agarose-based microfluidic platform with a gradient buffer for 3D chemotaxis studies.* Biomedical Microdevices, 2009. **11**(4): p. 827-35.
19. Antoine, E.E., P.P. Vlachos, and M.N. Rylander, *Characterization of Material Properties of Type I Collagen Hydrogels as a Function of Multiple Fabrication Parameters.* in preparation.
20. Levental, I., P.C. Georges, and P.A. Janmey, *Soft biological materials and their impact on cell function.* Soft Matter, 2007. **3**(3): p. 299-306.

21. Paszek, M.J., et al., *Tensional homeostasis and the malignant phenotype.* Cancer Cell, 2005. **8**(3): p. 241-254.

22. Buchanan, C.F., et al., *Three-Dimensional Microfluidic Collagen Hydrogels for Investigating Flow-Mediated Tumor-Endothelial Signaling and Vascular Organization.* Tissue Eng Part C Methods, 2014. **20**(1): p. 11.

23. Cardwell, N.D., P.P. Vlachos, and K.A. Thole, *A multi-parametric particle-pairing algorithm for particle tracking in single and multiphase flows.* Measurement Science & Technology, 2011. **22**(10).

24. Sabeh, F., R. Shimizu-Hirota, and S.J. Weiss, *Protease-dependent versus -independent cancer cell invasion programs: three-dimensional amoeboid movement revisited.* J Cell Biol, 2009. **185**(1): p. 11-9.

25. Zaman, M.H., et al., *Migration of tumor cells in 3D matrices is governed by matrix stiffness along with cell-matrix adhesion and proteolysis.* Proc Natl Acad Sci U S A, 2006. **103**(29): p. 10889-94.

26. Polacheck, W.J., I.K. Zervantonakis, and R.D. Kamm, *Tumor cell migration in complex microenvironments.* Cell Mol Life Sci, 2013. **70**(8): p. 1335-56.